REVIEWS

Journal of Semiconductors
(2019) 40, 121801
doi: 10.1088/1674-4926/40/12/121801

Deep-ultraviolet integrated photonic and optoelectronic devices: A prospect of the hybridization of group III–nitrides, III–oxides, and two-dimensional materials

Nasir Alfaraj‡, Jung-Wook Min‡, Chun Hong Kang, Abdullah A. Alatawi, Davide Priante, Ram Chandra Subedi, Malleswararao Tangi, Tien Khee Ng, and Boon S. Ooi†

Photonics Laboratory, Computer, Electrical and Mathematical Sciences and Engineering Division (CEMSE), King Abdullah University of Science and Technology (KAUST), Thuwal 23955-6900, Kingdom of Saudi Arabia

Abstract: Progress in the design and fabrication of ultraviolet and deep-ultraviolet group III–nitride optoelectronic devices, based on aluminum gallium nitride and boron nitride and their alloys, and the heterogeneous integration with two-dimensional and oxide-based materials is reviewed. We emphasize wide-bandgap nitride compound semiconductors (i.e., (B, Al, Ga)N) as the deep-ultraviolet materials of interest, and two-dimensional materials, namely graphene, two-dimensional boron nitride, and two-dimensional transition metal dichalcogenides, along with gallium oxide, as the hybrid integrated materials. We examine their crystallographic properties and elaborate on the challenges that hinder the realization of efficient and reliable ultraviolet and deep-ultraviolet devices. In this article we provide an overview of aluminum nitride, sapphire, and gallium oxide as platforms for deep-ultraviolet optoelectronic devices, in which we criticize the status of sapphire as a platform for efficient deep-ultraviolet devices and detail advancements in device growth and fabrication on aluminum nitride and gallium oxide substrates. A critical review of the current status of deep-ultraviolet light emission and detection materials and devices is provided.

Key words: deep-ultraviolet; ultraviolet; photonics; optoelectronics; hybrid

Citation: N Alfaraj, J W Min, C H Kang, A A Alatawi, D Priante, R C Subedi, M Tangi, T K Ng, and B S Ooi, Deep-ultraviolet integrated photonic and optoelectronic devices: A prospect of the hybridization of group III–nitrides, III–oxides, and two-dimensional materials[J]. *J. Semicond.*, 2019, 40(12), 121801. http://doi.org/10.1088/1674-4926/40/12/121801

1. Introduction

Ultraviolet (UV)-emitting group III–nitride materials hold a promising potential for a variety of multifunctional applications, including solid-state lighting technology[1–4] and water purification and disinfection[5, 6]. With the wide range of wavelength tunability available to UV-emitting group III–nitride materials, the most promising germicidal ultraviolet devices are found in aluminum gallium nitride and its alloys ($Al_xGa_{1-x}N$, where $0 < x < 1$), and one of the most crucial applications of $Al_xGa_{1-x}N$-based devices is water sterilization[7–10] , particularly for highly water-stressed countries. Group III–nitride materials are chemically and thermally robust[11–13], exhibit long carrier lifetimes[14], are operationally stable[15], and are the only known materials that have wide and direct bandgaps and are wavelength-tunable within the UV regime of operation (from around 200 to 400 nm). Other material systems do not exhibit these two properties simultaneously, but achieving p-type conduction is challenging for high aluminum-content group III–nitride compounds[16].

The heterogeneous integration of various forms of inorganic materials (which encompasses growing numbers of material types) into one electronic system is based on group III–nitridecompoundsemiconductors[17–28].Examplesincludethe following: on-chip frequency upconversion[29], nanomechanical optical detection[30, 31], solid-state neutron detection[32–34], piezoelectric resonators and electrical and harmonic generators[35–40], strain-gated transistors (SGTs)[41], multiple-valued logic (MVL) circuits[42], single-photon emission[43–45], water splitting[46–51], solar-blind photodetection[52], pressure[53], gas[54], pH[55], sensors, white light generation from light-emitting diodes (LEDs)[56–58] and from laser diodes (LDs)[59], metal–oxide–semiconductor field-effect transistors (MOSFETs)[60–62] and high-electron-mobility transistors (HEMTs)[63, 64], mechanically demanding applications[65], and thermoelectrics and thermal management[66–70]. All of these show promise in advancing the development of the new "new electronics" industry[71]. While resonant tunneling transport is essential for the operation of ultrafast electronic oscillators and quantum cascade lasers[72–75], this quantum mechanical effect remained elusive in the family of group III–nitride semiconductors until very recently[76, 77]. Encomendero *et al.* have engineered high-current resonant tunneling transport in group III–nitride heterostructures, which is employed to generate microwave power[76]. Their GaN/AlN resonant tunneling diodes exhibited microwave oscillations with peak current densities up to 220 kA/cm^2. A close look at common compound semiconductor materials reveals that zinc oxide (ZnO), a group II–VI semiconductor, has a wide direct bandgap[78], but it suffers from low p-type conductivity. Nevertheless, ZnO is one of the most promising materials for the development of sensor[79] and translucent optoelectronic devices[80]. These predictions are based

Nasir Alfaraj and Jung-Wook Min contributed equally to this work.
Correspondence to: B S Ooi, boon.ooi@kaust.edu.sa
Received 15 APRIL 2019.

on the fact that zinc (Zn) is an earth-abundant material; the exciton binding energy of ZnO are unusually high (about 60 meV), and the bandgap energy is around 3.4 eV[81]. From another point of view, it is well known that an internal electrical field can reduce the effective bandgap energy, a phenomenon referred to as the Franz–Keldysh effect[82, 83]. Bridoux *et al.* have demonstrated that this effect can be intensified when a tensile strain is generated in ZnO thin films[84]. Since the piezoelectric coefficient of ZnO is very high, very small strains can produce electric fields that reduce the effective energy gap on these films, providing a building block to the new field of piezo-phototronics[85–88].

Successful doping of a semiconductive material is a crucial factor in achieving an efficient carrier injection process to realize excellent device performance characteristics[89–96]. $Al_xGa_{1-x}N$-based UV light-emitting devices can be employed in a variety of applications, including water purification (because of the high absorbance by pathogenic DNA at UV wavelengths)[97], medical diagnostics[98], high-efficiency lighting[99], and chemical/biological detection processes[100]. Remarkable progress has been made to improve the quality and performance of devices based on $Al_xGa_{1-x}N$, and their attractive properties. Such properties include the tunability of their bandgap energies within a significant portion of the UV spectral range (namely, UV-C below 280 nm, UV-B between 280 and 315 nm, and UV-A between 315 and 400 nm), high chemical and device operational stability[101] and reliability[102], internal quantum efficiency (IQE), external quantum efficiency (EQE), and wall plug efficiency (WPE) of III–nitride-based devices, especially deep-ultraviolet (DUV) devices[103]. These properties remain relatively low, and the presence of spontaneous and piezoelectric fields limits their potential[104, 105]. The main causes of such low efficiency parameters are the high density of threading dislocations (TDs) extending from the surface of a strained layer system, which causes internal structural cracking and the subsequent increase in nonradiative recombination channels within the device active regions[90, 106–110]. These issues arise mainly from the lattice and thermal mismatches between the grown material and the substrate[111–113]. For devices emitting at short wavelengths below 280 nm, the EQEs do not exceed 20%[104], and hardly reach 20.3%, by designing a DUV LED utilizing a UV transparent magnesium (Mg)-doped $Al_{0.65}Ga_{0.35}N$ top contact layer, a rhodium (Rh) mirror electrode, an AlN template on a patterned sapphire substrate, and encapsulation resin[114]. In addition, $Al_xGa_{1-x}N$-based heterostructures exhibit poor p-type doping behavior[115, 116], and generally suffer from significant light extraction losses, particularly toward the DUV spectral regime[117], while conductive n-type $Al_xGa_{1-x}N$ layers can be realized with relative ease[118, 119]. A recent report by Nippert *et al.* attributed the efficiency droop in $Al_{0.45}Ga_{0.55}N$ quantum wells (QWs) to internal loss mechanism within the QWs, strikingly similar to the well-known case of $In_xGa_{1-x}N$/GaN QWs[120]. They attributed the reduction in IQE at high excitation power densities to the losses associated with direct and indirect[121] Auger processes, and have extracted an Auger recombination coefficient of $C = 2.3 \times 10^{-30}$ cm^6/s using time-resolved photoluminescence (TRPL), which is of the same order as determined by some studies investigating $In_xGa_{1-x}N$/GaN QWs for experimental report of C coefficient[122, 123] and in epitaxially-grown 280 nm multiple quantum well (MQW) $Al_{0.57}Ga_{0.43}N$ LEDs (by solving the carrier rate equation in the semiconductor)[124]. In general, Shockley–Read–Hall (SRH) recombination has been viewed by a broad swath of researchers as the dominant recombination mechanism at TDs, rendering it scalable only with the threading dislocation density (TDD)[125, 126]. Nagasawa and Hirano argued that the low TDDs of roughly 5×10^8 cm^{-2} demonstrated by $Al_xGa_{1-x}N$ and AlN templates on sapphire decreases the number of nonradiative recombination channels[127].

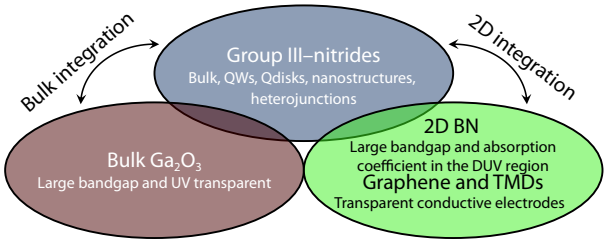

Fig. 1. (Color online) Graphical abstract reflecting areas explored in this review article.

While it has been well established that electron-beam irradiation[91] and thermal processing[128] can activate dopant impurities in $In_xGa_{1-x}N$ and remove magnesium-hydrogen complexes in GaN films[129], this raises the following questions: (1) If an electron-beam can ionize impurities in $In_xGa_{1-x}N$, can one develop an *in-situ* ion activation system for the growth of $Al_xGa_{1-x}N$[130–133]? (2) During the epitaxial growth process, can one irradiate the sample with UV, X-ray, or, perhaps, γ-ray radiation? (3) How can one design a safe-to-use system with an *in-situ* ion activation source? At the moment, these techniques do not seem feasible in the growth process of $Al_xGa_{1-x}N$, although Fujiwara and Sasaki fabricated random lasing structures directly on magnesium-doped GaN thin films solely using a UV irradiation of pulsed intense laser on the material surface[134].

In this article, we review the recent progress in the growth and fabrication of UV and DUV group III–nitride optoelectronic devices and materials based on $Al_xGa_{1-x}N$[135–138] and boron aluminum nitride and its alloys ($B_xAl_{1-x}N$, $0 < x < 1$)[139–141]. We provide an overview of UV and DUV light-emitting and detection devices from the prospect of the heterogeneous integration of group III–nitride compound semiconductors and two-dimensional (2D) materials with select material properties, particularly graphene[142] and 2D transition metal dichalcogenides (TMDs)[143], as illustrated through the graphical abstract of this article shown in Fig. 1. This graphical abstract represents a general schematic definition of the hybridization of group III–nitrides, III–oxides, and two-dimensional materials: a combination of 2D and bulk integration processes for different purposes such as the realization of highly absorptive DUV device active regions with transparent conductive electrodes integrated on UV transparent optoelectronic device platforms. Because of the two-dimensional confinement of electrons in a monolayer of 2D materials, the properties of such monolayers can be controlled by the electrical field formed on the monolayer surface[144]. We examine the basic physics and crystallography of these materials and discuss the challenges that hamper the realization of efficient and reliable DUV devices. Comparisons between sapphire and aluminum nitride as templates for optoelectronic devices is provided within the discussion, in which we criticize the status of sapphire as a platform for efficient DUV devices and

Table 1. Comparison between thermal and mechanical properties of AlN, sapphire, and Ga_2O_3 substrates.

Property	AlN[a]	Sapphire[b]	Ga_2O_3[c]
Thermal conductivity (W/(m·K))	180–230	42	[100]: 13.6 [010]: 22.8
Thermal expansion coefficient (10^{-6} K^{-1})	4.6[d] 5.2[e]	7.0[f] 7.7[g]	α_a = 0.1–2.78 α_b = 1.68–5.84 α_c = 1.74–6.27
Specific heat capacity (J/(kg·K))	720	750	490
Melting point (°C)	2200	2053	1725
Young's modulus (GPa)	320	470	230
Vickers hardness (GPa)	11	22.5	(101): 9.7 ($\bar{2}$01): 12.5

[a] As reported by MARUWA CO., LTD, Japan. [b] As reported by Kyocera Corporation, Japan. [c] As reported by TAMURA Corporation, Japan. Thermal expansion coefficient values are from Ref. [152] and reported in the temperature range of 24.85–926.85 °C. [d] In the range of 40–400 °C. [e] In the range of 40–800 °C. [f] In the range of 40–400 °C, perpendicular to *c*-axis. [g] In the range of 40–400 °C, parallel to *c*-axis.

detail the advancements in device growth and fabrication on aluminum nitride templates. We briefly discuss the most common growth and fabrication methods used to synthesize various types of group III–nitride nanostructures. We also provide a critical review of the status quo with regard to light emission and detection devices based on group III–nitride semiconductors. The integration of new materials for the realization of DUV devices, the process of carrier injection, and the relative alignment of the energy bands at group III–nitride semiconductor heterojunctions and their effects on device operation are highlighted. Given its usefulness and the ability to implant more nitrogen atoms to make it more insulating, thus capable of sustaining higher electric fields for power device applications[145], gallium oxide (Ga_2O_3) and its alloys have emerged as the materials of choice for the realization of DUV optoelectronic devices[146]. For more details about its physiochemical properties and heterogeneous integration with other group III–oxide materials, we refer the reader to the editorial and articles written by Higashiwaki and Jessen[147], Peelaers *et al.*[148], and Pearton *et al.*[149]. Table 1 provides a comparison between thermal and mechanical properties of AlN, sapphire, and Ga_2O_3 substrates. We note that sapphire suffers from considerably lower thermal conductivity and relatively higher thermal expansion coefficients when compared to AlN. On the other hand, Ga_2O_3 exhibits the lowest thermal conductivity values among the three substrates. Nevertheless, Ga_2O_3 substrates are significantly more expensive than sapphire, while it can be extrinsically conductive with carrier concentrations of up to 10^{19} cm^{-3} and conductivities of up to 100 S/cm for tin (Sn)-doped substrates. Therefore, unlike sapphire and AlN substrates, Ga_2O_3 substrates can be used to realize vertically-oriented optoelectronic devices[150, 151].

1.1. Aluminum gallium nitride system

While the doping process and its effects on group III–nitride semiconductors are not fully understood yet, we assert that AlN is the hardest to dope when compared to GaN or indium nitride (InN) and their alloys ($In_xGa_{1-x}N$, $0 < x < 1$)[89]. The primary difficulty is efficient doping of grown films with aluminum-rich clusters; the problem is particularly severe for p-

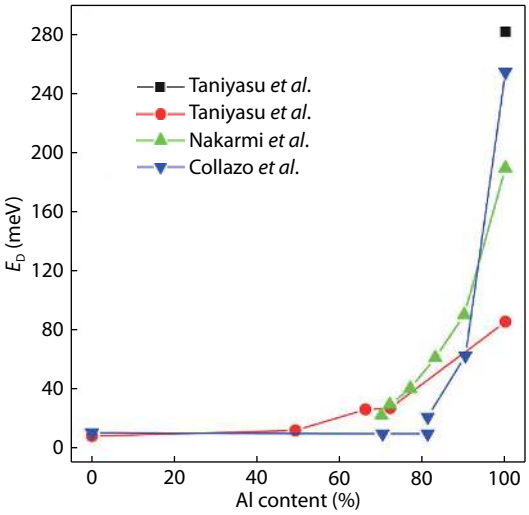

Fig. 2. (Color online) Comparison of donor activation energies of Si-doped $Al_xGa_{1-x}N$ obtained experimentally by various research groups[162–165]. Reprinted with permission from Ref. [161]. ©2017, Elsevier.

type doping, which is essential for the realization of Ohmic contacts in optoelectronic devices. This can be attributed to the empirical fact that magnesium impurities do not incorporate well into AlN and its high-aluminum-content alloys because of the high energy required to activate dopants. In particular, a high density of compensating point defects can be generated in these materials[153, 154]; such defects include nitrogen vacancies (V_N)[155], substitutional magnesium (Mg_{Ga})–V_N complex and other defect complexes[156–158], and magnesium interstitials[159, 160]. Therefore, high-conductivity p-type aluminum-rich $Al_xGa_{1-x}N$ films are difficult to obtain because of the low doping efficiency caused by the high activation energies of the acceptor dopant atoms. Using experimental data obtained by different research groups[161–165], the activation energy of silicon (Si) as an n-type dopant was observed to begin increasing dramatically when the incorporated aluminum content increased in $Al_xGa_{1-x}N$ beyond 40%, and reaches its maximum in pure AlN at around 280 meV, as shown in Fig. 2. This translates to an undesirable outcome: When the activation energy of silicon is high, only a few percent of silicon impurities are activated in $Al_xGa_{1-x}N$. While increasing the silicon impurity incorporation percentage seems an option, there is a self-compensate effect when the concentration of silicon is too high, as shown in Fig. 3. High silicon concentrations were observed to compromise the crystal integrity of $Al_xGa_{1-x}N$, increasing its dislocation density and internal aluminum and/or V_Ns. This situation reciprocates for the p-type doping process, where the activation energy of magnesium (E_A^{Mg}) as a p-type dopant in AlN was estimated to be between 465 and 758 meV[115, 161, 162, 166–168].

The most common p-type dopant for $Al_xGa_{1-x}N$ is magnesium through the introduction of highly-pure bis(cyclopentadienyl)magnesium ($MgCp_2$) into a metalorganic vapor-phase epitaxy (MOVPE) reactor[169]. While group II elements and transition metals could, in theory, constitute p-type dopants for group III–nitride compound semiconductors, the conductivity of magnesium-doped $Al_xGa_{1-x}N$ (specifically for high *x* values) is relatively low at room temperature due to the high E_A^{Mg} values, as emphasized earlier. Using Hall-effect measurements, E_A^{Mg} values of magnesium-doped AlN were found

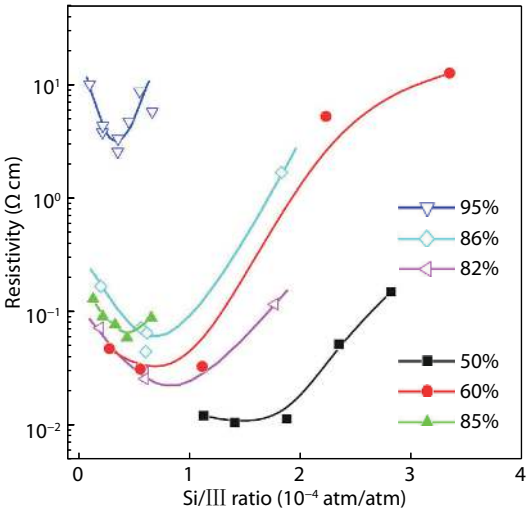

Fig. 3. (Color online) Variation in $Al_xGa_{1-x}N$ resistivity values as a function of the Si/III ratio[166]. The percentages refer to aluminum mole fraction. Reprinted with permission from Ref. [161]. ©2017, Elsevier.

to be around 510 meV[115] and 630 meV[162]. Hole concentration of magnesium-doped AlN, p, can be roughly estimated after making the following assumptions: (1) an acceptor concentration, N_A, of 10^{20} cm^{-3} and (2) the energy of electrons in the valence band follow the Maxwell–Boltzmann distribution,

$$p(T) = N_A e^{-E_A^{Mg}/kT}, \quad (1)$$

p can be determined to be between 2.4×10^8 and 3.9×10^{10} cm^{-3} at room temperature, which results in magnesium-doped AlN being an insulator. Taniyasu, Kasu, and Makimoto observed a p value of as low as 10^{10} cm^{-3} in p-type AlN at room temperature[162]. Nevertheless, to realize efficient DUV optoelectronic devices, conductive p-type $Al_xGa_{1-x}N$ layers are necessary. With limited success, there were several attempts to improve the conductivity and efficiency of p-$Al_xGa_{1-x}N$-based materials and devices through the incorporation of the following schemes: tunnel junctions (TJs)[170], $Al_xGa_{1-x}N$/GaN superlattices (SLs)[171–173], p-type graded $Al_xGa_{1-x}N$ polar heterostructures[174–178], $Al_xGa_{1-x}N$-delta-GaN QW structures[179, 180], and co-doping[181, 182]. In 2017, Tran *et al.* claimed to have experimentally accomplished remarkably high free hole concentrations of up to 6×10^{17} cm^{-3} in magnesium-doped AlN nanowires at room temperature[183], a value that is several orders of magnitude greater than those of conventional AlN epitaxial layers which are in the range of 10^{10} cm^{-3}[115, 162, 167], which in turn are several orders of magnitude lower than what is necessary to realize efficient LED and LD operation (10^{17}–10^{19} cm^{-3}). They attributed this strikingly unusual high carrier concentration in AlN to the efficient hole hopping conduction in the magnesium impurity band. This was compelled by the significantly improved magnesium-dopant incorporation in the almost defect-free AlN nanostructures[183, 184]. It is worth noting that although no research group was able to achieve conductive beryllium (Be)-doped $Al_xGa_{1-x}N$, in 2018 beryllium-doped AlN was found to exhibit a lower acceptor ionization energy of 330 meV[185] (in good agreement with effective-mass theory[168] and density functional theory [DFT][186] studies) compared to that of magnesium-doped AlN. The values of p were found to be around 10^{14} cm^{-3}, taking into account the aforementioned assumptions for estimating p, which demonstrates three orders of magnitude improvement compared to magnesium-doped $Al_xGa_{1-x}N$. However, later in 2010, Szabó *et al.* estimated the ionization energy of beryllium acceptors in AlN to be around 0.97 eV[187]. In 2018, Soltamov *et al.* studied the diffusion characteristics of beryllium in AlN single crystals (vapor phase at 1850 °C). They demonstrated that beryllium diffusion led to the quenching of visible (450 nm, 2.75 eV) and DUV (265 nm, 4.7 eV) optical absorption bands simultaneously with the triggering of an absorption band peak at around (248 nm, 5 eV). They also found that the introduction of beryllium impurities compensated the donor type paramagnetic centers by examining the doped semiconductor using electron paramagnetic resonance (EPR)[188]. They observed a shift of the Fermi level toward the lower energy levels of the AlN energy bandgap, reasoning that the beryllium atoms that incorporated into AlN through the diffusion process acted predominantly as acceptor impurities. However, this shift of the Fermi level resulted in recharging of the deep level defects in the AlN bandgap, causing the observed quenching of the visible and UV absorption bands. The commercial and scientific use of beryllium is impeded by its cost and the toxicity of inhaled beryllium-containing dusts[189, 190]. Furthermore, the use of foreign substrates, such as silicon and sapphire, and the short diffusion lengths of aluminum adatoms on growth surfaces cause deteriorated $Al_xGa_{1-x}N$ crystalline quality, especially for aluminum-rich $Al_xGa_{1-x}N$ films. These generated dislocation defects result in high leakage currents and suppression of the radiative recombination efficiency of carriers in $Al_xGa_{1-x}N$-based device active regions, which negatively impact device reliability and quantum efficiencies of optoelectronic devices[191, 192].

Islam *et al.* demonstrated tunable DUV LEDs using ultrathin GaN quantum dots (QDs) in the device active regions[193], by manipulating the GaN layer thicknesses with monolayer (ML) precision and applying a polarization-induced doping scheme for both n- and p-type carrier injection regions to enhance the electrical injection of carriers into the active regions[194, 178]. The surface-emitted light from GaN ML quantized structures is predominantly transverse electric (TE)-polarized[195], enhancing light extraction process when compared to $Al_xGa_{1-x}N$-based active regions[196]. We note that Reich *et al.* employed $\boldsymbol{k}\cdot\boldsymbol{p}$ theoretical model calculations to demonstrate an optimized $Al_xGa_{1-x}N$ MQW active region design, yielding increased TE polarization in bottom-emitting DUV LEDs with peak emission wavelengths of as short as 239 nm[197]. Compared to a previously reported value of 243 nm ($E \approx$ 5.1 eV)[198], the shortest electroluminescence (EL) emission wavelength Islam *et al.* achieved in their work was 232 nm ($E \approx$ 5.34 eV), a record short wavelength DUV LED in structures that simultaneously comprise binary GaN active regions and polarization-induced doping strategy. Their work advanced the incorporation of ultrathin GaN QWs and QDs as alternatives to $Al_xGa_{1-x}N$, constituting the light emission source material[198–200]. Through the reduction of GaN bulk layers having a direct energy bandgap of 3.4 eV (λ = 365 nm), to a few ML-thick quantum confined structures that are sandwiched between AlN barriers, tunable DUV photoemission from 234 to 274 nm (from about 5.3 to 4.5 eV) has been observed[198]. This relatively large blueshift in peak emission caused by quantum confinement effects was possible by virtue of the large conduction band offset (CBO) between GaN

and AlN of about 1.8 eV[201–205]. According to first-principles calculations based on DFT[206], and many-body perturbation theory and experimental results[207], the emission wavelength can be further lowered to 224–228 nm ($E \approx 5.44$–5.54 eV) for 1 ML GaN QWs, and additionally reduced to 222 nm ($E \approx 5.59$ eV) with 1–2 ML QDs[208]. Local compositional disorder- and defect-free and fully strained ML-thick GaN quantum structures offer enhanced IQE characteristics over $Al_xGa_{1-x}N$-based active regions: ultrathin quantized active regions can potentially enhance the IQE[208, 209], while the quantum-confined Stark effect (QCSE) is suppressed because of the negligible voltage drops across thin layers and the resulting improved overlap integral value between the electron and hole wavefunctions[210]. Also, because of three-dimensional (3D) quantum confinement of carriers in QDs, the injected carriers in QD-based LED structures are strongly delocalized from nonradiative recombination channels at TDs, further enhancing the IQE[211, 212].

By growing quasi-one-dimensional (quasi-1D) group III–nitride nanostructures using plasma-assisted molecular beam epitaxy (PA-MBE)[30, 138, 213–216], dislocation- and piezoelectric polarization-free $Al_xGa_{1-x}N$-based light-emitting nanowire structures can be realized. Nanowires have the advantage of allowing for the growth of lattice-mismatched foreign substrates, such as silicon and sapphire[217–221], in addition to achieving nearly defect-free crystals[222, 223], and therefore, opportunity for fabricating high efficiency optoelectronic devices, including LEDs and lasers, because of the highly effective lateral stress relaxation associated with the nanowire large surface-area-to-volume ratios[224–228]. However, because of the higher surface-area-to-volume ratios in lower-dimen sional semiconductor structures and the subsequent formation of deep-level surface trap energy states, the intrinsic properties of *d*-dimensional semiconductor structures for all $d \in \{0,1,2\}$ are directly influenced by their surface condition[229–234].

1.2. Boron aluminum/gallium nitride system

Previous studies on aluminum-based group III–nitride materials have shown desirable structural and electronic properties with tunable direct bandgap that can cover the entire UV spectral band. These studies highlighted the increase in the optoelectronic active area of devices, where UV light emission could be enhanced fourfold by incorporating boron, but they lack any direct empirical demonstration[235]. While Liu *et al.* have theoretically investigated the spontaneous polarization and piezoelectric constants of wurtzite $B_xGa_{1-x}N$ and $B_xAl_{1-x}N$ ($0 \leqslant x \leqslant 1$) ternary alloys and concluded that they are not piezoelectric for boron concentrations of 75% and 87%, respectively[236], the miscibility of gallium and aluminum in BN are still under study. However, they are projected to have very low miscibility in BN at normal growth temperatures as the boron miscibility in AlN and GaN is evidently very low as well (a maximum of 14.4% boron content in single-phase wurtzite $B_xAl_{1-x}N$ films was reported by Li *et al.*)[237–242]. For both unstrained ternary $B_xGa_{1-x}N$ and $B_xAl_{1-x}N$ alloys, Teles *et al.* used first-principles calculations to observe very high critical temperatures of roughly 9000 and 9500 K that cause broad miscibility gaps between BN and binaries GaN and AlN, which is attributed to the large lattice mismatch between these compounds[240, 241].

Hexagonal boron nitride (h-BN) has attracted a considerable amount of attention because of the unique combination of properties it exhibits[243], including its wide bandgap energy isostructural with graphite[141, 244–248], low relative permittivity[249–251], high thermal conductivity[252, 253], and chemical inertness. It typically exhibits p-type behavior because of acceptor-like vacancy formation[254]; when grown on sapphire substrates, oxygen impurities diffuse from the substrate during high temperature growth, acting as substitutional donors[255]. The presence of these donors causes donor-acceptor pair (DAP) recombination involving carbon deep level acceptors[256, 257]. Despite that and its simple crystal structure, the nature of its bandgap configuration (i.e., direct vs. indirect) remains debatable[258–274]. In 2016, Cassabois, Valvin, and Gil provided evidence that h-BN has 5.955 eV indirect energy bandgap[275]. Through phonon-assisted two-photon absorption measurements, they demonstrated that h-BN exhibits phonon-assisted optical transitions that arise from the observation of a thermal distribution of excitons in the high-energy tail of the different emission lines. More evidence of the indirect nature of h-BN energy bandgap is the observation of different phonon replicas of the free exciton at 5.76 and 5.86 eV, which agree with the calculation results. Although the authors demonstrated the indirect bandgap nature of h-BN, there are many uncertainties that remain to be addressed more deeply and clearly. One of them is the strong emission line at 5.76 eV, at which even stimulated emission has been observed; this seems infeasible if the material has an indirect bandgap. Significantly more investigation need to be conducted to verify the optical transition of h-BN and the mechanism of the phonon-assisted emission if h-BN is an indirect material[275]. In 2017, Laleyan *et al.* demonstrated that the critical challenges that hindered the development of efficient DUV photonic devices with aluminum-rich $Al_xGa_{1-x}N$ can be addressed by magnesium dopant-free $Al_xGa_{1-x}N$/h-BN nanowire heterostructures[276]. They observed enhanced emission from AlN (at around 210 nm [$E \approx 5.76$ eV], with an IQE of up to 80% at 20 A/cm^2), which can be attributed to surface passivation effects from the h-BN shell. In 2019, Schué *et al.* observed a thermally stable bright luminescent emission at 215 nm ($E \approx 5.76$ eV) from single crystal bulk h-BN, with the lowest-energy exciton having a binding energy of around 300 ± 50 meV (determined using *ab initio* calculations)[258] . Moreover, the dispersion of excitons in h-BN has revealed the presence of direct exciton at about 100 meV above the indirect one, which is responsible for the maximum of absorption in bulk h-BN, illustrating the origin of the Stokes shift observed in h-BN[277, 278]. These results are consistent with highly efficient phonon-assisted luminescence.

In 2018, Pierucci *et al.* demonstrated the controlled growth of h-BN on graphite using MBE via van der Walls epitaxy[279]. Fig. 4 illustrates the obtained film with scanning electron microscopy (SEM) images. They found that this type of heterostructure produces sharp bands, while h-BN and graphite mostly retained their original electronic band structure.

2. Group III–nitride crystal structure and material properties

2.1. Wurtzite crystal structure

Of all groups of III–nitride compound semiconductors, devices based on $Al_xGa_{1-x}N$ are ideally suited for UV and DUV device design and fabrication because of the tunability of pho-

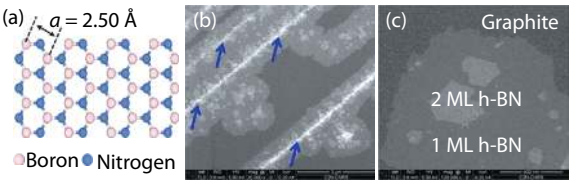

Fig. 4. (Color online) (a) Crystal structure of single layer h-BN. (b) SEM image of h-BN growth on HOPG demonstrating nucleation from HOPG in terrace steps pointed out by the blue arrows (darker contrast areas represent the underlying HOPG substrate while the lighter contrast areas represent regions of h-BN epitaxial growth). (c) High resolution SEM image of an h-BN island displaying areas of single and bilayer growth and part of exposed HOPG substrate. Reprinted with permission from Ref. [279]. ©2018, AIP Publishing.

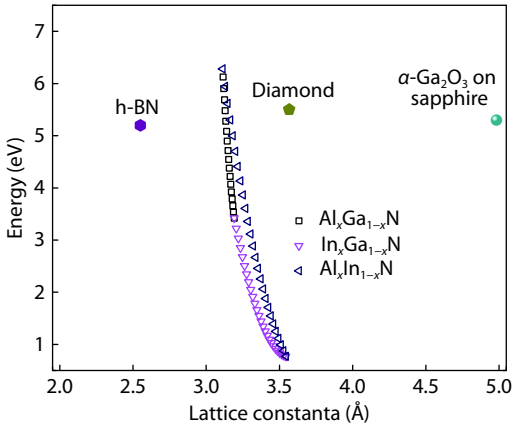

Fig. 5. (Color online) Plot of bandgap energy versus lattice constant a value of the (Al, In, Ga)N material system[280], α-Ga_2O_3[281–284], h-BN[275], and diamond, at room temperature.

toemission and photodetection wavelengths from about 200 to 364 nm by adjusting the AlN mole fraction. Because GaN crystal structures can be assimilated as cubic if the hexagonal planes are slided, the crystal lattice constants of group III–nitride semiconductors can be determined considering that each crystal forms a cubic lattice; hence, the lattice constant can be determined using the following expression:

$$a_{\text{cubic}} = \sqrt[3]{\sqrt{3}a_{\text{w}}^2 c_{\text{w}}}, \tag{2}$$

where a_{w} and c_{w} are the *a*-axis and *c*-axis, respectively, of the lattice of the wurtzite structure. Fig. 5 shows the bandgap energies of III–V semiconductor materials as functions of their lattice constants. The $Al_xGa_{1-x}N$ equilibrium structure is the wurtzite where all atoms are tetrahedrally coordinated with atoms of the opposite type.

The wurtzite structure is represented in Fig. 6(a) and is made of two hexagonal close-packed lattices perpendicular to the substrate (*c*-direction). The lattice constants are $a = b \neq c$ and the lattice angles are $\alpha = \beta = 90°$ and $\gamma = 120°$. For the case of GaN and AlN a = 3.1880 and 3.1127 Å, respectively, while c = 5.1856 and 4.9816 Å, respectively[285]. It is also noteworthy that in such compounds, the ratio *c/a* varies from the ideal value, denoting some degree of distortion. Fig. 6(b) shows the different crystallographic planes of the wurtzite structure. Most of group III–nitride-based LEDs and lasers have *c*-orientation (polar); however, research has also focused on semipolar (*a*- and *r*-planes)[286] and non-polar (*m*-

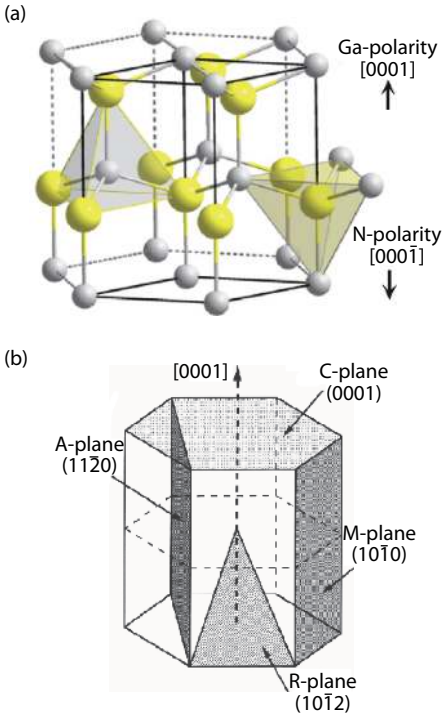

Fig. 6. (Color online) (a) Wurtzite structure. (Reprinted from [https://commons.wikimedia.org/wiki/File:Wurtzite_polyhedra.png]. Image stated to be in the public domain). (b) Wurtzite planes. Reprinted with permission from Ref. [288]. ©2017, IOP Publishing.

plane) because of a reduction in the polarization field and QCSE[287]. Two types of polarity are present in the wurtzite crystal structure, as it is not invariant with the inversion alongside the *c*-axis. This implies that the nitrogen atoms and the metal atoms exchange each other, causing crystallographic polarity, where the *c*-direction is the polar direction. Fig. 6(a) shows the [0001] and [000$\bar{1}$] directions that can be described as parallel to the Ga–N bond pointing toward the gallium and nitrogen atoms. Therefore, films grown along the [0001] or [000$\bar{1}$] directions are gallium- or nitrogen-polar, respectively. This is of essential significance for III–V nanowire growth and device design.

Spontaneous polarization in III–V semiconductors has detrimental effects through band bending[289, 290]. It results from the partially ionic bond between nitrogen anions and metal cations, although the chemical bonds in III–V materials are primarily covalent. Polarization vector points toward the [000$\bar{1}$] direction that is parallel and anti-parallel to the growth direction of nitrogen-polar and gallium-polar films. A summary of group III–nitride physical properties is provided in Table 2.

2.2. Polarization-induced fields

One of the principal causes of low IQE values in group III–nitride-based optoelectronic devices is the significant polarization fields built-in by the non-centro-symmetric nature of the atomic bonds. In a multilayer heterostructure, the spatial gradient of the polarization across the interfaces causes the formation of fixed charges, resulting in band bending and in turn, separation of carriers[319]. Hence, polarization fields are generally undesirable in light-emitting devices, as they hamper the integrity of the electronic and optical properties of the devices, reducing their performances. In the wurtzite crystal structure, spontaneous and piezoelectric polariza-

Table 2. Crystallographic[291–294], mechanical[291, 292, 295–300], thermal[291, 293, 294, 301–314], and optical properties[305, 315, 316] of select wurtzite group III–nitride semiconductors at room temperature.

Property	AlN	GaN	InN
Lattice constant (Å)	$a = 3.1127 \pm 0.0003$	$a = 3.1880 \pm 0.0001$	$a = 3.53$–3.548
	$c = 4.9816 \pm 0.0005$	$c = 5.1856 \pm 0.0005$	$c = 5.69$–5.76
Energy bandgap (eV)	6.2	3.44	0.69
Poisson's ratio	0.287 and 0.216[a]	0.37 and 0.33[b]	0.14–0.20[c]
Thermal expansion coefficient (10^{-6} K^{-1})	$\alpha_{\parallel} = 4.2$[d]	$\alpha_{\parallel} = 5.59$[f]	$\alpha_{\parallel} = 3.1$
	$\alpha_{\perp} = 5.3$[e]	$\alpha_{\perp} = 3.17$[g]	–
Thermal conductivity (W/(m·K))	319	230	800
Specific heat (J/(g·K))	0.6	0.49	0.32
Young's modulus (GPa)	$C_{11} = 410 \pm 10$, $C_{12} = 149 \pm 10$, $C_{13} = 99 \pm 4$, $C_{33} = 389 \pm 10$, $C_{44} = 125 \pm 5$, $C_{66} = 120 \pm 10$	$C_{11} = 390 \pm 15$, $C_{12} = 145 \pm 20$ $C_{13} = 106 \pm 20$, $C_{33} = 398 \pm 20$ $C_{44} = 105 \pm 10$, $C_{66} = 123 \pm 10$	$C_{11} = 190 \pm 7$, $C_{12} = 104 \pm 3$ $C_{13} = 121 \pm 7$, $C_{33} = 182 \pm 6$ $C_{44} = 10 \pm 1$
Index of refraction	2.1–2.2[h]	2.4–2.7[i]	2.05–3.06[j]
Melting point (K)	3100	2538[l]	1800[m]

[a] For (0001) and (1210) orientations, respectively. [b] For (0001) and (1210) orientations, respectively. [c] In the biaxial strain condition[317]. [d] In the temperature range of 295–1075 K. [e] In the temperature range of 295–1075 K. [f] In the temperature range of 300–700 K. [g] In the temperature range of 300–700 K. [h] For λ = 300–240 nm. [i] For λ = 600–350 nm. [j] For λ = 1500–600 nm. [k] Under moderate nitrogen pressure. In vacuum, AlN starts to dissociate at 2200 K. [l] At atmospheric pressure. Calculated using least-squares fitted result as determined by molecular dynamics simulations. [m] N_2 pressures exceeding 100 kbar are necessary for InN stability[318].

tion fields are caused by the partly ionic bond that induces a small crystal distortion and the presence of strain, respectively. In gallium-polar films the spontaneous polarization (P_{SP}) is parallel to growth direction (positive z-direction), whereas in nitrogen-polar films, P_{SP} is antiparallel to growth direction. Most of the group III–nitride planar crystals are grown gallium-polar, while most of the nanowires are grown nitrogen-polar. However, this depends on the growth conditions, and polarity can be easily interchanged.

Because the piezoelectric polarization field (P_{PE}) is related to the internal crystal strain (ε), it can be described as the nonzero elements of the crystal strain tensor as follows:

$$\varepsilon_{xx} = \varepsilon_{yy} = \frac{a - a_0}{a_0}, \quad \varepsilon_{zz} = -2\frac{C_{13}}{C_{33}}\varepsilon_{xx}, \tag{3}$$

where a, a_0, C_{13}, and C_{33} are the equilibrium and strained values of the in-plane lattice constant and the elastic constants[320]. The piezoelectric polarization is then expressed as:

$$P_{PE} = \pm 2\varepsilon_{xx}\left(\varepsilon_{31} - \varepsilon_{31}\frac{C_{13}}{C_{33}}\right), \tag{4}$$

where, depending on the metal or nitrogen polarity, we have the plus or minus sign. For the specific cases of GaN, AlN, and InN in metal-polar condition, the term within the brackets is negative; therefore, P_{PE} is negative (polarization vector points the substrate); while in nitrogen-polar condition it is positive, as summarized in Fig. 7

Changes in the normal component of the polarization field, ΔP, cause the formation of fixed charges at the heterointerfaces with density $\sigma P = -\Delta P$ and the subsequent carrier separation due to band bending. In the case of MQW structures, the continuity equation of the displacement flux through the different interfaces can be expressed as follows:

$$\varepsilon_w F_w + P_w = \varepsilon_b F_b + P_b, \tag{5}$$

where w and b stand for well and barrier, respectively, and ε, F and P are the permittivity of the material, the built-in electric field, and the sum of spontaneous and piezoelectric polarization fields, respectively. F_w and F_b are given by the following:

$$F_w = \frac{(P_b - P_w)L_b}{\varepsilon_b L_w + \varepsilon_w L_b}, \quad F_b = \frac{(P_w - P_b)L_w}{\varepsilon_b L_w + \varepsilon_w L_b}, \tag{6}$$

solved in the limit of an infinitely periodic structure and when voltage drop across layers is equal to zero ($F_w L_w + F_w L_w = 0$, L is the layer thickness). Fig. 8 shows the MQW band bending and the misaligned electron–hole wavefunction that imply

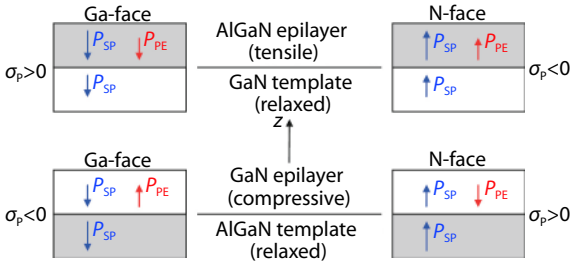

Fig. 7. (Color online) Polarization field directions and interface polarization charge distribution signs in GaN and $Al_xGa_{1-x}N$ structures. Reprinted with permission from Ref. [288]. ©2017, IOP Publishing.

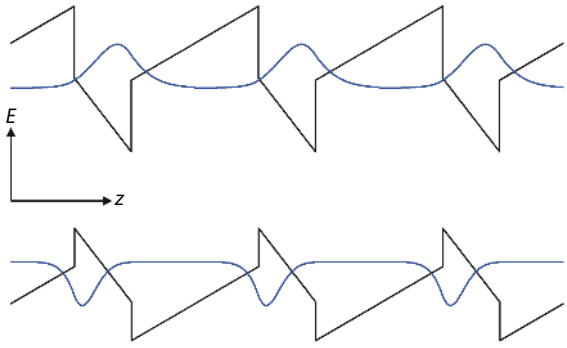

Fig. 8. (Color online) Conduction and valence band bending and electron and hole wavefunctions for the case of MQWs. Reprinted with permission from Ref. [288]. ©2017, IOP Publishing.

lower absorption and emission properties. Large field values of few MV/cm are usually present in *c*-plane III–nitride structures, causing the QCSE to dominate as the gap between conduction band minima and valence band maxima are reduced (red-shifted) by F_w.

2.3. Dislocations in $Al_xGa_{1-x}N$

Although $In_xGa_{1-x}N$-based devices demonstrate a remarkable resilience to high dislocation densities[321], dislocations are believed to be a significant factor limiting the efficiency of $Al_xGa_{1-x}N$-based LEDs[322–325]. $In_xGa_{1-x}N$/GaN-based light-emitting devices can be operational even with defect densities of up to 10^{11} cm^{-2} because of the effects of carrier localization[95, 321, 326, 327]. In any case, these defects are detrimental for optimal device performance, as they can increase leakage current densities (especially in visible wavelength LEDs)[328, 329], they act as nonradiative recombination centers, they reduce the IQE[330], and they decrease the lifetimes of LDs[331]. There are three types of dislocations in group III–nitrides that can be identified: (1) edge (*a*-type), mixed ([*a*+*c*]-type), and screw (*c*-type) dislocations[332], and each type of dislocation can be expressed using a Burgers vector (*b*) as is illustrated in the following[333, 334]:

$$b_{\text{edge}} = \frac{1}{3}\langle 11\bar{2}0\rangle, \quad b_{\text{mixed}} = \frac{1}{3}\langle 11\bar{2}3\rangle, \quad b_{\text{screw}} = \frac{1}{3}\langle 0001\rangle. \tag{7}$$

The defect density across a structure is directly influenced by epitaxial growth conditions of the materials on designated substrates. Because of its optical and thermal properties as well as its relatively low cost when compared to free-standing GaN substrates, sapphire is commonly employed as a substrate for the growth of group III–nitride light-emitting devices[335–337]. However, large lattice and thermal mismatches hamper their optoelectronic performances. For instance, sapphire and AlN exhibit a 13% lattice mismatch that causes high density of TDs at the interface between a sapphire substrate and an AlN buffer layer[338, 339], propagating toward the device active regions, and also causes lower IQEs[340, 341].

Moreover, due to the higher sticking coefficient and lower surface mobility of aluminum adatoms[342–344], $Al_xGa_{1-x}N$ epitaxial growth results are more challenging, compared to the GaN counterpart, having larger adatom mobility. For this reason, the growth of $Al_xGa_{1-x}N$ material results in 3D islands as aluminum adatoms are incapable of moving from their point of impact to energy favorable places. As the islands merge with each other, high-density defects such as grain boundaries and dislocations grow (mosaic model)[345], with densities in the range of 10^{10}–$10^{11}$$cm^{-2}$ for AlN, much higher compared to GaN (10^8 cm^{-2})[346]. Another theory, the *nucleation model*, that has been supported by transmission electron microscopy (TEM) studies and atomic force microscopy (AFM) studies[347], suggests that the TDs nucleate in the low-temperature nucleation layer extend in subsequent layers. Regarding the techniques used to reduce the TDs in the device active region, we can find superlattices growth[348], insertion layer growth[349], growth of graded layers[350], and temperature- and nitrogen-controlled growth[349, 351].

2.4. Efficiency droop

Efficiency droop is a phenomenon mainly associated with the reduction in $In_xGa_{1-x}N$/GaN-based LED efficiencies as the injection current densities increase. Despite the fact that this phenomenon is very pronounced in blue and green LEDs, it also affects UV devices to a lesser degree[352, 353]. Fig. 9 demonstrates the droop in quantum efficiency with increasing injection current for three LEDs emitting at different wavelength regimes, namely UV, blue, and green LEDs. The decrease in quantum efficiency is caused by the increase in bias voltages and subsequent device heating[354–358], which in turn reduces quantum efficiencies. Such efficiency droops were attributed to carrier delocalization[359, 360], electron leakage attributed to polarization mismatches[357, 361, 362], drift-leakage mechanism[363] tunneling leakage currents[364], poor carrier injection[365, 366], low hole mobility in heavily p-doped aluminum-rich $Al_xG_{1-x}aN$[367], and Auger recombination[122, 123, 368, 369]. However, there is still no conclusive evidence to pinpoint the origin of this problem[370]. For the special case of UV LEDs, the droop is supposedly less prominent, which can be attributed to the significantly reduced Auger losses in wide-bandgap semiconductors because of the substantial reduction in the coupling between electron and hole bands with increasing bandgap. However, the Coulomb interaction that assists in the Auger transitions is significantly stronger in these materials because of the smaller dielectric constants and the subsequent larger exciton binding energies, rendering the importance and strength of this argument inconspicuous[371–373].

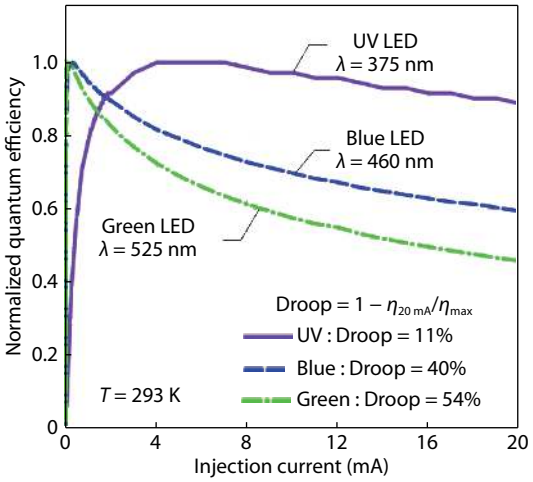

Fig. 9. (Color online) Efficiency versus injection current curves of GaN-based UV, blue, and green LEDs, demonstrating a decrease in quantum efficiency with increasing injection current. Green LEDs were shown to have the most prominent efficiency droop. Reprinted with permission from Ref. [352]. ©2013, John Wiley & Sons.

The IQE of a light-emitting device takes into account how efficiently holes and electrons can be extracted from their respective injection layers and the percentage of carriers that recombine radiatively to emit photons, and is expressed as[104]

$$\text{IQE} = \frac{\text{rate of photon generation}}{\text{rate of carrier injection into active region}}. \tag{8}$$

The IQE can also be expressed as the ratio of the injected current that leads to radiative recombination in the device active region to the total injected current (I_{tot}) as fol-

lows:

$$\mathrm{IQE} = \frac{I_r}{I_{tot}} = \frac{I_r}{I_r + I_{nr}}, \quad (9)$$

where I_{nr} is the current that is dissipated in nonradiative processes and transitions. When I_{nr} dominates (i.e., $I_{nr} > I_r$), efficiency droop takes place. I_{nr} includes the carrier losses attributed to SRH recombination, Auger recombination, and carrier leakage outside the QWs. Hence, I_{tot} can be expressed as

$$I_{tot} = I_r + I_{SRH} + I_{Auger} + I_{leakage}. \quad (10)$$

Inside the QWs, the carrier recombination current can be expressed as

$$I_{QW} = I_r + I_{SRH} + I_{Auger} = qV_{QW}(AN + BN^2 + CN^3), \quad (11)$$

where q is the elementary charge value and V_{QW} is the total volume of the QW region. A, B, C are the three recombination coefficients of SRH, radiative, and third-order processes (such as Auger losses), respectively, and N is the excess density of carriers involved in the respective recombination processes. The leakage current can be represented by[366]

$$I_{leakage} = \alpha(I_{QW})^2. \quad (12)$$

By combining Eq. (9) with Eq. (12), we can express the IQE as follows

$$\mathrm{IQE} = \frac{\eta_{inj} + BN^2}{AN + BN^2 + CN^3}, \quad (13)$$

where η_{inj} is the carrier injection efficiency. For $In_xGa_{1-x}N$ QWs, the A, B, and C coefficients are in the order of 10^7 s^{-1}, 10^{-11} cm^3/s, and 10^{-33} cm^6/s, respectively, from first-principle study by Delaney, Rinke, and Van de Walle[374, 375]. Researchers have been seeking alternatives to solve issues related to low IQEs; one approach is the employment of nanostructured devices, such as nanowire LEDs. Because of the reduced polarization fields stemming from effective strain relaxation and low dislocation densities, as well as reduced Auger recombination, group III–nitride nanowires can potentially represent a solution to solve the aforementioned device efficiency issues[58, 376].

2.5. Thermodynamic photoinduced disorder

In the case of group III–nitride semiconductors, it is broadly assumed that the photocarrier relaxation dynamics consist of a fast initial decay process in the subpicosecond range, followed by a slower decay described by the ultrafast carrier thermalization dynamics, the carrier trapping by surface states, and the slower carrier cooling effects, respectively[377]. This process allows for radiant refrigeration, suggesting that they are solid-state radiative heat pumps[378] as illustrated by David *et al.* for the case of group III–nitride LEDs[379]. Hence, a more in-depth understanding of the opto-electrothermal properties of group III–nitride semiconductors through an entropic point of view is necessary to further understand their applicability and operational and thermal stability[380] in multifunctional applications[381]. In 2017, we employed temperature-dependent photoluminescence to examine the photoinduced entropy of an ensemble of thick $Al_{0.18}Ga_{0.82}N$ nanowires[382] and $In_{0.32}Ga_{0.68}N$/GaN p–i–n double-heterostructure nanowire photodiodes[383], shown in Fig. 10, by correlating the energy exchange during the photoexcitation and photoemission processes of the light–solid reaction and the generation of photoinduced entropy of the nanowires using temperature-dependent (6 to 290 K) photoluminescence. We defined the photoinduced entropy as a thermodynamic quantity that represents the unavailability of a system's energy for conversion into work due to luminescence refrigeration[384]. We also studied the ultrafast dynamics of photocarriers using wavelength-integrated time-resolved photoluminescence down to the subnanosecond regime. We investigated the thermodynamic behavior alongside the photocarrier dynamics in GaN-based nanowires because an in-depth understanding of the factors that govern energy transfer processes, and the transport of free carriers through them, is crucial to realizing creative designs of reliable and efficient high-power electronics and LEDs. Strong exciton localization in metal-rich clusters, carrier trapping by surface defect states, and thermodynamic entropy effects were examined and related to the photocarrier dynamics.

In $In_{0.32}Ga_{0.68}N$/GaN nanowires, we observed a rising trend in the amount of generated photoinduced entropy of the system above 250 K, while a fluctuating trend in the generated entropy of the system below 250 K was observed. The fluctuations in the generated entropy stabilized between 200 and 250 K. It was supposed that the amount of generated photoinduced entropy of the $In_{0.32}Ga_{0.68}N$ active region increase as more nonradiative channels became activated, and more shallowly localized carriers settle into deeply localized states (allowed for through the strong localization in indium (In)-rich clusters)[385, 386]; thereby, additional degrees of uncertainty related to the energy of states involved in thermionic transitions were attained. For the $Al_{0.18}Ga_{0.82}N$ nanowires, we observed a fluctuating trend in the generated entropy of the system below 200 K, with a fluctuation frequency that was significantly lower than what we had previously observed in $In_{0.32}Ga_{0.68}N$. In contrast to the sharp increase in generated entropy at temperatures close to room temperature in $In_{0.32}Ga_{0.68}N$, an insignificant increase was observed in $Al_{0.18}Ga_{0.82}N$, indicating lower degrees of disorder-induced uncertainty in the wider bandgap semiconductor. We conjectured that the improved atomic ordering in $Al_xGa_{1-x}N$[387–390] induced lower degrees of disorder-related uncertainty related to the energy of states involved in thermionic transitions; in keeping with this conjecture, we observed lower fluctuation frequency below 200 K.

3. Innovative material growth mechanisms and device fabrication techniques

Advancements in growth techniques made it possible to achieve highly improved optoelectronic device performance through high-quality single-crystal material growth[391–393]. Since GaN exhibits a smaller degree of lattice mismatch with the lattice of AlN compared with that of sapphire (a = 4.7576 Å and c = 12.9834 Å at 25 °C)[293], the epitaxial growth of GaN films on AlN/sapphire templates can be conveniently carried out[394, 395]. This assisted in the reduction of dislocations on overgrown active regions. In 1983, Yoshida, Misawa, and Gonda achieved significant improvements in the electrical and luminescent properties of reactive MBE-grown GaN/AlN

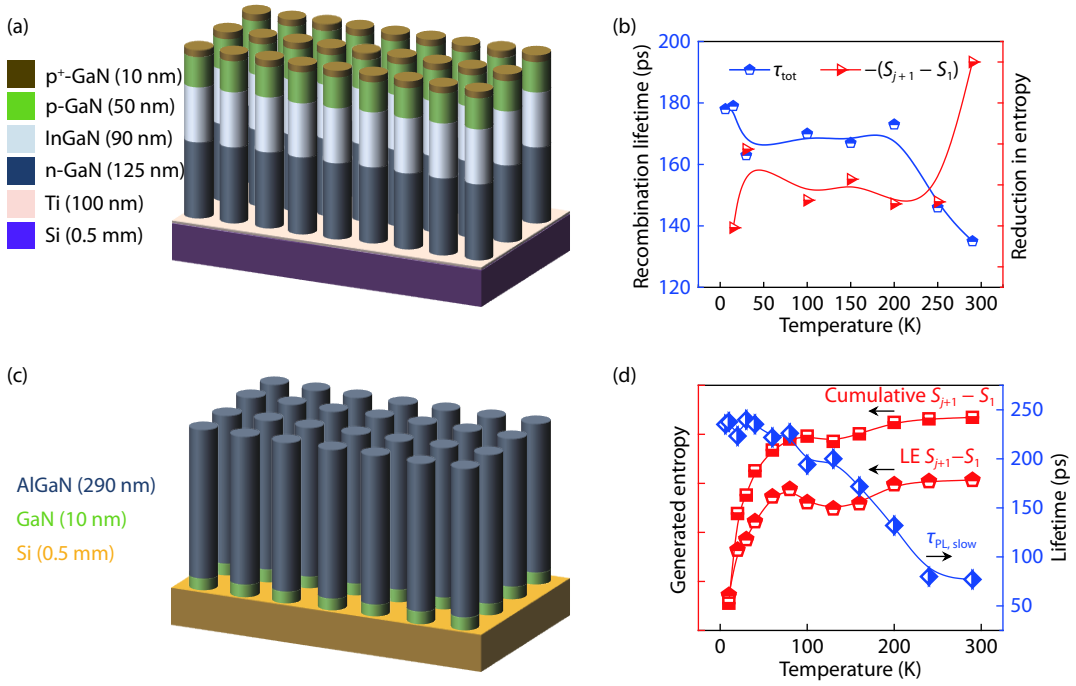

Fig. 10. (Color online) (a) Schematic and layer structure of the $In_{0.32}Ga_{0.68}N$/GaN p–i–n nanowires and (b) the evolutions in the total carrier recombination lifetime and the amount of entropy generation with temperature. (Reprinted with permission from Ref. [383]. ©2017, AIP Publishing). (c) Schematic and layer structure of the $Al_{0.18}Ga_{0.82}N$ nanowires and (d) the integrated and low-energy-peak-related evolution of the amount of entropy generation with temperature. Reprinted with permission from Ref. [382]. ©2017, AIP Publishing.

heterostructures on sapphire substrates[396], while in 1989, Akasaki *et al.* achieved high-crystal-quality and crack-free overgrown GaN epitaxial layers on AlN acting as a low-temperature buffer layer using MOVPE in 1986[397], while in 1989, Akasaki *et al.* prepared GaN and $Al_x Ga_{1-x}N$ ($0 \leqslant x \leqslant 0.4$) films by the preceding deposition of the AlN buffer layer, where they considerably reduced the mosaicity of and microscopic fluctuations in the crystallite orientation[339]. Another milestone step for growing high quality group III–nitrides was accomplishing p-type doping in GaN. In 1989, Amano *et al.* realized magnesium-doped GaN by low-energy electron-beam irradiation (LEEBI) treatment, and the properties of the GaN p–n junction LED were reported for the first time[91]. The first blue LEDs consisting of p-GaN/n-$In_xGa_{1-x}N$/n-GaN double-heterostructures were fabricated in 1993 by Nakamura, Senoh, and Mukai[398]. Later, in 1996, Nakamura *et al.* demonstrated the first violet laser emitting at 417 nm based on $In_{0.20}Ga_{0.80}N$/GaN/$Al_xGa_{1-x}N$ heterostructures[94]. This breakthrough demonstrated the use of group III–nitride materials beyond the blue and green LEDs, though achieving p-type doping for $Al_xGa_{1-x}N$-based UV devices remains difficult as magnesium dopant demands more activation energy in group III–nitride semiconductors. For the first time, Asif Khan *et al.* reported the fabrication and characterization of a high-frequency GaN/$Al_{0.13}Ga_{0.87}N$-based heterojunction FET in 1994[399].

3.1. Nanostructured layer growth

3.1.1. Molecular beam epitaxy

In 2016, while addressing challenges encountered during growth of aluminum-rich $Al_xGa_{1-x}N$ nanowires for DUV optoelectronic devices, Zhao *et al.* demonstrated that such nanowires with significantly enhanced compositional uniformity can be realized through a new growth prototype other than the conventional nitrogen-rich growth conditions. They argued that they can a achieve precise control on the optical bandgap energy of the ternary $Al_xGa_{1-x}N$ nanowires by employing a GaN nanowire template and varying the substrate temperature while improving the aluminum/gallium compositional uniformity. They demonstrated $Al_xGa_{1-x}N$ nanowire LEDs, with emission wavelengths spanning from 236 to 280 nm[400]. Their key results are summarized in Fig. 11. The improved growth paradigm revolves around the idea that low nitrogen flow rates would enhance the surface migration of aluminum adatoms, causing a more uniform aluminum/gallium compositional distribution. This resulted in an accurate control on the emission wavelengths of ternary $Al_xGa_{1-x}N$ nanowires, which can be accomplished by altering the substrate temperature, instead of the conventional epitaxial way of varying aluminum and gallium beam equivalent pressures (BEPs)[99, 401–403].

Vuong *et al.* studied the optoelectronic properties of h-BN grown by PA-MBE. By combining AFM, spectroscopic ellipsometry, and photoluminescence spectroscopy in the DUV regime, they compared the quality of h-BN grown on sapphire and highly oriented pyrolytic graphite substrates. They were able to demonstrate DUV emission in h-BN, with an emission spectra peak at 235 nm, indicating the high optical quality of the MBE-grown h-BN. The h-BN epitaxial layers grown on highly oriented pyrolytic graphite have shown superior performance in the DUV regime down to 210 nm, compared to the same films grown on sapphire[404].

Liu *et al.* have demonstrated large-area AlN nanowall 214 nm LEDs grown on a sapphire substrate. Through temperature-dependent and power-dependent photoluminescence measurements and rate equation analysis, a relatively high internal quantum efficiency of about 60% was determined for the AlN

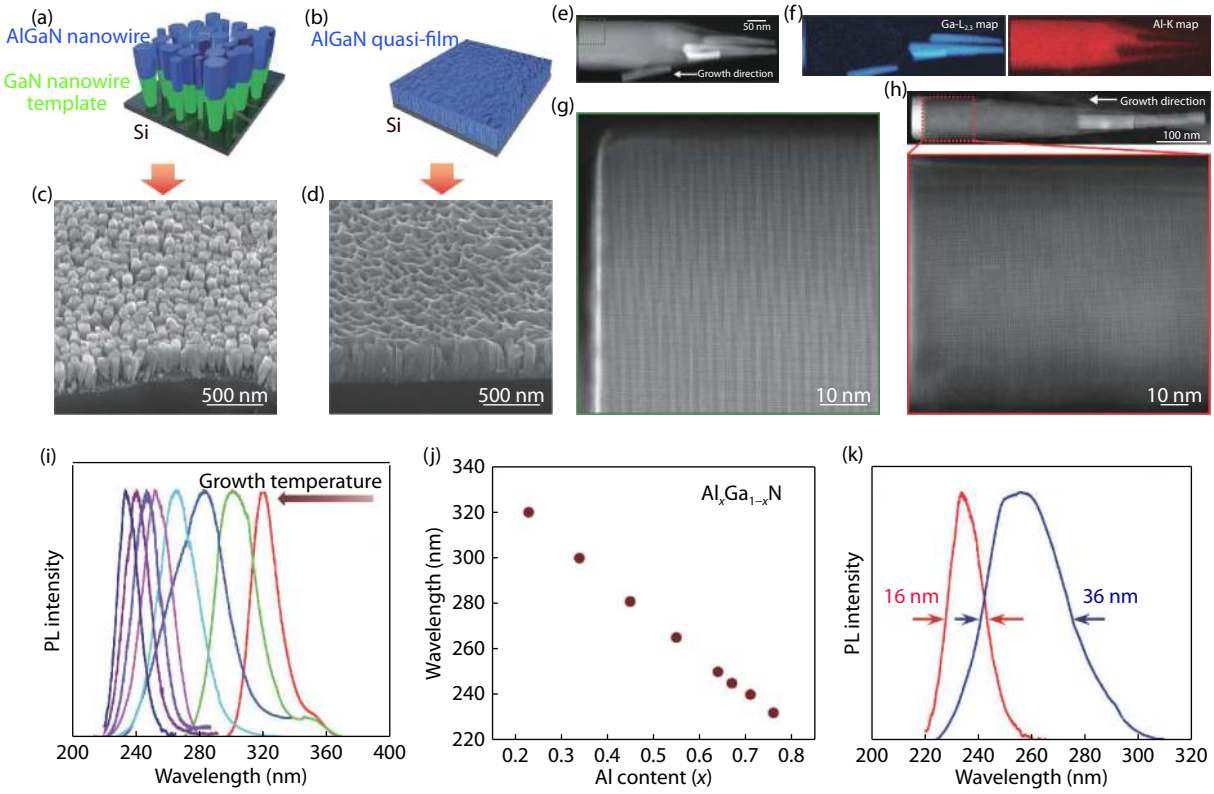

Fig. 11. (Color online) (a) Schematic illustration of $Al_xGa_{1-x}N$ nanowires grown on GaN nanowire templates (with a low nitrogen flow rate of 0.4 sccm) on a Si substrate. (b) Schematic of direct growth of $Al_xGa_{1-x}N$ nanowires on a Si substrate, forming an $Al_xGa_{1-x}N$ quasi-film. (c) Elevation-view SEM image of the $Al_xGa_{1-x}N$/GaN nanowires. (d) Elevation-view SEM image of highly coalesced $Al_xGa_{1-x}N$ nanowires grown directly on a Si substrate. (e) Low-magnification scanning transmission electron microscope (STEM) image of a single $Al_xGa_{1-x}N$/GaN nanowire and (f) the color-coded (green-bordered) electron energy loss spectroscopy (EELS) maps depicting the elemental distribution of Al and Ga. (g) High-resolution image of the $Al_xGa_{1-x}N$ segment in (e), showing the relative uniformity of aluminum distribution, with the thin bright band being the *p*-GaN contact layer. (h) Low-magnification STEM image of a single $Al_xGa_{1-x}N$/GaN nanowire grown with a high nitrogen flow rate of 1.0 sccm (the inset shows a high-resolution image taken from the $Al_xGa_{1-x}N$ segment) manifesting the remarkable atomic-scale compositional modulation. (i) PL spectra of ensembles of nanowires grown under substrate temperatures between 895 and 960 °C with a nitrogen flow rate of 0.4 sccm. (j) Evolution of the peak PL wavelength with AlN mole fraction. (k) PL spectrum (blue curve) of a nanowire sample grown with similar conditions as the sample emitting at 232 nm in (i) but with an increased nitrogen flow rate of 1.3 sccm. The latter is shown in (k), red curve. Reprinted with permission from Ref. [400]. ©2016, AIP Publishing.

nanowall structures at room temperature. A consistent blue-shift in the emission wavelengths was observed with decreasing nanowall widths because of the reduced distribution in tensile strain. The LEDs exhibited excellent current–voltage *I*–*V* characteristics, including a turn-on voltage of 7 V and current densities of greater than 170 A/cm^2 at 12 V[405].

3.1.2. Metalorganic vapor phase epitaxy

While $Al_xGa_{1-x}N$-based structures show significant importance in applications requiring DUV light sources, the absorption of UV light by p-type layers results in these devices suffering from low light extraction efficiencies (LEEs)[114, 136, 406–410]. To solve this issue, various methods have been proposed by a large body of research[114, 411, 412]. In this context, Jo, Maeda, and Hirayama utilized a transparent p-$Al_{0.70}Ga_{0.30}N$ layer that was synthesized primarily for enhancing the UV LEE, paving a promising path toward zero absorption property of output UV light[413]. The transparent p-$Al_{0.70}Ga_{0.30}N$ layer served as a contact layer and led to a higher LEE by using reflective metal electrodes. Conventionally, blue and UV LED structures incorporate p-type GaN contact layers, but these layers are not suitable for DUV LEDs because GaN layers absorb most of the output UV emission. Higher aluminum mole fraction $Al_xGa_{1-x}N$ epitaxial layers with highly transparent and highly conductive aluminum metal layers are crucial to obtain excellent DUV devices, but the fabrication process of realizing high quality p-type $Al_xGa_{1-x}N$ layers is difficult due to issues associated with the large activation energy of acceptors, resulting in low hole concentrations and low formation energies of compensation defects. Nevertheless, two 260 nm LEDs were fabricated on sapphire substrates by MOVPE, with one employing a nickel (Ni)/gold (Au) as metal electrode, while the other employed a Ni/aluminum metal electrode[413]. Both LEDs utilize p-type $Al_{0.70}Ga_{0.30}N$ layers with a magnesium concentration of 5×10^{19} cm^{-3} and have been thermally annealed at 950 °C in N_2 ambience. Regardless of the low hole concentration < 10^{16} cm^{-3}, by using highly transparent (> 95% transmittance) p-type $Al_{0.70}Ga_{0.30}N$ contact layer, the LED demonstrated an efficiency of 2%, similar to that of the LED employing p-type GaN contact layers. Furthermore, an enhancement of 3.4% in EQE was obtained in the LED employing a Ni/aluminum metal electrode compared to that employing a Ni/Au electrode. The aforementioned improved LED performance was attributed to hopping conduction by acceptor sites[184, 414, 415]. To date, numerous efforts have been made to improve the con-

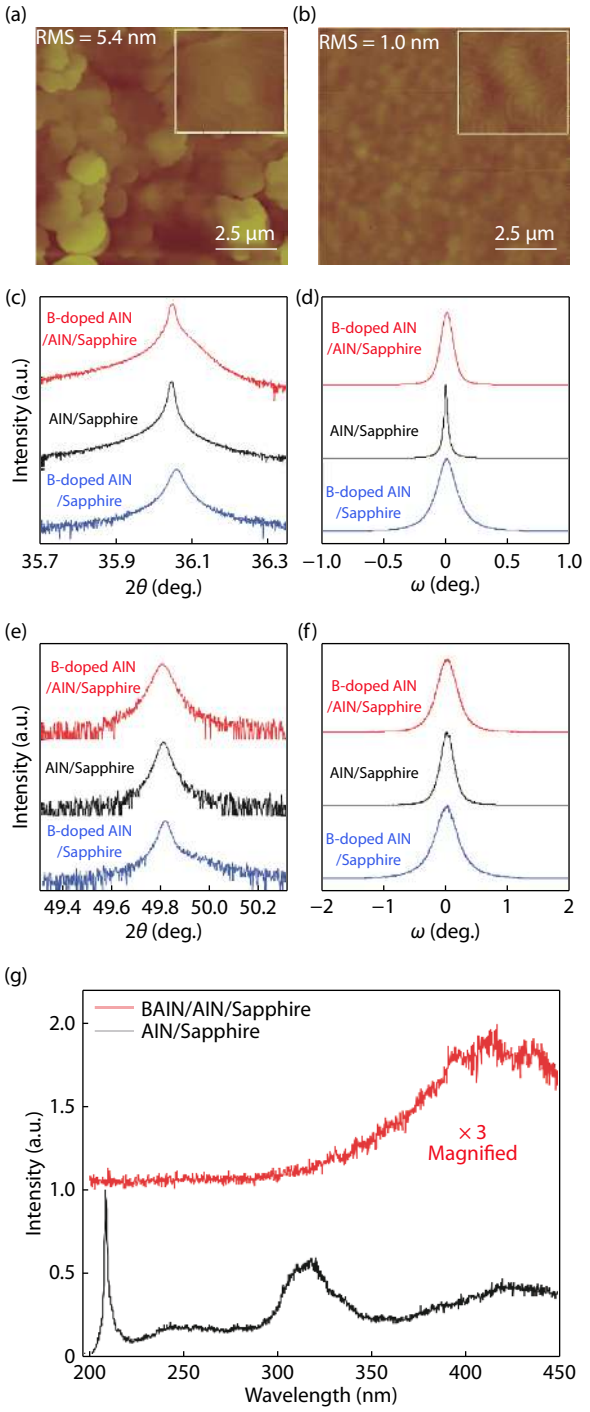

Fig. 12. (Color online) AFM images of the magnesium-doped $Al_xGa_{1-x}N$ layers showing enhanced RMS roughnesses of (a) 5.4 nm for $x = 0.35$ by continuous growth method and (b) 1 nm for $x = 0.43$ by metal-source FME. Reprinted with permission from Ref. [419]. ©2018, AIP Publishing. XRD characteristics of B-doped AlN/AlN/sapphire, AlN/sapphire, and B-doped AlN/sapphire samples. (c, d) Symmetric 0002 AlN reflections. (e, f) Asymmetric $10\bar{1}2$ AlN reflections. (g) Cathodoluminescence spectra of $B_xAl_{1-x}N$/AlN/sapphire and AlN/sapphire samples. Reprinted with permission from Ref. [154]. ©2018, John Wiley & Sons.

ductivity property of the p-type $Al_xGa_{1-x}N$ grown layers by increasing the hole concentration in magnesium-doped $Al_xGa_{1-x}N$ and decreasing its acceptor activation energy. In spite of several approaches developed to overcome this obstacle, including magnesium-delta doping[180, 416], co-doping[417], and polarization-induced doping[418], these structures involve wurtzite crystallographic orientations and suffer from high polarization effects, which result in even larger acceptor activation energies. During the $Al_xGa_{1-x}N$ growth process, applying nitrogen-rich conditions with large V/III ratios is favorable to achieve better magnesium incorporation and smoother morphology structures.

Metal-source flow-rate modulation epitaxy (FME) provides unique opportunities to realize high hole concentrations in magnesium-doped $Al_xGa_{1-x}N$. Luo *et al.* were able to demonstrate a hole concentration of about 2.3×10^{17} cm^{-3} at room temperature, nearly ten times higher than conventional growth procedures, with resistivities as low as 12.7 Ω·cm by implementing metal-source FME[419]. Owing to its smooth step-flow growth, improved surface morphology and crystalline quality were observed as a result of employing FME capability in enhancing the adatoms migration as seen in Figs. 12(a) and 12(b). The working principle of the FME technique is based on the interrupted flow rate of metal while a nitrogen source is continuously suppling, ensuring high nitrogen-rich conditions and keeping maximum V/III flow ratio. A slow growth rate of about 4 nm/min was observed by employing FME interrupted metal flow rate, and hence the Al(Ga) adatoms had sufficient time to migrate on terraces toward the steps. As a result, a highly efficient magnesium doping, with acceptor activation energies ranging between 20 and 22 meV, and a smooth surface morphology, with AFM root mean square (RMS) roughness of about 1 nm, compared to 5.4 nm by conventional growth method, were obtained. This can enhance quantum efficiency of DUV LEDs. The FME principle was also utilized to grow $Al_xGa_{1-x}N$/AlN distributed Bragg reflectors (DBR) with a reflectivity of 97% and a stopband of 6–9 nm at DUV wavelengths ranging between 220 nm and 250 nm[420]. The AlN molar fraction was regulated to obtain the required bandgap wavelength associated with the peak reflective wavelength of the $Al_xGa_{1-x}N$/AlN DBRs. The grown DBRs of optical quarter wavelength of the desired peak wavelength were grown using MOVPE at a temperature of 1130 °C and a pressure of 100 mbar, while assisted through the FME technique by continuously supplying trimethylaluminum (TMAl) and NH_3, while frequently interrupting the supply of trimethylgallium (TMGa). The AlN molar fractions in two samples were chosen to be 0.48 and 0.61 by controlling the growth thickness of the respective $Al_xGa_{1-x}N$ layer to be 400 nm and by varying the molar flowrate ratio TMAl/III between 0.35 and 0.44, respectively. For the FME-$Al_xGa_{1-x}N$, the AlN molar ration was controlled by tuning TMGa and TMAl period thicknesses and TMAl single period thickness. As a result, the atomic steps of DBR structure was fully strained to the AlN layer and became a defect-free surface and, hence, improved DBR reflectivity was attained. In this regard, we also reported the significant role of yttrium oxide (Y_2O_3)-doped hafnium oxide (HfO_2) on silicon dioxide (YDH/SiO_2) DBR having a high reflectivity of 99.9% at a wavelength of 240 nm with a stopband of 50 nm[421]. The YDH/SiO_2 DBRs were deposited by RF magnetron sputtering (RF power of 75 W and argon gas flow of 25 sccm) on UV-grade sapphire substrates. The YDH/SiO_2 DBR thicknesses were kept at 30 nm with RMS roughness of about 1.2 nm and 1.07 nm for YDH and SiO_2, respectively. Because of its higher bandgap energy resulting from doping HfO_2 by Y_2O_3, YDH films are semi-transparent in the UV-C band, rendering them

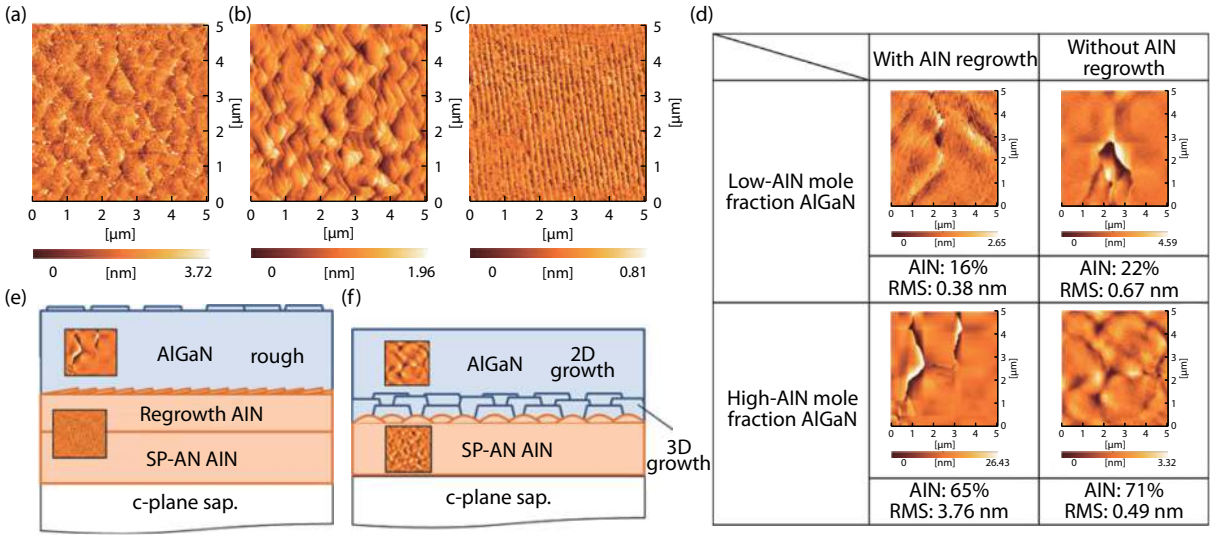

Fig. 13. (Color online) (a–c) Surface roughness enhancement trend (from 0.54 to 0.13 nm). In (a) an AFM scan of a sputtered AlN/sapphire template after high-temperature annealing is shown, while in (b), the AlN/sapphire template in (a) scanned after the temperature had been increased to 1250 °C and maintained for three minutes in an NH_3 ambience. (c) AFM scan of the 1 μm-thick AlN homoepitaxial layer grown on the SP-AN AlN/sapphire template. (d) AFM images of the surface morphologies of $Al_xGa_{1-x}N$ heteroepilayers with different AlN mole fractions; these heteroepilayers were grown on sputtered and annealed AlN/sapphire templates with and without AlN regrowth layers. (e) Schematic illustrations of high-AlN mole fraction $Al_xGa_{1-x}N$ grown on sputtered and annealed AlN/sapphire templates: (e) with AlN regrowth layer, (f) without AlN regrowth layer. Reprinted with permission from Ref. [128]. ©2018, John Wiley & Sons.

prime candidates for use in DUV devices to enhance optical performance.

Instead of employing p-type $Al_xGa_{1-x}N$ layers, several efforts have been made to substitute these low conductivity layers with BN[422]. One of the advantages of epitaxially grown BN is its small magnesium acceptor activation energy of approximately 31 meV[423] compared to about 150–300 meV in mixed-phase BN[424–426], and approximately 170–510 meV in $Al_xGa_{1-x}N$[162, 167, 169, 427]. Imura *et al.* conducted a detailed investigation on boron incorporation on the growth of high-quality AlN layers (Figs. 12(c)–12(g))[154]. They have confirmed a homogeneous boron concentration of 2×10^{21} cm^{-3} (≈ 2% of the atomic composition) in the MOVPE-grown AlN epitaxial layers. A conventional AlN/sapphire sample exhibited different emissions, namely near-band-edge emission at 208.4 nm and likely defect-related emissions at 315 nm and 400–450 nm originating from complexes of aluminum vacancies ($(V_{Al}$–complex$)^{2-}$) and/or oxygen impurities (V_{Al}^{-3}–O) with dot-shaped defects along the $\{11\bar{2}3\}$ facet oxygen impurity incorporation into AlN[428–430]. The boron-doped AlN layers demonstrated weak and broad emission at 400–450 nm, as depicted in Fig. 12(g). The quenched emissions in these layers were mainly attributed to the fact that analysis of the incorporation of boron into AlN layers at the nanoscale revealed that the boron atoms were not integrated in the AlN crystal, forming amorphous[431] and/or disordered precipitates that prevented the formation of perfect $B_xAl_{1-x}N$ alloys by suppressing the 2D layer-by-layer synthesis of AlN.

Hakamata *et al.* investigated the combination of sputtering and MOVPE to study surface quality and optical properties of MOVPE-grown AlN and $Al_xGa_{1-x}N$ epitaxial layers on sputtered and annealed AlN/sapphire templates[128]. Sputtering is known for its capability to deliver high quality and large size AlN layers through inexpensive means by adopting annealing at high temperatures. The cause of the high crystallinity in sputtered films is post annealing, which enhances the coalescence of AlN columnar structure and reduces possible dislocations in sputtered layers[432–435]. In their study, an AlN thin film was sputtered on *c*-plane sapphire substrates and then annealed (SP-AN) at 1700 °C. Then, the MOVPE growth processes of AlN and $Al_xGa_{1-x}N$ epitaxial layer on SP-AN AlN/sapphire were detailed. Homogeneous epitaxial layers (homoepilayers) of AlN were grown in two stages. Stage I occurred when growth temperature reached and kept at 1250 °C for three minutes in H_2 and NH_3 ambience. Stage II occurred when a 1-μm-thick AlN layer was grown at 1250 °C. The AFM roughness measurements (Figs. 13(a)–13(c)) show significant enhancements in the RMS roughness (from 0.54 to 0.13 nm) as the fabrication process continued from the high temperature annealing through stages I and II. Fig. 13(c) shows high surface quality step-terrace structure of the grown AlN homoepilayer on SP-AN AlN template. As mentioned previously, this improvement was attributed to the enhancement of the AlN epitaxial layer coalescence. Moreover, oxide or oxynitride column crystals observed at the surface that contained aluminum were removed due to the high temperature annealing process in an NH_3 ambience. On the other hand, the $Al_xGa_{1-x}N$ heterogeneous epitaxial layer (heteroepilayer) growth process resulted in high- and low-AlN concentrations because of reactor replacement during growth process on the plane- and the 1-μm-thick AlN regrowth layers on SP-AN AlN/sapphire template. Fig. 13(d) depicts the morphology of the grown $Al_xGa_{1-x}N$ samples with high and low AlN mole fractions, with and without the AlN regrowth layer. By embedding the regrown AlN layer, dislocations were observed on the surface as 3D growth that assisted in relaxing the resultant compressive strain. Conversely, without the AlN regrowth layer, 3D growth arises because of the roughness of surfaces at grown layer interface, and hence the majority of dislocations were bent[436–438]. It was detected that while growing thick $Al_xGa_{1-x}N$ layers, the growth process followed 2D be-

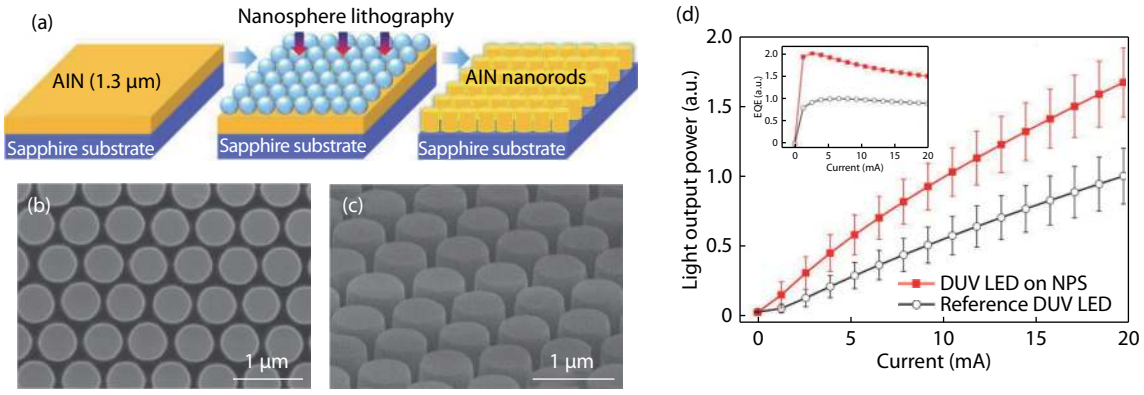

Fig. 14. (Color online) (a) Schematic diagram of silica nanosphere lithography, (b) plan-view, and (c) bird's-eye-view SEM images of the fabricated NPS. (d) Plot of the average LOP as a function of the injection current measured from 50 LEDs at room temperature. The relative EQE, estimated by dividing the photocurrent by the injection current, is also shown in the inset. The OP of the DUV LEDs on NPS shows much higher LOP by 67% than that of the reference DUV LED at the injection current of 20 mA. Reprinted with permission from Ref. [445]. ©2017, AIP Publishing.

havior, which led to a flat surface structure.

Sun *et al.* have conducted AlN growth experiments by MOVPE to investigate the effects of TMAl pretreatment on the surface roughness and crystalline quality of grown AlN layers on *c*-plane sapphire substrates[439]. In their study, AFM results revealed that precise pretreatment time is the most important factor to realize TD-free smooth surfaces on AlN films. The pretreatment time of five seconds showed the smoothest surfaces, whereas samples without pretreatment or those that underwent a pretreatment time of greater than ten minutes suffered from TDDs, pits, and rougher surfaces. Mixed nitrogen- and aluminum-polarity exhibited in the AlN films was believed to be responsible for low surface roughness on the untreated sample because of the presence of Al_xO_yN interlayer between AlN nucleation layer and the sapphire substrate[440, 441]. For 0–5 s of TMAl pretreatment, RMS roughness values of less than 1 nm indicated excellent morphologies because the nitrogen-polarity areas vanished by inhibiting the oxygen diffusion from sapphire substrate[442]. By increasing the pretreatment time beyond 40 s, RMS roughness values increased as nanocolumns were observed at the surface as a result of the formation of 3D islands at the nucleation layer and the presence of 3D growth mode[443]. Finally, the MOVPE growth of single-crystalline AlN-on-sapphire-based ring resonators with high optical *Q* factors were demonstrated by Bruch *et al.*[36]. A 1.1 μm-thick AlN grown on sapphire substrate was fabricated using a single masking lithography process, where a FOx-16 hydrogen silsesquioxane (HSQ) mask and then 300 nm poly(4-styrenesulfonic acid) (PSSA) were spun before sputtering a 10 nm-thick Au to transfer the pattern to the AlN via an inductively coupled plasma (ICP) etching process. Compared to the two-step fabrication process reported earlier by Liu *et al.*[444], this proposed fabrication process enabled high etching selectivity that led to etching the entire AlN structure, and subsequently, more confinement of the visible mode was achieved.

3.2. Device fabrication

In this section, we discuss various methodologies to enhance the performance of DUV devices. Most challenging to realizing growth of group III–nitride semiconductors are the high TDDs resulting from the lattice mismatch and/or thermal expansion mismatch between foreign substrates such as sapphire or silicon and the grown AlN epitaxial layers. On the other hand, the growth process of AlN on native substrates such as AlN or GaN is limited due to the high cost and unavailability of inexpensive commercial substrates. Various approaches have been discussed to address the sapphire substrates' TDDs[137]. Patterned sapphire substrates (PSS) are one of these promising approaches to suppress TDs where nanometer-to-micrometer-sized patterns are transferred to the sapphire substrate by additive or subtractive techniques. The main advantage of the PSS is its ability to minimize TDDs through selective area growth and by improving the photon scattering by uneven sapphire surface. Recently, crack-free DUV LED epitaxial layers were obtained on a four inch *c*-plane sapphire substrate by epitaxial lateral overgrowth (ELO) on periodic air-voids-incorporated nanoscale patterns as shown in Figs. 14(a)–14(c)[445]. Since the ELO technique demonstrates unique properties in hindering TDD effects and increasing the output power of UV LEDs, it has been widely utilized in micro-patterned substrates. However, it is considered an expensive growth process due to first, higher temperature (above 1300 °C) requirements, which are necessary for the migration of aluminum adatoms, and second, long epitaxial time necessary to realize coalesces thick of 10 μm of AlN. In their experiment, Lee *et al.* conducted an ELO of AlN on NPS at a relatively lower growth temperature of 1050 °C, which resulted in a faster coalescence time than previous micro-patterned substrates at much lower cost. During the MOVPE growth process, the air-voids patterns helped to relax the tensile strength issues and minimize TDD effects, and subsequently, its output power reaches 67%, compared to a reference UV LED (Fig. 14(d))[445].

Another method to reduce the fabrication cost of the ELO process of AlN is decreasing the coalescence thickness via nanosphere lithography (NSL). In this regard, Dong *et al.* successfully utilized nanopatterned sapphire substrates (NPSS) that coalesce after only 3 μm of growth, compared to 10 μm for microstructure patterning methods, and hence, reduce fabrication time[323]. They were able to enhance the performance of 282-nm $Al_{0.40}Ga_{0.60}N/Al_{0.50}Ga_{0.50}N$-based DUV LED by NSL technique, where TDs in the vicinity of nano-voids are suppressed as they bend in the direction of voids sidewalls as depict in Figs. 15(a)–15(c). The EQE was achieved around 3.45% with an enhancement of approximately 98%,

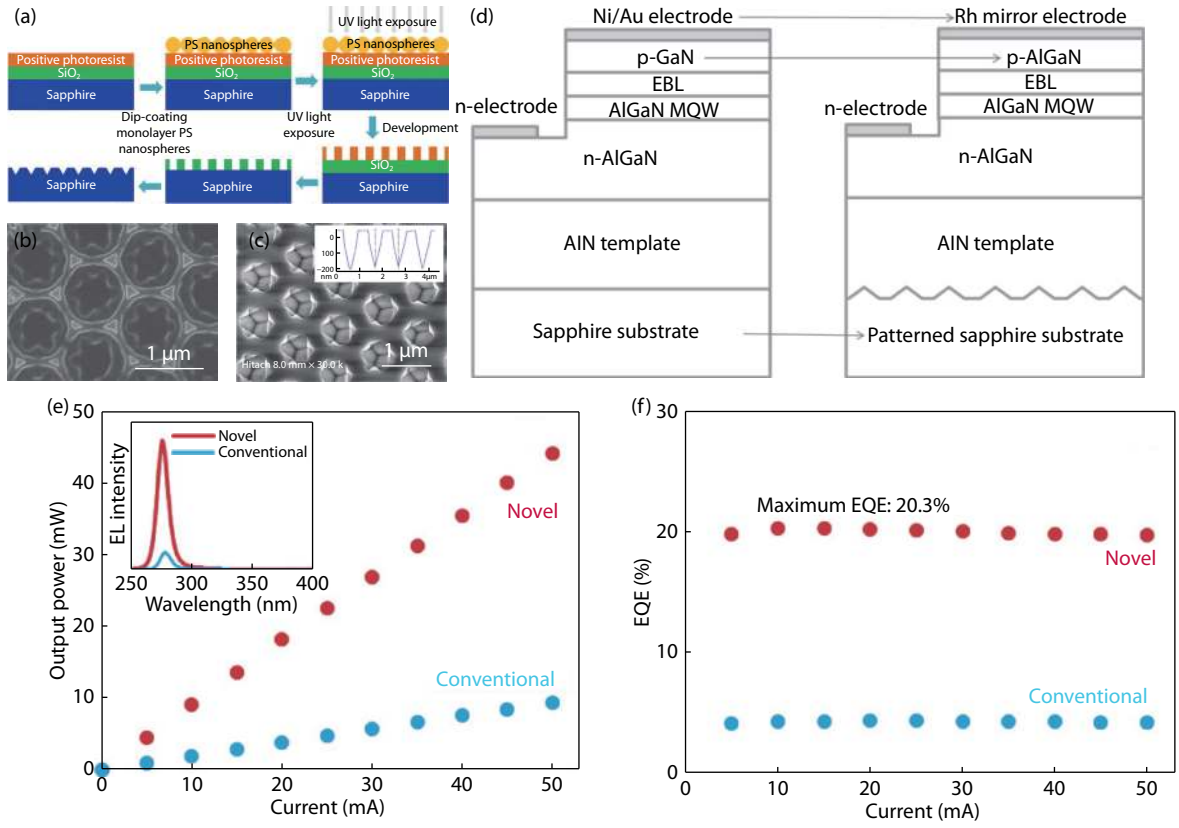

Fig. 15. (Color online) (a) Schematic of the fabrication process flow to create nanopatterns on a sapphire substrate. SEM images of the (b) patterned PR and (c) wet-etched NPSS. The inset in (c) shows the line profile of the patterns of NPSS by AFM measurement. (Reprinted with permission from Ref. [323]. ©2013, AIP Publishing). (d) Schematics of conventional (left) and novel UV LED structures (right). In the novel UV LED structure, a transparent p-type $Al_{0.65}Ga_{0.35}N$:Mg contact layer, a Rh mirror electrode, a PSS, and encapsulation resin are introduced. (e) Output power–current and (f) EQE–current characteristics. Blue and red dots show the characteristics of the conventional and novel UV LED structures, respectively. Inset in (e) shows the EL spectra of the UV LEDs at a DC of 20 mA. (Reprinted with permission from Ref. [114]. ©2017, The Japan Society of Applied Physics).

compared with conventional at sapphire substrate, by adopting NSL and wet etching mechanisms. In another report, Zhou *et al.* demonstrated the effect of different sizes of cone-shaped-PSS on performance of UV LED emitting at 375 nm[446]. They noticed that TDDs are in a decreased trend associated with increasing pattern sizes and with the PSS filling factor. The measured light output power (LOP) of the UV LED grown on a large PSS with a fill factor of 0.71 was 131.8% higher than that of the UV LED grown on a small PSS with a fill factor of 0.4. This behavior can be attributed to the reduction of GaN island density and to an increased lateral overgrowth area of GaN, which leads to higher optical performance of the device. The growth process of GaN epitaxial layers on larger PSS including AlN nucleation layer (15 nm of thickness) increases the transition time from 3D island to 2D coalescence, which resulted in a better IQE performance. In a subsequent report, a light-extraction mechanism based on an Rh mirror electrode and a transparent p-type $Al_{0.65}Ga_{0.35}N$:Mg contact layer was studied by Takano *et al.*[114]. They achieved a 20% enhancement in EQE at 275 nm of wavelength. In their design, a conventional $Al_xGa_{1-x}N$-based LED is modified into a UV LED structure by utilizing the following features: (1) crack-free AlN on the PSS, (2) $Al_{0.65}Ga_{0.35}N$:Mg p- type contact layer, (3) mirror electrode, and (4) silicon encapsulation resin. The encapsulation resin helped to reduce optical loss and reached 89% transmission. Implementing Rh mirrors into the LED structure results in an improvement in output power from 3.9 to 18.3 mW at 20 mA, and in the EQE from 4.3% to 20.3%, in comparison with conventional LEDs. Increased multireflection of light in the chip and absorption reduction effectively improved the device performance (Figs. 15(d) and 15(e)).

Fig. 16 shows a moth-eye micro-arrays which was fabricated on the back of sapphire platform to significantly increase the LEE by weakening the total internal reflection (TIR)[447]. Consequently, a high degree of optical polarization (DOP) of 81.8% is obtained for DUV LED utilizing moth-eye micro-arrays, compared to a standard DUV LED of DOP of 64.7%. The high performance of LEE (Fig. 16(f)) is due to the impact of moth-eye micro-arrays on improving the TE/transverse magnetic (TM) modes.

Similar to sapphire substrate integration in the DUV LED fabrication process, growing AlN epitaxial layers on silicon substrate is of critical importance due to the availability, suitability, and low-cost of silicon substrates. Nevertheless, the lattice mismatches between silicon (111) and AlN (0001) are approximately 19% in the $[11\bar{2}0]_{AlN}$ and $[1\bar{1}00]_{AlN}$ directions; however, they are around 0.74% between the $[1\bar{1}00]_{AlN}$ direction and silicon (110), which leads to enhancement in device efficiencies[448]. Although several reports discussed the growth process of AlN layers on different direction-oriented silicon substrates, few reported high quality AlN on silicon (110). In 2017, Shen *et al.* reported a V-profile pit free high quality AlN surface with clear atomic steps grown on silicon (110) orienta-

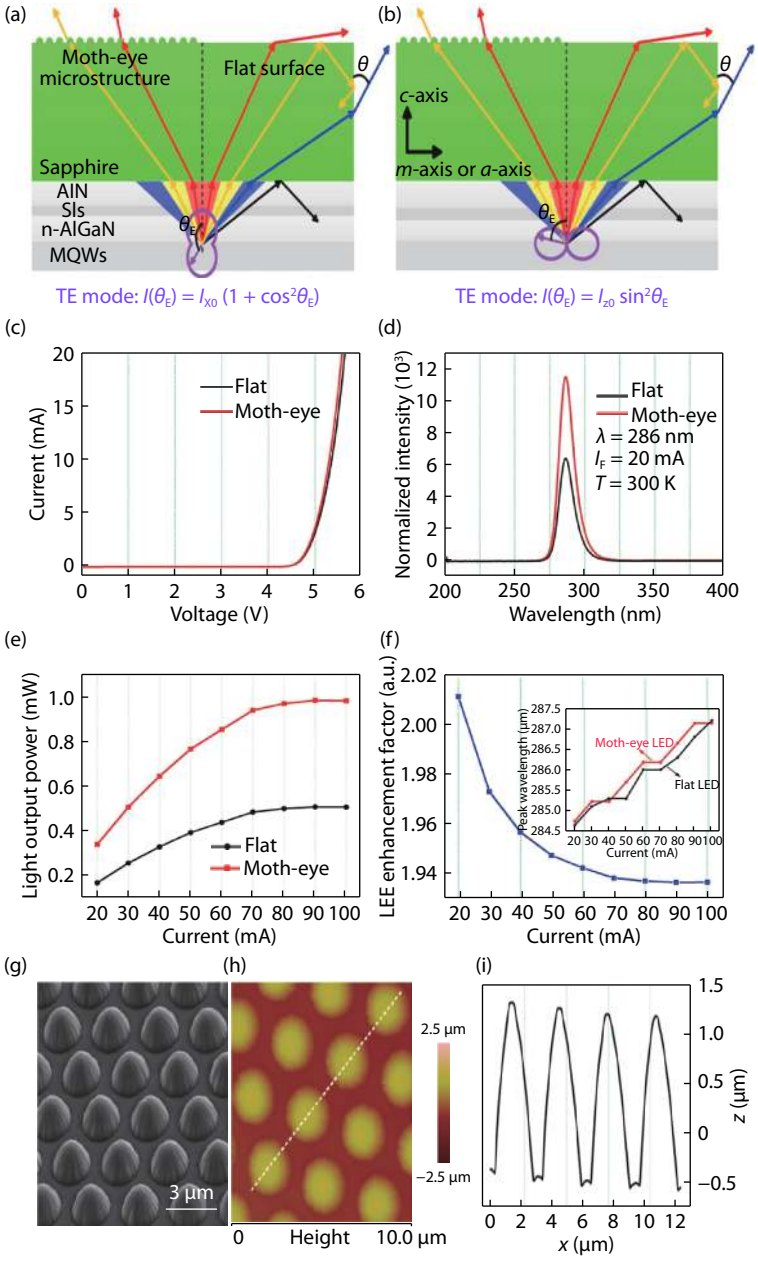

Fig. 16. (Color online) (a) TE and (b) TM mode light propagation characteristics in moth-eye DUV LEDs reported by Wang *et al*.. The purple line represents TE/TM mode light emission intensity profile inside the MQWs, whereas the shadow areas correspond to the sapphire surface and sidewall radiation areas, as well as TIR radiation areas. (c) *I*–*V* characteristics; (d) normalized spectra; (e) LOP; (f) LEE enhancement factor. The inset depicts the peak wavelengths at different current injection levels. (g) SEM and (h) AFM image of moth-eye microstructure. (i) The structure size along the dash line in the AFM image. Reprinted with permission from Ref. [447]. ©2018, American Chemical Society.

tion substrate that exhibits high resolution structure via high resolution X-ray diffraction measurements as illustrated in Fig. 17[448]. The key factor in achieving high resolution structure is by controlling growth rates and AlN layer thicknesses.

Micro-circle-patterned silicon substrate (mPSIS) is another configuration technique to enhance the quality of grown AlN template on silicon substrate[449]. Different mPSIS sizes were fabricated to grow thick AlN template with the help of NH_3 pulsed-flow and ELO in the MOVPE growth process. During the lithography process, the ICP bias powers were modified to obtain different mPSIS sizes. MPSIS pattern sizes of 1.7 and 2.0 μm were fabricated on two silicon substrate samples by selecting ICP power of 10 W for 50 min of etching and ICP power of 5 W for 40 min of etching, respectively. During the growth process, the temperature decreased from 1390 to 1380 °C while NH_3 increased from 5 to 6 sccm to enhance the AlN surface. The sample with larger pattern size (i.e 2.0 μm) showed better results in term of AFM roughness of 1.6 nm, compared to 3.5 nm for the other sample with 1.7 μm pattern size. Also, TEM images showed smoother surface for the large size pattern sample as an atomic step with high quality terraces observed. The TDs become less pronounced in the large size pattern sample than in the small pattern size sample, as the dislocations bend and terminate at sidewalls.

4. Critical review of the current status of nitride-based optoelectronic devices

4.1. Light-emitting diodes

$Al_xGa_{1-x}N$-based DUV LEDs have been dominating re-

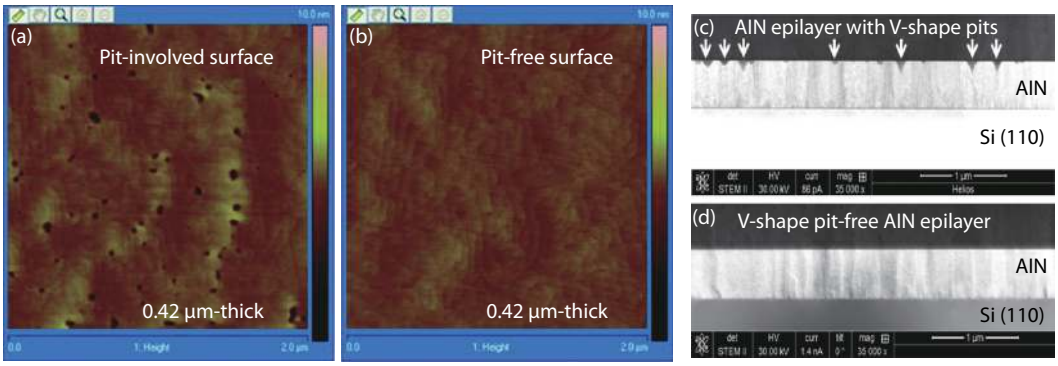

Fig. 17. (Color online) AFM images showing the effect of several growth rates on two AlN layers, where the growth rates are (a) 250 nm/h and (b) 50 nm/h. Sides-sectional STEM images depicting two 420 nm-thick AlN/Si(110) samples (c) with and (d) without V-shape pits by controlling the growth rate. Reprinted with permission from Ref. [448]. ©2017, Royal Society of Chemistry.

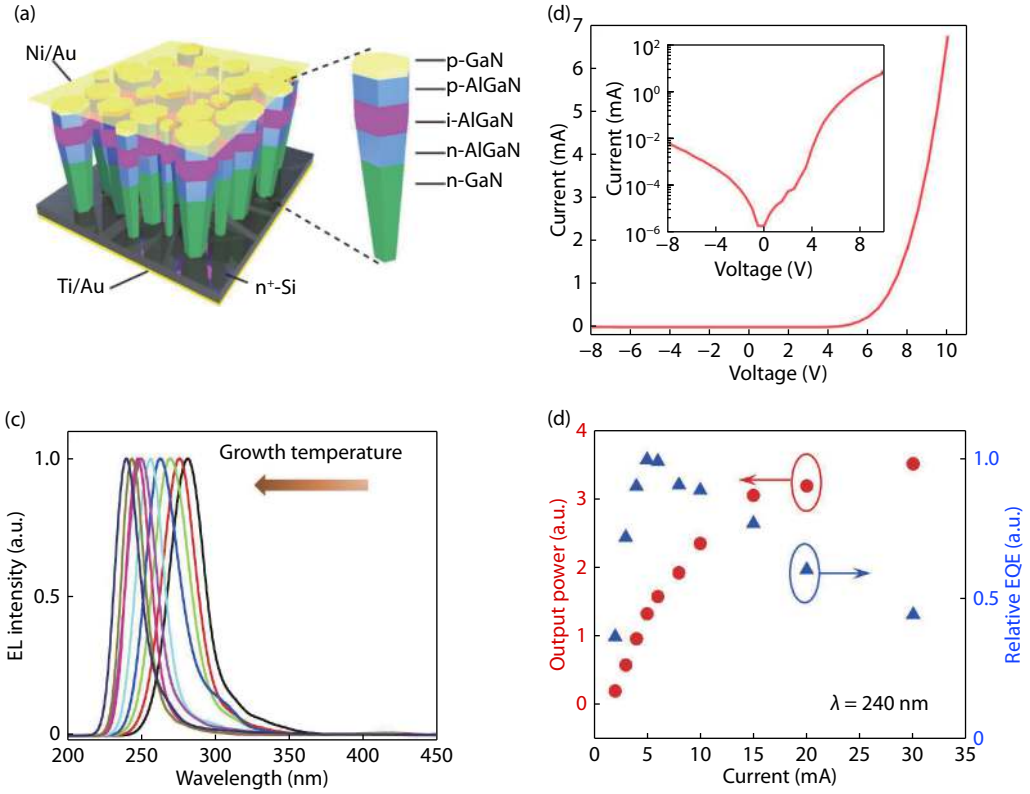

Fig. 18. (Color online) (a) Schematic illustration of the p–i–n $Al_xGa_{1-x}N$ nanowire-based LEDs grown on titanium (Ti)/Au on Si by Zhao *et al.* (b) Linear and semilogarithmic scale *I*–*V* characteristics curve of an $Al_xGa_{1-x}N$ nanowire UV LED emitting around 240 nm. (c) EL spectra measured from several nanowire LEDs with different AlN mole fractions under an injection current of 20 mA. (d) *L*–*I*–*V* and relative EQE curves of a UV device emitting around 240 nm. Reprinted with permission from Ref. [400]. ©2016, AIP Publishing.

search in the last few years[450–462]. Most notably, using the growth paradigm described earlier, Zhao *et al.* were able to fabricate defect-emission-free $Al_xGa_{1-x}N$ nanowire LEDs operating in the UV-C regime, and attributed the enhanced current conduction characteristics to the improved acceptor magnesium dopant incorporation in the $Al_xGa_{1-x}N$ nanowires and the subsequent acceptor impurity band conduction[184, 400, 463]. Fig. 18(a) shows the device schematic, while the *I*–*V* characteristics of an $Al_xGa_{1-x}N$ nanowire LED with emission wavelength around 240 nm are depicted in Fig. 18(b). Fig. 18(c) depicts the room-temperature EL spectra measured from several devices. The output power measurements (*L*–*I*–*V*) of a UV LED device are shown in Fig. 18(d).

4.2. Photodetectors

Taking advantage of high absorption coefficients (>10^5 cm^{-2}) and wide bandgap energy, group III–nitride semiconductor alloys have attracted remarkable attention for UV photon detection owing to their prospective applications in solar radiation monitoring[464], missile plume detection[465–467], biological treatment[468], and non-line-of-sight (NLOS) communication[469]. Compared to other wide bandgap materials (e.g., ZnO, SiC, and Ga_2O_3), the large bandgap tunability of group III–nitrides also allows the absorption or cut-off wavelength to be engineered by simply changing the alloy composition, an easy tailoring for demanding applications that require high signal-to-noise ratios (SNR) and spectrum se-

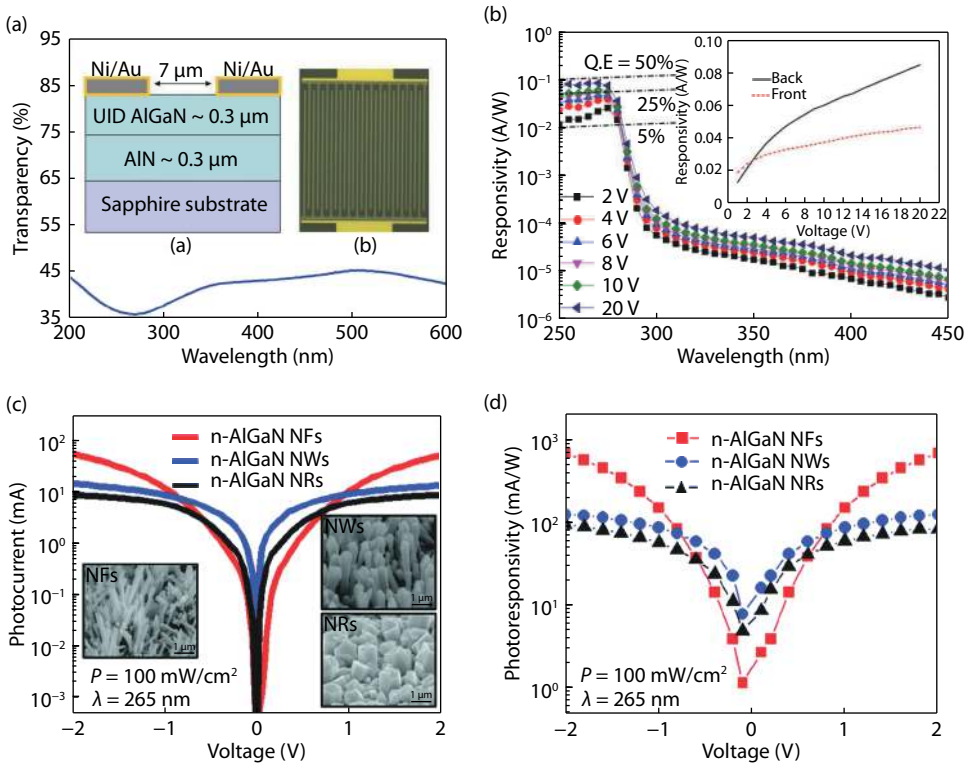

Fig. 19. (Color online) (a) Transmission spectrum of Ni/Au interdigitated electrodes used in an MSM-based PD. Inset shows the typical structure of an $Al_xGa_{1-x}N$-based MSM PD. (b) Corresponding responsivity spectrum of a bottom-illuminated $Al_{0.40}Ga_{0.60}N$-based MSM PD. Inset shows the comparison of measured responsivity for front and bottom-illumination mode. (Reprinted with permission from Ref. [494]. © 2013, AIP Publishing). Comparison between n-$Al_xGa_{1-x}N$ nanoflower, nanowire, and nanorod PDs in terms of (c) photocurrent and (d) photoresponsivity spectra. (Reprinted with permission from Ref. [508]. ©2018, Royal Society of Chemistry).

lectivity. Apart from that, high thermal and chemical stabilities of group III–nitride material system stands out in harsh environments, compared to conventional silicon-based detectors, which have limited operating temperature range and require extra protective packaging[470–473]. In addition, silicon-based photodetectors typically have low photoresponsivity in the UV regime of operation due to low penetration depth of UV-wavelength photons in silicon[474]. Photomultiplier tubes (PMTs) were also suggested as alternative devices in UV photon detection[475]; however, the associated bulky volume and high operating voltage hinders further applications of PMTs[476]. Following the development of a more mature epitaxial growth for group III–nitride compounds, $Al_xGa_{1-x}N$-based photodetectors (PDs), which can cover the wavelength range from 200 to 360 nm depending on the aluminum composition[477], show promise for achieving highly reliable UV photodetectors and in alleviating the aforementioned issues, and are the subject of active research in UV and DUV photon detection, opening up a plethora of potential applications in the future.

The early work on GaN-based PDs started in in 1992 by Khan *et al.*, where a photoconductive UV detector with high spectral responsivity (R) of 2000 A/W (200 to 365 nm) was demonstrated[478]. This is the first reported UV sensor based on as-deposited single-crystal insulating GaN films. Since then, various types of $Al_xGa_{1-x}N$-based PDs, particularly for photon detection in the solar-blind region (i.e., 230 to 280 nm), such as Schottky-type PDs[479–481], metal–semiconductor–metal (MSM) PDs[482–486], HEMTs[487], and p–i–n heterojunction PDs[488–491], have been demonstrated. Among these, MSM-based PDs attract noteworthy attention, owing to their ease of fabrication, low stray capacitances, and high switching speed for monolithic integration on photonic circuits[480, 492, 493]. Another notable advantage of MSM-based PDs is that p-type doping of $Al_xGa_{1-x}N$ is not necessary, putting it in dominance when compared to p–i–n structured PDs. In addition, depending on the device design, MSM-based PDs can be illuminated through either front or bottom illumination. For example, Wang *et al.* compared performance differences in terms of responsivity and EQE of $Al_{0.40}Ga_{0.60}N$-based MSM UV PD, in both illumination modes[494]. For a photodetector, the EQE can be determined using

$$\mathrm{EQE} = \frac{I_{\mathrm{PC}}}{P_{\mathrm{IL}}}\frac{hc}{q\lambda} = R\frac{hc}{q\lambda}, \tag{14}$$

where I_{PC} is the generated photocurrent, P_{IL} is the illuminated optical power, h is Planck's constant, c is speed of light, and λ is operation wavelength. Fig. 19(a) shows the transmission spectrum of a Ni/Au interdigitated electrode commonly used in MSM-based PDs, where low transparency values of less than 45% are observed in the UV wavelength region. In the case of front-illumination, fully transparent or semi-transparent interdigitated electrodes are deemed pivotal in order to increase light absorption efficiency. In such cases, this requirement may complicate the fabrication process because of the necessity for highly UV transparent electrodes, such as graphene[142, 495, 496], carbon nanotubes[497, 498], and metal–oxide composites[499, 500]. Compared to the front-illumination mode, higher EQEs are typically observed with bottom-illumin-

ation configuration owing to first, the smaller refractive index of sapphire substrates, compared to $Al_xGa_{1-x}N$ layers, and second, higher absorption efficiency because of the absence of light shadowing metal electrodes[494] . Fig. 19(b) shows the higher responsivity (inset) and corresponding EQE (around 50%) obtained in the case of a bottom-illuminated PD, compared to a front-illuminated PD. A detailed examination of the influence of AlN buffer layers and $Al_{0.50}Ga_{0.50}N$ absorber layer for a bottom-illuminated MSM-based PD was presented by Brendel *et al.*[484]. A threefold enhancement of EQE (up to 20% at 20 V) was observed for a 100 nm-thin $Al_{0.50}Ga_{0.50}N$-based bottom-illuminated MSM PD. At the end of 2015, the same group reported an EQE of up to 67% at 50 V in a bottom-illuminated 500 nm-thick $Al_{0.50}Ga_{0.50}N$ absorber layer of an MSM-based PD[485]. Apart from the influence of absorbance layers, the effects of asymmetric electrodes on the EQE of bottom-illuminated $Al_{0.40}Ga_{0.60}N$- and $Al_{0.50}Ga_{0.50}N$-based MSM PDs have also been discussed[483, 501]. The dependence of the EQE on carrier lifetime and transit time in $Al_{0.25}Ga_{0.75}N$-based MSM PD at different operation voltages has been reported by Schlegel *et al.*[502]. To produce high performance MSM-based PDs with low leakage currents and high responsivities, various counter-move investigations include correlation between lateral leakage current and screw dislocation density (ρ_{screw})[503]. Edge TDs and suppression of leakage current using a surface passivation layer in MSM-based PDs have also been widely discussed[504, 505]. Other than that, carrier collection mechanisms and influence of core threading dislocation in MSM-based PDs have recently been reported by Walde *et al.*[506]. This work provides insightful observations to the advantage of open-core threading dislocation in $Al_{0.50}Ga_{0.50}N$ layers for improving the EQE of MSM-based PDs, in which dislocation is typically held accountable for high leakage currents in $Al_xGa_{1-x}N$-based LEDs. Prior works present valuable device designs and optimization methods for high-performance solar-blind MSM-based PDs. Recently, Yoshikawa *et al.* reported a true solar-blind $Al_{0.60}Ga_{0.40}N/Al_{0.50}Ga_{0.50}N$-based MSM PD with a cut-off wavelength at 280 nm and a high rejection ratio of 10^6[507]. The improved photocurrent and high rejection ratio achieved in this work was attributed to the control of carrier density in the 2D electron gas (2DEG) layer through a decreased thickness of $Al_{0.60}Ga_{0.40}N$ barrier layer. Although a high responsivity of up to 10^6 A/W, comparable to values achieved with PMTs, was achieved; nevertheless, slow response time due to persistent photoconductivity effect was simultaneously observed.

Despite the advantages of bottom-illuminated configuration PDs, the thermal and lattice mismatches between conventional sapphire substrates and group III–nitride materials still persist. While paving the way toward the solar-blind regime of operation, high aluminum composition of greater than 40% are required to provide the aforementioned applications in the solar-blind region. High TDDs and thermal structural cracking developed during the epitaxial growth, especially at increased aluminum contents, hinder the device performance of $Al_xGa_{1-x}N$-based PDs, which requires low charge generation rates and stray capacitances. In order to alleviate these issues, various methods have been reported, including selective area growth[509], pulse atomic epitaxial technique (PALE)[510], and crack-free AlN template layer use. Cicek *et al.* demonstrated a solar-blind $Al_{0.40}Ga_{0.60}N$-based p–i–n PD with a high EQE of up to 89% (at 5 V reverse bias voltage) and a responsivity of around 176 mA/W (at zero bias voltage) by using various optimized growth and structural design methods[511]. Improvements in structural characteristics were attributed to the use of a crack-free AlN template layer, a highly conductive silicon-indium co-doped[512] $Al_{0.50}Ga_{0.50}N$, and an improved magnesium-doped $Al_{0.38}Ga_{0.62}N$ layer grown using MOVPE. In a recent work, Han *et al.* proposed the use of metal–insulator–semiconductor (MIS) structures in solar-blind $Al_{0.45}Ga_{0.55}N$-based PDs, as a competitive alternative to the conventional p–i–n structure[513]. The latter is impeded by growth of high-aluminum-content p-doped $Al_xGa_{1-x}N$ layers. The demonstrated bottom-illuminated MIS-based structure exhibited a high EQE of 70.6% (at 3 V reverse bias voltage) at 270 nm with a relatively fast rise time of 1.4 ns. The significance of optimized AlN template in growing high quality $Al_xGa_{1-x}N$ PD structures has been substantially highlighted. Chen *et al.* reported a solar-blind $Al_xGa_{1-x}N$-based p–i–n PD grown and fabricated on a high quality and low residual compressively stressed AlN template[514]. They attributed the improved performance of the device (EQE at 68.8% and response speed of 6.5 ns) to the insertion of a mesothermal AlN (MT-AlN) interlayer to assist in strain relief along the growth direction. Similar work on optimized growth conditions for producing high quality and crack-free $Al_xGa_{1-x}N$ layers have also been reported. High specific detectivity (D^*) of 1×10^{14} Jones (cm·$\sqrt{Hz}$/W) was calculated for the solar-blind p–i–n-based PD, similar to that of a PMT, but without the need of a high voltage supply. While undertaking the effort to improve $Al_xGa_{1-x}N$-based PDs, high PD response speeds up to to 1.7 ns (rise time) and 4.5 ns (fall time) p–i–n PDs were demonstrated by Albrecht *et al.* through the optimization of layer growth conditions[515]. In an earlier work, an $Al_xGa_{1-x}N$-based MSM PD with a 3-dB bandwidth of as high as 5.4 GHz was also demonstrated[516]. More recently, Muhtadi *et al.* reported an $Al_{0.64}Ga_{0.36}N/Al_{0.34}Ga_{0.66}N$ MQW-based PD with an RC-limited response speed of 2 ns[517], undoubtedly opening up a vast application opportunity of solar-blind $Al_xGa_{1-x}N$-based PDs for high speed operation and monolithic integration.

Other than planar structures, $Al_xGa_{1-x}N$-based PDs constructed using lower-dimensional structures, such as nanowires and nanorods, have also received significant attention[518]. In 2017, Kang *et al.* reported on a two-step growth process for single-crystalline silicon-doped $Al_{0.45}Ga_{0.55}N$ nanorods as a solar-blind PD[519]. The vertically-aligned and compositionally uniform nanorod structure displayed high responsivity of up to about 115 mA/W and high sensitivity of approximately 64% in the UV-C region[519]. Later, the same group demonstrated improved photoresponsivity of up to 0.72 A/W, fabricated using n-type $Al_{0.45}Ga_{0.55}N$ nanowires with flower-like morphology, also called as nanoflowers[508]. Figs. 19(c) and 19(d) show improved photocurrent by close to one order of magnitude and high responsivity of up 0.72 A/W in $Al_{0.45}Ga_{0.55}N$ nanoflower-structured PD, compared to that of nanowire-structured PD (0.13 A/W) and nanorods (0.09 A/W). The improved performance of nanostructured PDs was largely attributed to improved photon absorption due to high aspect ratios and compact density distribution[138]. These works paved the way for high performance low-dimen-

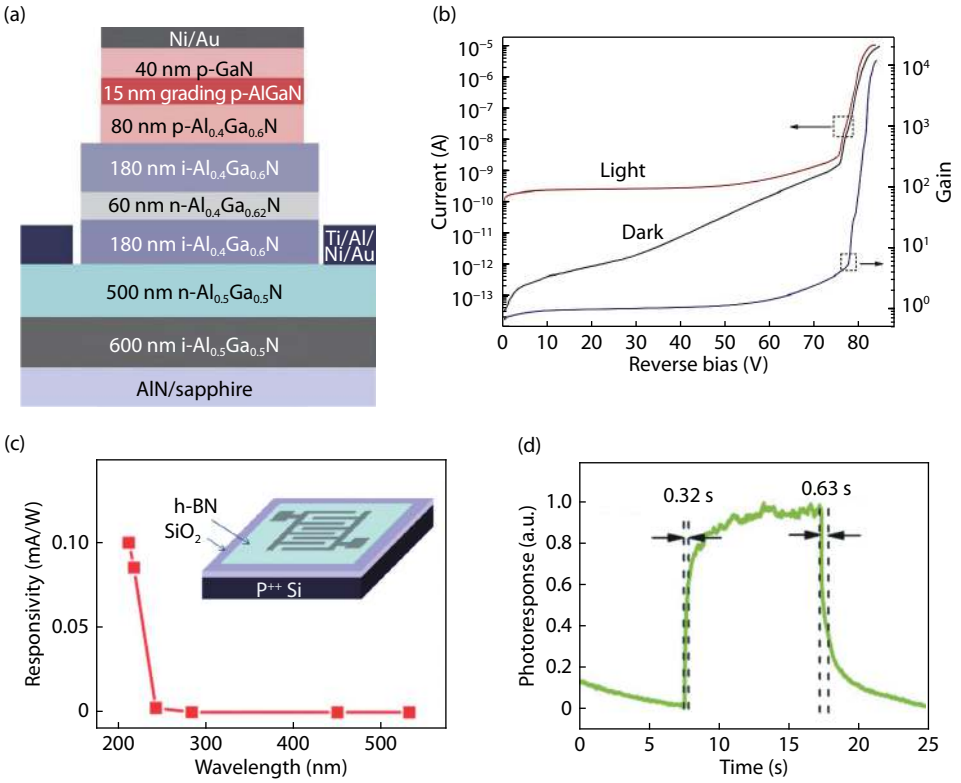

Fig. 20. (Color online) (a) Device structure of $Al_{0.40}Ga_{0.60}N$-based p–i–n–i–n separate absorption and multiplication (SAM) APD. (b) *I*–*V* curves and multiplication gain achieved using $Al_{0.40}Ga_{0.60}N$-based APD. (Reprinted with permission from Ref. [522]. ©2014, IEEE). (c) Responsivity spectrum of an h-BN-based MSM PD with peak responsivity of 0.1 mA/W at 212 nm and a clear cut-off wavelength at around 225 nm. Inset shows the schematic illustrations of the device structure, where h-BN layers were transferred onto SiO_2/Si substrate with interdigitated electrode fabricated on the top. (d) Photoresponse spectrum of an h-BN-based MSM PD showing a slow rise time of 0.32 s and a fall time of 0.63 s. Reprinted with permission from Ref. [550]. ©2018, Royal Society of Chemistry.

sional $Al_xGa_{1-x}N$-based PDs in various applications[520]. Furthermore, group III–nitride-based avalanche photodetectors (APD), which show promise in providing higher photocurrent gains combined with high speeds and low operating voltages, are also of contemporary interest in the community[521–529]. Moreover, the use of Geiger-mode operation in group III–nitride-based APDs has also received significant attention for its potential employment in high sensitivity single-photon counting for various applications, such as quantum computing and astrophysics[530, 531]. Compared to UV-enhanced silicon-based APDs, $Al_xGa_{1-x}N$-based APDs promise high wavelength tunability and selectivity. Low leakage currents and high avalanche gains (5×10^5) in an $Al_{0.05}Ga_{0.95}N$ APDs grown on free-standing GaN substrates were demonstrated by Kim *et al.* in 2015,[532] highlighting a significant improvement in APD performance, compared to other APD structures grown on sapphire templates. Later in 2016, Wu *et al.* reported a true solar-blind $Al_{0.40}Ga_{0.60}N$-based APD structure with zero-bias EQE of up to 52.7% with an avalanche gain of higher than 2×10^4 at a relatively high voltage bias of −140 V[533]. More recently, Hahn *et al.* demonstrated a relatively low dark current of 1 pA at up to 60 V reverse voltages in an $Al_{0.69}Ga_{0.31}N$-based APD grown on sapphire substrate, with multiplication gain of around 5500 at 84 V reverse bias[534]. Another special type of $Al_xGa_{1-x}N$-based APDs, based on a p–i–n–i–n separate absorption and multiplication (SAM) structure, has also been studied for higher gain and lower avalanche breakdown voltage, compared with their conventional counterpart[522, 535]. Fig. 20(a) shows a back-illuminated p–i–n–i–n SAM structure while Fig. 20(b) shows a demonstration of its capability to achieve record high gain of up to 1.2×10^4 at a reverse bias of 84 V.

However, to tailor PDs for the DUV wavelength regime of operation, high quality and crack-free high-aluminum-content layers are pivotal. Up until now, no solution has been found to address high defect densities associated with the incorporation of $Al_xGa_{1-x}N$ layers with high aluminum contents. Walker *et al.* was one of the earliest to demonstrate $Al_xGa_{1-x}N$-based PDs operating in DUV wavelengths with a responsivity of 0.11 A/W at 232 nm (5 V reverse voltage) and an IQE of 90%[536]. In their device structure, high-aluminum-content $Al_xGa_{1-x}N$ layers of up to x = 70% were successfully grown using low-pressure chemical vapor deposition (LPCVD) on sapphire substrates. Subsequently, in 2007, Gökkavas *et al.* demonstrated $Al_{0.75}Ga_{0.25}N$-based with relatively high responsivity of up to 0.53 A/W at 222 nm[537]. The high responsivity obtained in this work can be attributed to the high-quality $Al_{0.75}Ga_{0.25}N$ layer, demonstrating a low dark current of less than 100 pA at very high bias voltages of up to 350 V. Alternative nitride-based materials, such as AlN and BN, have also been widely discussed[477, 538–542]. AlN-based photodetectors received significant attention in the early 2000s because of their high bandgap energies (around 6.1 eV) and high SNRs with the suppression of visible background for DUV detection. The demonstration of AlN-based MSM PD for operation below 230 nm was reported by Li *et al.*[477]. A sharp cut-

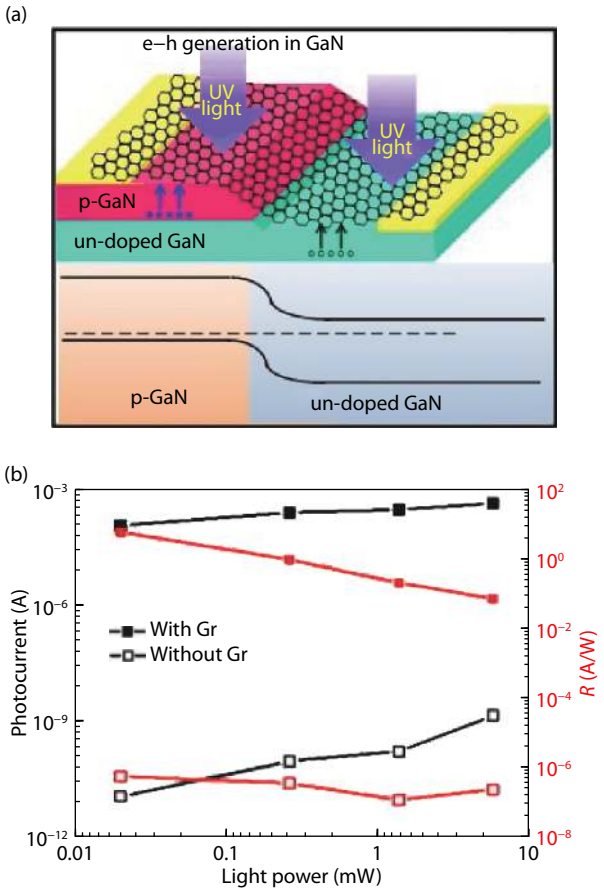

Fig. 21. (Color online) (a) Schematic of the device structure and bandgap energy diagram of hybrid graphene/GaN UV PD. (Reprinted with permission from Ref. [552]. ©2018, The Optical Society). (b) Photocurrent and responsivity curves of a hybrid graphene/GaN UV-A PD at 10 V reverse bias (with and without graphene). (Reprinted with permission from Ref. [553]. ©2018, AIP Publishing).

off wavelength was observed at 207 nm with peak responsivity of 0.4 A/W (at 100 V voltage bias) at 200 nm, with a rejection ratio of four orders of magnitude. The insertion of superlattice structures after the AlN nucleation layer have also been introduced by Nikishin *et al.* to reduce the inversion domains (IDs) in AlN-based PDs[543]. The fabricated large-area MSM PD exhibited a low dark current of 50 fA up until 30 V voltage bias with the insertion of AlN/GaN short-period superlattices (SPSLs), with a peak responsivity of 0.08 A/W at 202 nm. Following these discoveries, large area (about 3.1 mm^2) DUV PDs based on AlN films were demonstrated by Barkad *et al.* with titanium nitride (TiN) as a Schottky contact[544]. The cut-off wavelength was reported to be around 203 nm, the shortest ever cut-off wavelength reported in AlN-based PDs, with a rejection ratio of up to three orders of magnitude. Other than the above, the first surface acoustic wave (SAW)-based DUV sensor based on AlN films for photodetection below 200 nm has also been reported[545]. In recent years, BN with similar bandgap energy (around 6 eV) as AlN have also received increasing attention for DUV applications. In 2018, Soltani *et al.* demonstrated DUV PD with cut-off wavelength below 200 nm using cubic BN (c-BN)[546]. The MSM-based PD demonstrated a very short cut-off wavelength at 193 nm because of the wide bandgap of c-BN (about 6.4 eV), while the peak responsivity appears at 32 mA/W at 180 nm with 35 V voltage bias. Although the achieved responsivity is still considered relatively low, the cut-off wavelength was the shortest at that time, and a high rejection ratio of up to four orders of magnitude was also recorded. Later in 2012, Li *et al.* explored h-BN epitaxial layers as UV photodetectors with sharp cut-off wavelengths at around 230 nm with high absorption coefficients (approximately 7×10^5 cm^{-1}) than that of AlN (around 2×10^5 cm^{-1})[547]. In addition to their sufficient performance as thermal interface materials[548], optically transparent (down to 210 nm) BN nanosheets (BNNSs) have also been examined for UV detection below 300 nm[549]. This study showed that the BNNSs-based DUV PDs were blind to photons with energies of less than 4 eV, with a PD output power of around 2 μW. However, the output electrical power to the input optical power ratio was about 1%. Until recently, DUV PDs based on 3 nm-thin h-BN layers were demonstrated by Liu *et al.*[550]. The devices exhibited a low responsivity of 0.1 mA/W at 212 nm, as shown in Fig. 20(c), but also exhibited a rejection ratio of over three orders of magnitudes between 212 and 284 nm. The low responsivity obtained was ascribed to the limited thickness and non-uniformity of the h-BN layers. In addition, as shown in Fig. 20(d), relatively slow response times of 0.32 s (rise time) and 0.63 s (fall time) were observed, thus limiting their relevance in high speed detection applications. Most recently, we demonstrated a novel heterogeneous integration of group III–oxides and silicon to fabricate solar-blind DUV $(Al_{0.28}Ga_{0.72})_2O_3$ Schottky MSM and metal–insulator–metal (MIM) photodetectors. Apart from achieving a high peak responsivity of 1.17 A/W at 230 nm, this is also the first demonstration of DUV Ga_2O_3-based photodetector grown on a silicon substrate, paving the way for potential monolithic integration of future DUV oxide-based photodetectors on the matured silicon platform[551].

As discussed earlier, further improvements in the performance of group III–nitride-based PDs were largely inhibited by the low crystal quality and low conductivity characteristics originating from the growth of PD structure materials. To alleviate these issues, hybridization of GaN-based PDs with 2D materials, such as graphene, have been proposed. Phototransistors based on graphene/GaN structures with relatively high responsivity of 0.36 A/W at 325 nm were reported by Tian *et al.* and shown in Fig. 21(a). Their reported device characteristic values were significantly higher than those realized without the integration of graphene layers (up to 700-fold improvement); the high achieved gain can be attributed to high carrier mobility effects exhibited in graphene, which allow for multiple carrier transport to generate high photocurrent densities[552]. Without the graphene layer, it can be expected that generated carriers would be trapped in the lower-mobility GaN layer, limiting the achievable photocurrents and gains in PD devices. Similar work was later published by Tian *et al.* They demonstrated a significantly enhanced responsivity of up to 5.83 A/W with illumination at 325 nm and an EQE of up to 2200%, which they accredited to multiple carrier circulation and long carrier lifetimes in the graphene layer using a similar hybrid phototransistor structure[553]. However, it was also emphasized that responsivity considerably decreased with increasing power of incident light, as shown in Fig. 21(b), because of dampening of the net built-in electric fields by opposite electric fields formed by accumulated pho-

togenerated carriers. Nevertheless, both reports provide insight into improving the performance of UV phototransistors without stringent requirements on the crystal quality of light-absorbing layers. Notably, a similar strategy was employed in DUV PD devices to improve photoconductive gains, with graphene layers achieving transparencies greater than 80% within the DUV regime[554]. The incorporation of BNNSs and 1D cellulose nanofibers has also been demonstrated as flexible solar-blind PDs by Lin *et al*. Although their demonstrated paper-based device exhibited a relatively low responsivity of 0.05 mA/W at 185 nm illumination, the device displayed near-zero responsivity between UV-B (300 nm) up to NIR (1000 nm) wavelengths, manifesting its true solar-blind detection capabilities[52]. Furthermore, taking advantage of the high thermal conductivity of h-BN (about 146 W/mK), the paper-based device was capable of functioning at high temperatures of up to 200 °C, which represents a significant step forward in reaching the goal of flexible and wearable electronic devices. Table 3 provides a summary of key performance characteristics of state-of-the-art group III–nitride-based and hybrid UV and DUV PDs.

4.3. Lasers

Poor current conduction has also prevented the achievement of electrically pumped QW lasers operating in the UV-B (280–315 nm) and UV-C (200–280 nm) bands[566–570]. Because they are still being extensively investigated in research laboratories around the globe, the development of DUV LDs is still in its infancy stage, as these researchers almost exclusively attempt to exploit the $Al_xGa_{1-x}N$ material system[571, 572]. To realize an LD, energy transfer into the gain medium of the laser from an external source to produce excited states in the atoms (referred to as the laser pumping process) is necessary. The laser pumping method can be classified into two categories:

1. Electrical pumping: LDs are naturally pumped using electric currents. Researchers have demonstrated electrically pumped lasers at relatively long emission wavelengths, such as 330 nm[573] and 342 nm[574], and also at 275 nm[575]. The former two operate within the UV-A region, while the latter emits a UV-C light suitable for germicidal applications. The challenges for realizing electrically injected DUV LDs using $Al_xGa_{1-x}N$ MQW structures include the high densities of dislocations in the lattice structure, large spontaneous and piezoelectric polarization fields, and poor p-type doping characteristics. These issues hinder improvement in the DUV LD EQE and the output power of electrically injected $Al_xGa_{1-x}N$ MQW-based DUV LDs. Some researchers have focused their attention on nanowire-based LDs because of the potentially high crystalline quality that they can achieve, the high LEEs, and the low strain-induced polarization exhibited in nanowire structures[576]. Random lasers based on nanowire arrays have been demonstrated at peak lasing wavelengths of 239 nm[577] and 262.1 nm[578]. However, their optical output powers are still considerably low, while peak emitting wavelengths are mostly unstable because the laser cavities are defined through random multiple scattering.

2. Optical pumping: Pumping LDs using an optical pumping source is an artificial way to operate a laser, although dye lasers are optically pumped[579–583]. DUV LDs emitting at the sub 250 nm regime have been demonstrated[584–586], but producing light using this method would require another optical power source with higher optical power outputs and shorter excitation wavelengths, rendering this mechanism impractical in real-life applications.

Given these hindrances, conventional optically pumped DUV LDs and electrically pumped random DUV LDs are impossible to practically exploit in vital applications, such in the study of geology and climate in outer space. An alternative way to drive an LD active material is by using an electron beam, through which electron–hole pairs are generated by the energy transfer of high-energy electrons emitted from an electron gun. One advantage of this approach is that the incorporation of p- and n-type doped layers is not necessary, avoiding the undesired optical absorption commonly associated with these layers. In 2015, Klein *et al*. demonstrated high-power green and blue electron-beam-pumped LDs, with a peak optical powers of 5.9 W (λ = 350 nm) and 3.3 W (λ = 462 nm) at moderate electron energies of 42 keV and 37 keV, respectively[587]. In 2010, Oto *et al*. achieved DUV emission from electron-beam-excited AlN-based QW optical source with a peak emission at 240 nm, peak optical power of 100 mW, and pumping power and current of 10 kV and 45 μA, respectively[588]. The success shown in these reports manifests a great potential of electron-beam-pumped LDs in achieving high power and short wavelength DUV laser devices.

5. Substrate technology and heterogeneous integration of new materials

To realize efficient optoelectronic devices for applications necessitating DUV light emission, high-crystalline-quality AlN templates are the key enablers of success in growing upper $Al_xGa_{1-x}N$ epitaxial layers. Various growth techniques were developed to either achieve efficient UV and DUV light emission or merely improve the crystalline quality of $Al_xGa_{1-x}N$ layers[589, 590].

5.1. High quality AlN templates

Kataoka, Funato, and Kawakami developed 3D $Al_{0.50}Ga_{0.50}N$ QWs on MOVPE-grown AlN templates for polychromatic DUV LEDs[591]. They attempted a maskless regrowth of AlN on a trench-patterned AlN template procedure to create the AlN multi-facets of (0001), {1$\bar{1}$01}, and vicinal (0001) with bunched steps[592]. Eventually, multi-faceted p–i–n structures, including three periods of $Al_xGa_{1-x}N/Al_yGa_{1-y}N$ active region, were grown on the AlN template, which led to different emission wavelengths as demonstrated in Fig. 22(a). Under DC injection current at room temperature, two polychromatic emission bands at 250 and 275 nm were demonstrated, with a tendency similar to those observed by Funato *et al*. for 3D $In_xGa_{1-x}N$ polychromatic emitters[593]. Without any patterning or further synthesis of high-level-features AlN template, Kaneda *et al*. used the continuous high-temperature (CHT) growth method before growing $Al_xGa_{1-x}N$-based DUV LEDs[594–597]. With increased miscut angles of 0.2°, 0.3°, and 10 for sapphire substrate, the MOVPE AlN template exhibited lower TDDs and denser macrosteps as illustrated in Fig. 22(b). The flip-chip bonded DUV LEDs grown on a miscut angle of 1.0° demonstrated 20% higher output power, compared with the devices on 0.3° miscut. They also experimentally proved that the enhanced IQE performance was caused

Table 3. Performance comparison of select group III–nitride-based and hybrid UV and DUV PDs at room temperature (* Indicates an EQE value we calculated using Eq. (14)).

Device structure	Material system	Bias (V)	Peak responsivity (A/W)	EQE	Rise/Fall time (s)	Year	Ref.
MSM	$(Al_{0.28}Ga_{0.72})_2O_3$	2.5	1.17 (230 nm)	631%	–	2019	[551]
MSM	β-Ga_2O_3/TiN	15	277.08 (250 nm)	1.37×10^5%	–	2019	[555]
MSM	β-Ga_2O_3	10	8.41 (254 nm)	4.11×10^3%*	18 s/1.6 s	2019	[556]
MSM	β-Ga_2O_3	20	150 (254 nm)	7.40×10^4%	1.8 s/0.3 s	2018	[557]
MSM	$Al_{0.50}Ga_{0.50}N$	20	0.094 (270 nm)	43.2%*	<20 ms/ <20 ms	2018	[503]
MSM (flexible)	h-BN	10	0.00005 (185 nm)	0.03%*	0.267 s/0.393 s	2018	[52]
MSM	h-BN	20	0.0001 (212 nm)	0.06%*	0.32 s/0.63 s	2018	[550]
MSM	$Al_{0.50}Ga_{0.50}N$	10	5 (264 nm)	2.35×10^3%*	0.52 s/44 s	2017	[558]
MSM	$Al_{0.50}Ga_{0.50}N$	5	10^6 (250 nm)	4.96×10^8%*	0.2 s/1000 s	2017	[507]
MSM (SiO_2-passivated)	$Al_{0.25}Ga_{0.75}N$/GaN	10	0.27 (365 nm)	91.78%*	–	2015	[504]
MSM	$Al_{0.25}Ga_{0.75}N$	5	<0.01 (310 nm)	<4% *	–	2013	[502]
MSM	$Al_{0.42}Ga_{0.60}N$	20	0.045 (270 nm)	21.5%	–	2013	[494]
			0.085 (270 nm)	39%	–		
MSM	TiN/AlN	100	0.002 (200 nm)	1.24%*	–	2010	[544]
MSM	AlN	10	0.08 (202 nm)	49.14%*	–	2009	[543]
MSM	c-BN	35	0.032 (180 nm)	22.06%*	–	2008	[546]
MSM	$Al_{0.75}Ga_{0.25}N$	50	0.53 (222 nm)	>250%	–	2007	[537]
p–i–n	$Al_{0.46}Ga_{0.54}N$	0	0.15 (271 nm)	68.8%	6.5 ns/0.95 μs	2018	[514]
p–i–n	$Al_{0.34}Ga_{0.66}N$	0.5	0.1 (250 nm)	50%	0.4 μs/0.4 μs	2017	[517]
p–i–n	$Al_xGa_{1-x}N$	0	0.21 (360 nm)	70%	1.7 ns/4.5 ns	2014	[515]
p–i–n	$Al_{0.40}Ga_{0.60}N$	5	0.192 (275 nm)	89%	–	2013	[511]
p–i–n	$Al_{0.40}Ga_{0.60}N$	5	0.129 (279 nm)	57%	–	2013	[509]
p–i–i	$Al_{0.55}Ga_{0.45}N$	5	0.075 (254 nm)	37%	–	2012	[510]
p–i–n	$Al_{0.70}Ga_{0.30}N$	5	0.11 (232 nm)	58.83%*	–	2000	[536]
p–i–n–i–n	$Al_{0.40}Ga_{0.60}N$	15	0.15 (280 nm)	50%	–	2014	[522]
p–i–n APD	$Al_{0.40}Ga_{0.60}N$	0	0.114 (278 nm)	52.7%	–	2016	[533]
p–i–n APD	$Al_{0.05}Ga_{0.95}N$	0	0.043 (354 nm)	16%	–	2015	[532]
MIS	$Al_{0.45}Ga_{0.55}N$	3	0.154 (270 nm)	70.6%	1.4 ns/55 μs	2018	[513]
MIM	$(Al_{0.28}Ga_{0.72})_2O_3$	2.5	0.4 (230 nm)	218%	–	2019	[551]
p–n	$PtSe_2$/GaN	0	0.193 (265 nm)	90.36%*	0.172 μs/284 μs	2019	[559]
p–n	MoS_2/GaN	0	0.187 (265 nm)	87.55%*	46 μs/114 μs	2018	[560]
Heterojunction	graphene/Ga_2O_3 nanowires	5	0.185 (258 nm)	88.96%*	9 ms/8 ms	2018	[561]
Heterojunction	graphene/β-Ga_2O_3	6	12.8 (254 nm)	6.68×10^3%	1.5 ms/2 ms	2018	[562]
Heterojunction	graphene/h-BN/GaN	1	1915 (245 nm)	9.69×10^5%*	8 s/6 s	2016	[563]
Schottky	graphene/β-Ga_2O_3/graphene	10	9.66 (254 nm)	4.72×10^3%*	0.96 s/0.81 s	2017	[564]
Schottky	graphene/$Al_{0.25}Ga_{0.75}N$/GaN	2	0.56 (300 nm)	231.60%*	–	2016	[565]
Phototransistor	graphene/GaN	10	0.361 (325 nm)	138%	3.2 ms/1.2 ms	2018	[552]
Phototransistor	graphene/GaN	10	5.83 (325 nm)	$>2.20 \times 10^3$%	2.7 ms/4.6 ms	2018	[553]
Nanorods	$Al_{0.45}Ga_{0.55}N$	3	0.115 (250–276 nm)	53.84%*	–	2017	[519]
Nanowires (Schottky)	GaN	1	25 (357 nm)	8.69×10^3%*	–	2013	[518]
Nanoflowers (MSM)	$Al_{0.45}Ga_{0.55}N$	2	0.72 (265 nm)	340%	–	2018	[508]

by the reduction in nonradiative recombination channels at the MQWs and the compositional modulations in the MQWs by virtue of the macrosteps of the AlN template[598, 599]. As an alternative to MOVPE grown AlN templates, Susilo *et al.* and Miyake *et al.* investigated sputtered AlN templates with high temperature annealing (HTA)[600, 434]. Sputtered AlN provide an avenue to achieve cost-efficient AlN templates with low TDDs[432, 601–611]. In addition, HTA can provide beneficial effects on the grain of buffer layers at the AlN layer/substrate interfaces by eliminating tilt components between buffer layer grains, achieving TDDs down to 4.7×10^8 cm^{-2} for 2.3 μm-thick MOVPE-grown AlN layers[433]. In addition to their lower production costs and reduced substrate curvature, Susilo *et al.* showed that sputtered thin HTA AlN (⩽750 nm) template exhibited lower TDDs (7.2×10^8 cm^{-2}) as compared to epitaxially laterally overgrown (ELO) AlN/sapphire using MOVPE (1.1×10^9 cm^{-2}). Their DUV LED devices (fabricated on the sputtered AlN templates) demonstrated DUV emission at around 268 nm, with output powers in the range of 0.65–0.72 mW at 20 mA, which is comparable to DUV LEDs fabricated on MOVPE-grown AlN templates[600]. Several MOVPE complex growth approaches were attempted, including lateral overgrowth of nitrogen-polar AlN domains with aluminum-polar AlN[612] and high-V/III-ratio-induced roughening[613]. Typical AlN layer TDD values were around 1×10^9 cm^{-2}, which are desirable but not adequate for the realization of high-efficiency DUV LEDs[409].

Chang *et al.* demonstrated the growth of high-quality AlN templates on NPSSs via graphene-assisted quasi-van der Waals epitaxy[614–617]. This process allowed for rapid film coales-

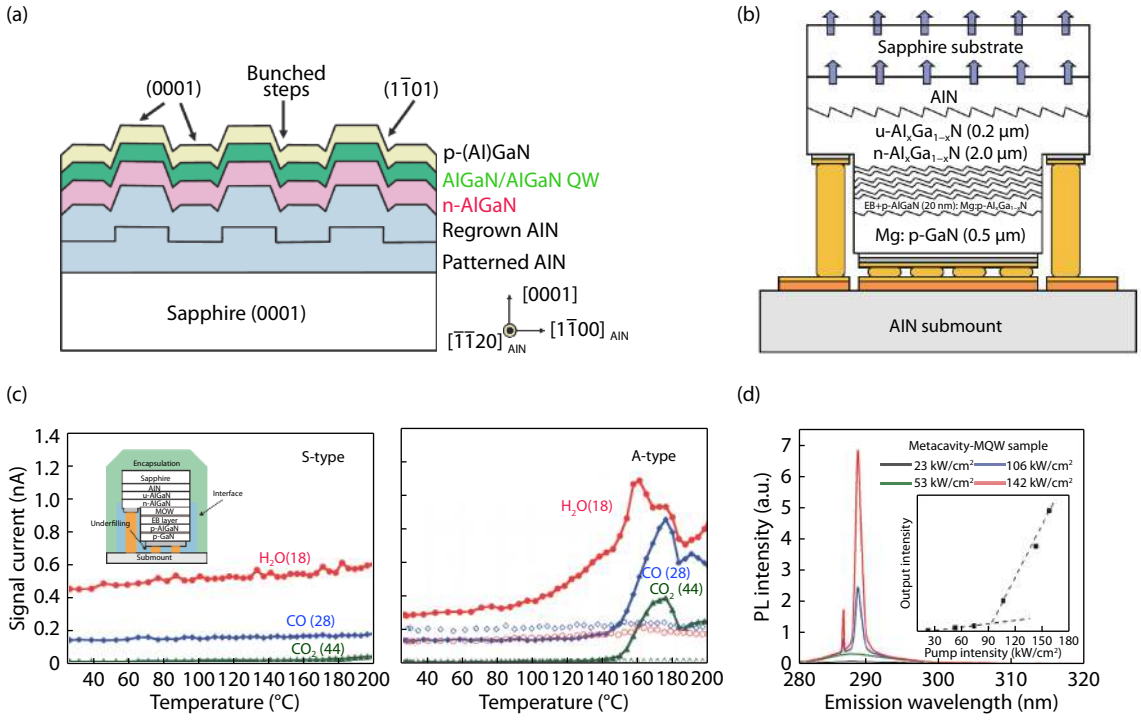

Fig. 22. (Color online) (a) Schematic illustration of an $Al_{0.50}Ga_{0.50}N$-based polychromatic UV LED structure on patterned AlN template. Reprinted with permission from Ref. [591]. ©2017, The Japan Society of Applied Physics. (b) Schematic illustration of a flip-chip mounted $Al_xGa_{1-x}N$-based UV LED with uneven MQWs. Reprinted with permission from Ref. [594]. ©2017, The Japan Society of Applied Physics. (c) Temperature-programmed desorption mass spectroscopy analysis for S- (left) and A-type (right) resin samples. For S-type sample, no decomposition observed. However, A-type sample showed CO, CO_2, and H_2O peaks after DUV irradiation. Inset shows the schematics of DUV LED with underfilling and encapsulation. Reprinted with permission from Ref. [410]. ©2015, The Japan Society of Applied Physics. (d) PL versus pump power of metacavity-MQWs. Narrow lasing peaks were shown from a broad emission spectrum. Inset shows PL peak intensity versus pump power indicating the lasing threshold. Reprinted with permission from Ref. [630]. ©2018, John Wiley & Sons.

cence, reducing growth times. Because of the presence of graphene, AlN films tend to be 2D laterally expanded on the NPSS, resulting in reduction of TDD (from 5.5×10^9 cm^{-2} to 1.5×10^9 cm^{-2} on the surface for layer thickness of 1.5 μm) as well as strain release in the AlN epitaxial layer, which were attributed to air voids above the nanopattern that were formed during the epitaxial growth process. The 2D growth nature of AlN in this case caused the TDs near the air voids to bend and ultimately annihilate at the end of the void. EL measurements of the fabricated DUV LEDs utilizing the graphene interlayer have shown considerable improvement in emission characteristics at 280 nm.

5.2. Hybrid integration on Ga_2O_3

Gallium oxide and its ternary alloys ($(In_xAl_yGa_z)_2O_3$, $x + y + z = 1$) are wide-bandgap oxides of post-transitional metals with ionic bonds. With superior breakdown fields of around 8 MV/cm compared with SiC (3 MV/cm) and GaN (3.8 MV/cm), their intrinsic band gap spans from 4.9 to 5.3 eV; there are five known polytypes of Ga_2O_3, α, β, γ, δ, and ε[618]. Among these, β-Ga_2O_3 is the most stable structure with a superior melting point of up to 1820 °C; it became available as a wafer substrate by using conventional melt growth techniques. Despite its large bandgap ranging from 4.7 to 5.0 eV, its electrical properties can be tuned from an insulator to an n-type semiconductor with carrier concentration of up to 10^{19} cm^{-3} for DUV device applications[619, 620]. In contrast, α-Ga_2O_3 has not yet been studied as a metastable phase of Ga_2O_3. With a highest energy bandgap of around 5.3 eV, its rhombohedral corundum structure allows for its utilization on conventional sapphire substrates as opposed to using it as a wafer. In addition, alloys of α-Al_2O_3, α-Ga_2O_3, and α-In_2O_3 can make multinary oxide compounds from each other. Eventually, they can make unique physical properties with other corundum systems of transition metal oxides (α-M_2O_2; M = Fe, Cr, V, Ti, Rh, and Ir)[281].

High n-type conductivity and transparency characteristics reveal that Ga_2O_3 is an ideal candidate for the realization of DUV devices as a transparent conducting oxide (TCO) substrate. Even though Ga_2O_3 does not have a hexagonal structure, it is relatively easy to induce a hexagonal atomic arrangement for optoelectronic device applications. In 2015, epitaxial growth of planar GaN layer on (100) a-plane β-Ga_2O_3 was first demonstrated[621]. Low-temperature GaN buffer layer was first introduced, and a 1 μm-thick GaN layer was subsequently grown at 1070 °C by MOVPE. From the X-ray diffraction measurement, θ–2θ scan confirmed a wurtzite GaN layer with c-plane orientation, and it showed 1200 arcsec full width at half maximum (FWHM) rocking curve. Room temperature photoluminescence measurements showed an emission peak wavelength at around 362.6 nm, and eventually, a blue LED device was successfully fabricated. In 2006 and 2007, GaN layers grown on β-Ga_2O_3 were also demonstrated by ammonia- and RF-MBE, respectively[622, 623]. In MBE epitaxial growth, nitridation was a crucial factor for planar GaN layer growth at the interface with β-Ga_2O_3 substrate. In ammonia-MBE, nitridation was processed under NH_3 condition inside

the growth chamber to reconstruct the surface from a twofold symmetry *a*-plane β-Ga_2O_3 to a sixfold symmetry of *c*-plane GaN. Effective nitridation step helped to obtain a transparent and mirror-like GaN surface layer on Ga_2O_3; however, GaN has a rough surface and tends to peel off from the substrate when the nitridation step is skipped[622]. The surface of β-Ga_2O_3 was also successfully controlled by nitridation in RF-MBE[623]. At the interface, GaN phase was transformed from cubic to wurtzite by increasing the nitridation time. This thin GaN layer served as the basis for growth of subsequent epitaxial GaN layers on the β-Ga_2O_3 substrate. In 2012, another research group further investigated *c*-plane GaN layers on (100) *a*-plane β-Ga_2O_3 that could easily be peeled off from the substrate[624]. Initially NH_3-treated 150 μm-thick GaN layers showed limited adhesion at their interfaces. As a result, the self-separation of GaN layer was achieved at room temperature, directly after the hydride vapor phase epitaxy (HVPE) growth process.

As part of a GaN epitaxial layer growth study on β-Ga_2O_3 substrates, an $Al_xGa_{1-x}N$ layer was demonstrated by MOVPE, and its crystalline quality was compared with that of grown on sapphire. The $Al_{0.08}Ga_{0.92}N$ and GaN growth processes were carried out on low-temperature buffer layers[625]. An optimized facet-controlled method and thermal annealing process resulted in high-quality GaN and $Al_{0.08}Ga_{0.92}N$ layers on β-Ga_2O_3 substrates with enhanced morphology, photoluminescence intensity, and reduced FWHM of the X-ray diffraction rocking curve. Other than the (100) plane, the growth of GaN/$Al_{0.20}Ga_{0.80}N$ MQWs on ($\bar{2}$01)-oriented β-Ga_2O_3 was also investigated by Ajia *et al.*[626]. While GaN layer growth on (100) β-Ga_2O_3 resulted in an uncontrollably peeled off film from the substrate, Ajia *et al.* demonstrated that GaN/$Al_{0.20}Ga_{0.80}N$ growth on ($\bar{2}$01)-oriented β-Ga_2O_3 can provide a stable layer for the more operationally stable vertical device applications. With a 2 nm-thick low-temperature AlN buffer layer, a 100 nm-thick n-$Al_{0.75}Ga_{0.25}N$ layer was grown at 1020 °C, followed by a 900 nm thick n-$Al_{0.30}Ga_{0.70}N$ layer at 1120 °C. Subsequently, 3× GaN/$Al_{0.20}Ga_{0.80}N$ MQWs were grown for their study. As compared to films grown on sapphire substrates, the GaN/$Al_{0.20}Ga_{0.80}N$ MQWs on the ($\bar{2}$01)-oriented β-Ga_2O_3 showed higher structural and optical crystalline quality as well as lower density of nonradiative recombination centers. These results hold promise of unleashing the potential of UV transparent and conductive Ga_2O_3 substrates as a suitable alternative to group III–nitride-based substrates for the realization of DUV device applications.

5.3. Polymeric materials as key enablers for DUV light-emitting device mass production

Polymeric materials, such as optically isotropic and stable amorphous fluorine resin[627, 628] and graphene oxide (GO)-based fluoropolymer composites[629], may constitute a suitable substitute to other materials for the mass-production and packaging of $Al_xGa_{1-x}N$-based UV and DUV LEDs because of their decomposition characteristics below 330 nm[410, 457, 627, 628]. DUV LED dies are generally flip-chip bonded on submounts with gold bumps, and polymer-based materials can be used between the submount and dies as underfilling materials, as well as for the rest of entire surfaces (as an encapsulation). Yamada *et al.* revealed that instead of conventional resins, C-F-based polymers, so called S-type amorphous fluorine resins (terminated with a trifluoromethyl), are ideal candidates for the underfilling and encapsulating materials for the DUV LEDs[410]. Fig. 22(c) shows the temperature-programmed desorption mass spectroscopy analysis for S- and A-type resin with an inset indicating the schematics of flip-chip LEDs with underfilling and encapsulation. From this experiment, S-type resin tests showed no peaks after 261 nm light irradiation. However, A-type resin showed CO, CO_2, and H_2O peaks after DUV irradiation, which means decomposition of materials. With the optically isotropic characteristics of S-type resin for encapsulation, it showed no degradation over 3000 h of operation time.

5.4. Nanolasers realized via nanoscale plasmonic effects

Increasing demand of miniature-sized LD are of importance for the optical communications and data storage industries. One of the possible approaches for the realization of nanoscale lasers is using surface plasmon polaritons, which contain strong localized fields at the dielectric/metal interfaces. Recently, Shen *et al.* demonstrated DUV lasers with hyperbolic metamaterial (HMM) including multiple stacks of dielectric (20 nm of MgF_2)–metal (20 nm of aluminum) interfaces[630, 631]. Those specially designed hyperbolic metacavity arrays helped to achieve a high-quality photonic density of state (PDOS), and eventually all excited plasmon oscillations coupled in one lasing mode. Focused ion beam (FIB)-fabricated 200 nm^2 hyperbolic metacavity arrays were formed on MOVPE-grown high aluminum-content $Al_xGa_{1-x}N$ MQW active regions, and the top of the structures were capped with annealed aluminum films as reflectors. Using a 266 nm pulsed laser as an exciting source, plasmonic nanolaser was demonstrated at lasing peak of 289 nm with narrow linewidth of 0.8 nm as depicted in Fig. 22(d). The lasing threshold is shown in the inset of Fig. 22(d).

5.5. Integration of 2D MX_2/group III–nitride interfaces for the optoelectronic applications

In addition to UV light-emitting devices, researchers have also focused their efforts on advancing the integration of new materials for the realization of DUV photodetection. As a new approach for this application, the interesting characteristics exhibited at the interfaces of 2D TMDs and 3D group III–nitride semiconductors have recently emerged as the central theme of various studies[632–636]. The fabrication of 2D platinum diselenide ($PtSe_2$)/GaN heterojunctions for self-powered DUV photodetectors has also been reported[559]. Group III–nitride semiconductor materials and 2D TMDs can be bonded through the weak out-of-plane van der Waals interactions in the absence of surface dangling bonds on their surfaces[637], providing an easy path for the integration of MX_2/group III–nitride interfaces for the optoelectronic applications, where M = a transition metal (Mo, W, Nb, Ta, Ti, Re) and X = S, Se, Te[638, 639]. Specifically, the direct bandgap[640–642] 2D layered molybdenum disulfide (MoS_2) is the most promising candidate for this purpose and widely explored for PD applications[560, 638, 643–649]. With a relatively small lattice mismatch of 0.8% between MoS_2 and GaN layer, free-dangling bond surface of MoS_2 provides excellent heterojunctions[637]. Zhuo *et al.* investigated p–n MoS_2/GaN heterojunctions as self-powered PDs and developed a detection device for 265 nm

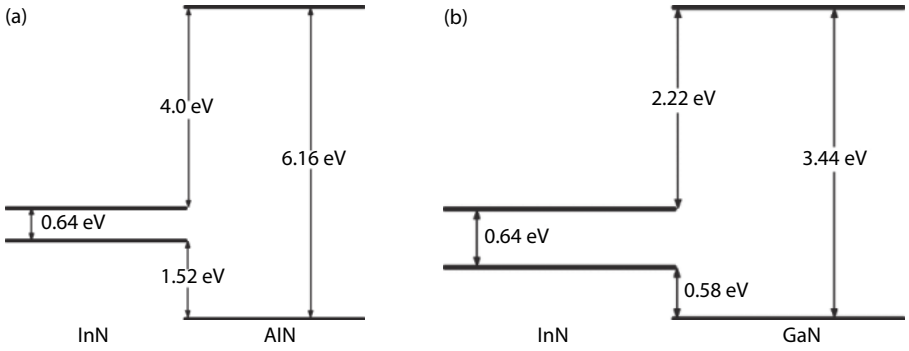

Fig. 23. Schematic representations of the band alignment at (a) InN/AlN and (b) InN/GaN interfaces acquired using HRXPS studies. Reprinted with permission from Refs. [659, 658], respectively. ©2007, AIP Publishing and ©2008, American Physical Society.

DUV light operating at zero bias voltage. The naturally formed band bending at the MoS_2/GaN interface results in the alignment of the Fermi levels of MoS_2 and GaN[650], inducing a built-in electric field that enables the device operation at zero bias voltage. Moreover, the strong interaction of the MoS_2 layer with incident light manifested excellent photoresponsivity to DUV light, with demonstrated high responsivity of 187 mA/W, high specific detectivity of 2.34×10^{13} Jones, and high ON/OFF current ratio of over 10^5[560].

6. Electrical carrier injection and band alignment

In this section, the band offsets of heterojunctions and their effects on charge carrier injection associated with the electrical transport properties are reviewed. We also review the doping and injection efficiencies of charge carriers. We emphasize the role of band-offset parameters as important parameters to understand the carrier injection efficiency and confinement effect of devices employing heterointerfaces. We further discuss the state of current injection efficiency in $Al_xGa_{1-x}N$-based UV LEDs.

6.1. Band alignment

The state and band parameters at semiconductor heterointerfaces are essential to the effective design of active regions in contemporary electronic and optoelectronic devices[331, 635, 651]. Band discontinuities present at heterojunctions, formed by adjoining two different semiconductor materials, have unequal bandgap energies that act as potential barriers, which play an important role in controlling the charge carrier transport properties[652]. The feasibility of charge carrier injection across such heterointerfaces relies on the interface quality and the band-offset parameters (i.e., CBOs and valence band offsets (VBOs))[653, 654]. Based on these parameters, heterostructures are classified based on three alignment types: straddling gap (referred to as type I), staggered gap (type II), and broken gap (type III) junctions[655]. In general, type I band alignments with high refractive index contrasts are the most favorable for electron and optical mode confinement, thereby facilitating the carrier recombination process in the active regions of $Al_xGa_{1-x}N$-based optoelectronic devices. The other two alignment types are necessary to realize other electronic devices, such as hot electron transistors, provided they exhibit reasonably low CBOs, which allows for improved tunneling probabilities and lower turn-on voltages[656]. Researchers have extensively employed X-ray photoelectron spectroscopy (XPS) to determine band offset parameters and interface alignment types formed by group III–nitrides using their bandgap energy values. Several studies can also be found on the band offset parameters of dissimilar heterojunctions formed between compound III–nitrides and other families of semiconductor materials, such as oxides and 2D materials[635, 657]. For instance, King *et al.* determined the band alignment type for InN/AlN and InN/GaN heterojunctions to be type I heterointerfaces using high-resolution XPS (HRXPS) measurements and the bandgap properties of the constituent materials[658, 659]. The corresponding band alignment schematic is shown in Fig. 23. Table 4 summarizes a thorough literature survey of band offset parameters for compound III–nitrides-based and hybrid heterostructures. It is noteworthy that irrespective of the polarity and crystal structure, all group III–nitride semiconductors exhibit type I heterojunctions, which satisfies the fundamental requirement to design optoelectronic devices. However, although the nature of type I heterojunctions at wide bandgap compound III–nitrides interfaces facilitates carrier and optical mode confinement, there are other bottleneck issues, such as line defects, structural cracking, and low p-type doping efficiencies, hindering the overall device efficiencies.

6.2. Doping and injection efficiency of charge carriers

From the ABC model, the IQE is directly proportional to η_{inj}, where η_{inj} is influenced by the efficiency of electron and hole injection[679, 680]. Considering the effective masses of charge carriers ($m_{e,h}$) in group III–nitride materials, it is evident that electrons are more mobile in the crystal lattice than holes[681–683]. The traditional approach of impurity-induced doping of III–nitrides suffers from the large acceptor activation energy of magnesium, thereby resulting in low p-type doping efficiency in $Al_xGa_{1-x}N$. Hence, electrons leak into the p-type $Al_xGa_{1-x}N$ layers of the optoelectronic devices, causing reduced IQE[162, 684, 685]. Strain-induced piezoelectric fields, along with spontaneous polarization fields, can have values in the order of several MV/cm, which lead to separation of electron and hole wavefunctions. Consequently, increased carrier separation results in the prevailing of QCSE, which has a detrimental effect on device efficiencies by reducing the radiative recombination[287, 686, 687]. Nonetheless, using the polarization-induced charges, researchers reported graded heterojunctions of $Al_xGa_{1-x}N$, which establishes a 3D slab of bound charges, either an n- or p-type conducting layer, depending on the direction of the aluminum concentration gradient and the polarity of the material[688]. Jena *et al.* showed the polarization-induced bulk electron doping in III–nitride semiconduct-

Table 4. Summary of group III–nitride, III–oxide, and hybrid material heterointerface properties.

Heterojunction structure	VBO (eV)	CBO (eV)	Heterojunction type	Measurement method	Ref.
Wurtzite GaN/AlN	0.7 ± 0.24	–	I	XPS	[660]
Cubic GaN/AlN	0.5 ± 0.1	1.4 ± 0.1	I	Theory (*ab initio*)	[661]
Cubic AlN/GaN (zincblende (001) SLs)	1.02	0.68	I	Theory (Quasiparticle)	[204]
Wurtzite InN/AlN	1.52 ± 0.17	4.0 ± 0.2	I	XPS	[659]
	1.81 ± 0.2	–	I	XPS	[660]
a-plane GaN/AlN	1.33 ± 0.16	–	I	XPS	[662]
a-plane AlN/GaN	0.73 ± 0.16	–	I	XPS	[662]
Semi-polar AlN/GaN	0.7 ± 0.2	2.1 ± 0.2	I	XPS	[663]
	0.58 ± 0.08	2.22 ± 0.1	I	HRXPS	[658]
	0.85	1.82	I	Internal photoemission	[664]
	1.04, 0.54	–	I	XPS	[665]
InN/GaN	1.05 ± 0.25	–	I	XPS	[660]
	0.5 ± 0.1	2.2 ± 0.1	I	XPS and PL	[666]
	1.07	1.68 ± 0.1	I	Photocurrent spectroscopy	[667]
	0.72 ± 0.28	–	–	XPS	[668]
$InAl_{0.83}N$/GaN	0.2 ± 0.2	1	I	XPS	[669]
$In_{0.17}Al_{0.83}N$/GaN	0.15	–	I	XPS	[670]
$In_{0.25}Al_{0.75}N$/GaN	0.1 ± 0.2	0.4	I	XPS	[399]
$In_{0.3}Al_{0.7}N$/GaN	0.0 ± 0.2	0.2	I	XPS	[399]
$Al_xGa_{1-x}N$/GaN	0.3*x*	–	I	Theory (tight binding)	[671]
$B_{0.14}Al_{0.86}N$/GaN	0	2.1 ± 0.2	I	HRXPS	[672]
$B_{0.14}Al_{0.86}N/Al_{0.70}Ga_{0.30}N$	0.4 ± 0.05	0.1 ± 0.05	II	HRXPS	[673]
InN/($\bar{2}$01) β-Ga_2O_3	–0.55 ± 0.11	–3.35 ± 0.11	I	HRXPS	[674]
ITO/($\bar{2}$01) β-Ga_2O_3	–0.78 ± 0.3	–0.32 ± 0.13	I	HRXPS	[675]
ITO/(010) β-$(Al_{0.14}Ga_{0.86})_2O_3$	–1.18 ± 0.2	0.32 ± 0.05	I	HRXPS	[676]
Al_2O_3/(010) β-$(Al_{0.14}Ga_{0.86})_2O_3$	0.23 ± 0.04	1.67 ± 0.3	I	HRXPS	[677]
Wurtzite InN/h-BN	–0.3 ± 0.09	4.99 ± 0.09	II	XPS	[678]
GaN/single-layer MoS_2	1.86 ± 0.08	0.56 ± 0.1	II	HRXPS	[636]
$In_{0.15}Al_{0.85}N/MoS_2$	2.08 ± 0.15	0.6 ± 0.15	I	HRXPS	[635]

ors by grading the $Al_xGa_{1-x}N$/GaN ($0 \leqslant x \leqslant 0.3$) heterojunctions over a distance of ≈ 100 nm[689]. The polarization-induced bulk charge, also referred to as 3D electron slap (3DES), mimics a local donor with zero activation energy, overcoming the localized optical transitions associated with the defect centers of donor atoms. Such carriers are not rendered thermally inert at low temperatures, unlike the shallow donor-doped bulk carriers. Thus, absence of ionized impurity scattering results in high mobilities of charge carriers; consequently, improved carrier injection efficiency can be achieved. Subsequently, Simon *et al.* reported ionization of the magnesium acceptor dopants utilizing built-in polarization fields in bulk wurtzite semiconductors[178]. These field-ionized holes can oppose thermal freeze-out effects, resulting in major improvement in p-type electrical conductivity. This doping scheme helped improve optical emission efficiency in UV LED structures. Thus, polarization-induced doping renders a solution to enhance carrier injection efficiency in wide-bandgap $Al_xGa_{1-x}N$ semiconductors. In contrast, the incorporation of an $Al_xGa_{1-x}N$ layer as an electron-blocking layer (EBL) results in polarization-induced electron gas at the $Al_xGa_{1-x}N$/GaN interface, leading electrons to leak toward the p-type GaN layer. To overcome this leakage issue, polarization inverted EBL was proposed, but inverting the polarity during the growth remained challenging[690]. Later, Kuo *et al.* replaced the GaN last quantum barrier (QB) with an $In_{0.01}Ga_{0.99}N$/GaN heterojunction, which aided in the development of an upward band bending at the last GaN barrier, resulting in an effective electron blocking by the EBL[691]. Despite the difficulty in growing $In_xAl_{1-x}N$[692], $In_{0.20}Al_{0.80}N$ acting as an EBL that was well lattice-matched with GaN reduced the piezo-polarization effect and electron leakage[693].

With experimental evidence, Zhang *et al.* computationally demonstrated that silicon step-doping of quantum barriers would lower polarization-induced fields and reduce energy barriers for hole transport[694]. They compared three devices differing solely in terms of doping in barrier layers. Device I is a standard LED with unintentionally doped barriers, while devices II and III consist of silicon-doped layers and step-doped barriers, respectively, as shown in Fig. 24(a). Figs. 24(b) and 24(c) respectively show the experimentally measured and numerically simulated optical output power and EQE as functions of injection currents for devices I, II, and III. Considering the entire current range, device III outperformed I and II. The silicon step-doping suppressed QCSE and enhanced hole injection, consequently improving LED performance.

6.3. State of current injection efficiency and $Al_xGa_{1-x}N$-based UV LEDs

With the advancement of technology, there is a colossal demand for high power and highly efficient UV optoelectronic devices because of their diverse application (water/air/food sterilization, surface disinfection, free-space non-line-of-sight communication, epoxy curing, counterfeit detection, fluorescence or Raman identification of biological/chemical

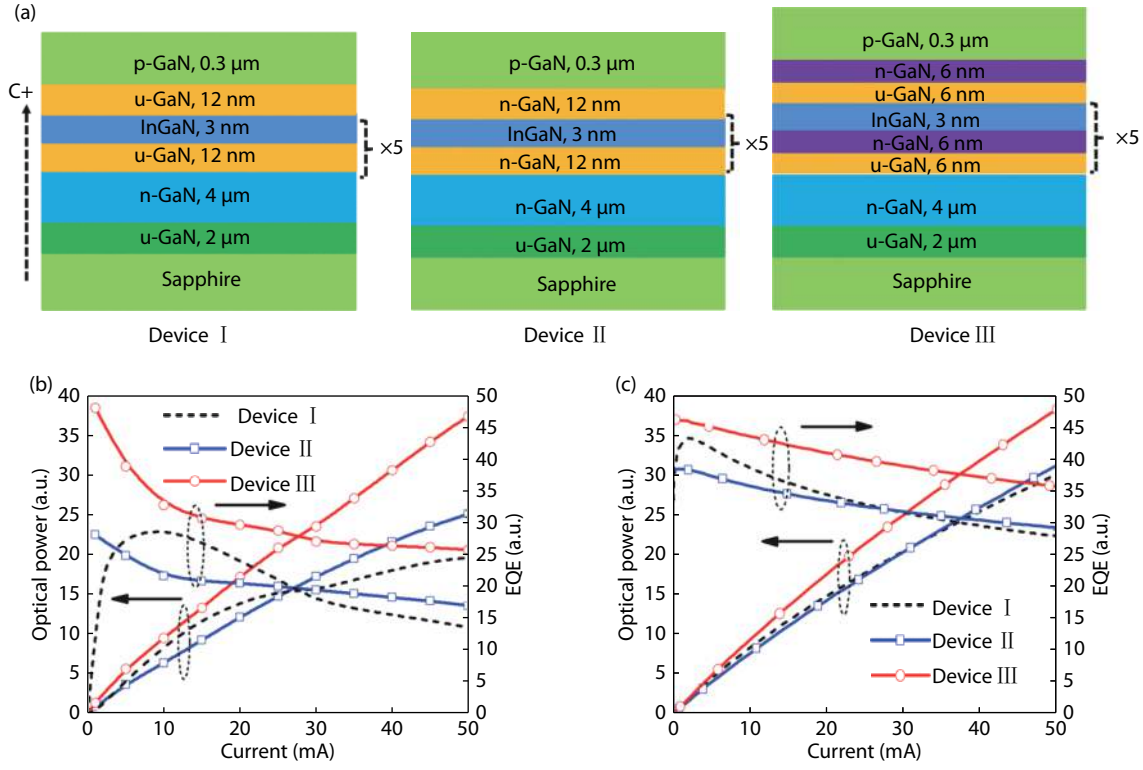

Fig. 24. (Color online) (a) Schematic representation of the LEDs. Device I is a standard LED with unintentionally doped barriers, device II is designed with 12 nm-thick barriers, each fully doped with Si, and device III features step-doped barriers (6 nm undoped and followed by 6 nm doped). (b) and (c) respectively show the experimentally measured and numerically simulated optical output power and EQE as a function of current for devices I, II, and III. Reprinted with permission from Ref. [694]. ©2013, IEEE.

agents, and various diagnostic and therapeutic medical functions)[695, 402]. With such a diversity in potential applications, as exciting as it may sound, UV optoelectronic devices are far from perfected. Thus, there is a plenty to improve in materials system (choice of material, synthesis/growth), device structure (fabrication), and packaging.

EQE of a light-emitting device (Fig. 25(a)) is the product of electrical injection efficiency (EE), IQE, and LEE, and typical values are shown in Fig. 25(b)[696]. EQE for the UV LEDs and LDs has been improved over time by tweaking materials or structures; however, it is still noticeably lacking[402]. One of the major bottlenecks for abysmal EQE is poor current injection. In this section, we highlight the techniques utilized to improve current injection of UV optoelectronic devices.

Current injection is affected by numerous factors: metal contacts, interfaces in between contact material and electron/hole supplier layers, concentration of electron/hole in electron/hole supplier layers, electrical conductivity, and electric field (piezoelectric field) developed across the active region. Both p- and n-type doping became challenging in DUV $Al_xGa_{1-x}N$-based devices due to high aluminum concentrations[697]. High ionization energy of magnesium and lower mobility worsen the hole injection, which creates imbalance in charge carrier injection[698, 91]. Thus, research problems, achievements, and prospects on the enhancement of hole injection are worthy of discussion. The key factors that require attention for the enhancement of hole injection are outlined in Fig. 26.

When a device is electrically biased, the very first hurdle that a hole encounters is the interface of the p-type metal contact and the hole supplier layer[699]. In 1999, Ho *et al.* demonstrated a low specific contact resistance to p-type GaN where a Ni/Au thin film was deposited on p-type GaN and annealed at 500 °C in air to form NiO and obtain specific contact resistances as low as 4×10^{-6} Ω [700]. This technique is one of the popular techniques to obtain low specific contact resistances to date. Other metal combinations utilized in enriching p-type Ohmic contacts include zinc-nickel (ZnNi)/indium tin oxide (ITO)[701], ruthenium (Ru)/Ni/iridium (Ir)[702], and Ti/Au[699]. In addition, contact interfaces can be improved by manipulating the polarization effect and adopting superlattice structures[703] and tunnel junctions[704–706].

In the majority of UV LED devices, a hole supplier layer consists of p-type GaN and $Al_xGa_{1-x}N$ layers. As a hole reaches the hole supply layer, it encounters a high discontinuity in the valance band at the heterojunction, which makes the hole transport challenging. Graded heterojunctions[707], $Al_xGa_{1-x}N$/ $Al_yGa_{1-y}N$ ($x > y$) superlattice structures[708–710], polarized induced electric fields[178, 711] (as shown in Fig. 27), and magnesium-delta doping[416, 180] are some of the major techniques employed to enhance the hole transport within the hole supplier layer, lowering the activation energy of magnesium dopants to as low as 17 meV. In addition, drift velocity can be significantly increased utilizing the strong field produced at the interface (for aluminum-rich p-$Al_xGa_{1-x}N$ and p-GaN) of heterojunction in the hole supply layer[712].

Electron leakage under high bias currents is inevitable. An EBL is not only thought to be capable of minimizing electron leakage, but also hindering hole transport because of the discontinuity of the valance band[652, 707, 713]. Mehnke *et*

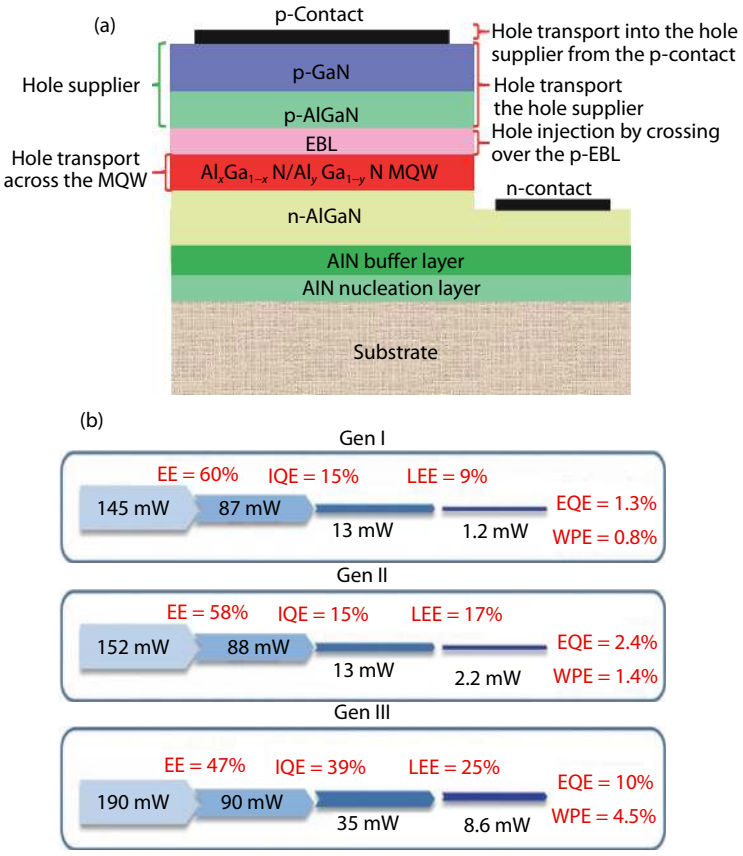

Fig. 25. (Color online) (a) Schematic diagram of an $Al_xGa_{1-x}N$-based UV LED. (Reprinted with permission from Ref. [652]. ©2017, MDPI). (b) Illustration of EQE of UV LEDs under different circumstances. (Reprinted with permission from Ref. [696]. ©2014, IOP Publishing).

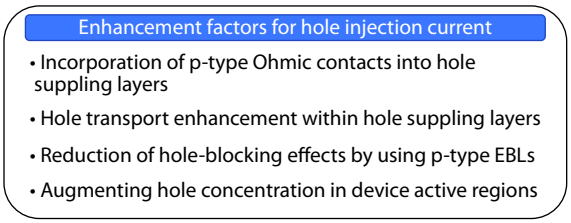

Fig. 26. (Color online) An outline that underscores essential factors for enhancement in hole injection current.

al. implemented AlN electron blocking heterostructures (EBHs) in $Al_xGa_{1-x}N$-based MQW LEDs with peak emission below 250 nm[714]. Owing to the EBHs, the emission from the QW was enhanced, whereas long wavelength parasitic luminescence was significantly reduced. Consequently, adequate hole injection was maintained by optimizing thickness of the EBH. Using such device structure, UV-C LED with peak emission at 234 nm, optical power of 14.5 μW, and EQE of 0.012% at current density of 18.2 A/cm^2 was demonstrated. AlN is optically transparent for DUV (> 210 nm) and often used as a QB layer in $Al_xGa_{1-x}N$-based MQW LEDs. However, carrier injection is severely hindered by poor conductivity of AlN. Thus, there is a common practice of doping the QBs. Tsai *et al.* revealed a DUV LED device structure that utilizes an intrinsic QB on high-quality AlN template[715]. It is confirmed that the output power was improved as a result of restricted diffusion of magnesium tunneling into the MQW region and suppression of the sub-band parasitic emissions. To exploit the intraband-tunneling assisted hole injection, Zhang *et al.* proposed a p-type EBL with a very thin insertion layer having smaller energy bandgap[712].

Holes in the active regions of visible LEDs tend to accumulate close to the interface between the MQW region and the p-type EBL; however, this is not the case in DUV LEDs[716, 717]. Furthermore, hole distribution in the active region can be modifiedthroughmanipulationofaluminumcompositioninAl$_x$Ga$_{1-x}$N QWs and QBs. It has been observed that band offset is reduced, which is beneficial for hole transport across the active region[717]. Enhancement of hole concentration in each QW appears more easily accomplished than uniform hole distribution across an entire active region. The thicknesses of the QWs and QBs also affect hole concentration. Fewer than a couple nanometers of QW thickness and less than 8 nm for QB are the thicknesses recommended for the high hole concentrations and excellent spatial overlap of the electron–hole wavefunctions[718–721].

7. Outlook and future challenges

While sapphire is intrinsically nonconductive, Ga_2O_3 substrates can be highly conductive and UV transparent, though the carrier mobilities are relatively low compared to GaN[722, 723]. Background impurities do not make sapphire conductive and only increase absorption in the UV region, while AlN templates are currently highly resistive, and AlN substrates suffer from point crystal defects within the UV regime[724–728]. Therefore, from the prospective of device fabrication, optoelectronic devices fabricated on AlN/sapphire require an etch down process that is cumbersome to implement, resulting in laterally-oriented devices exhibiting poor electron injection. AlN substrates might be the ideal choice in development of next-

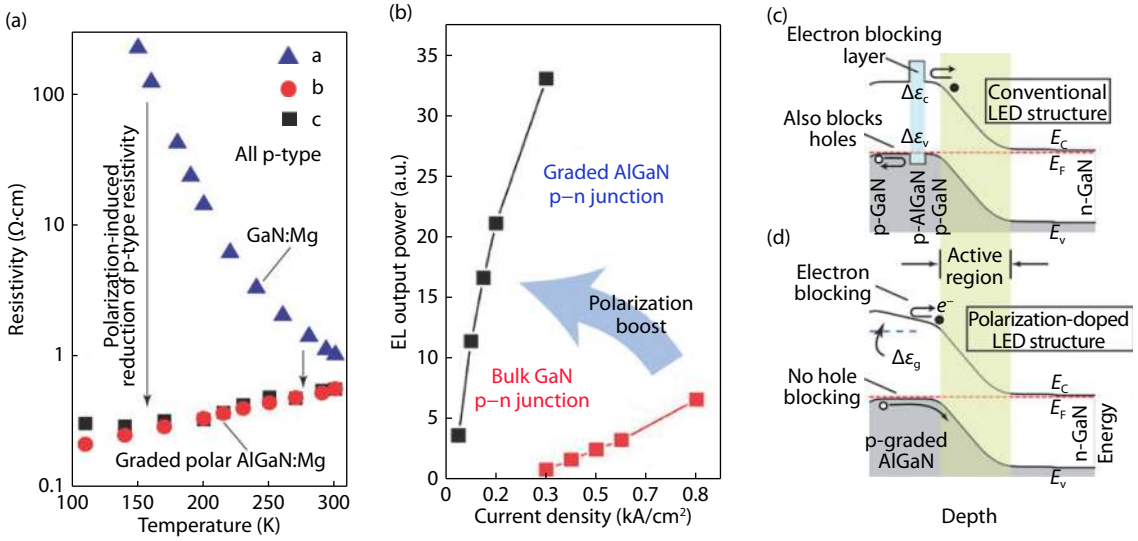

Fig. 27. (Color online) (a) Measured temperature-dependent resistivity for different $Al_xGa_{1-x}N$ samples highlighting the polarization boost in p-type conductivity. Sample a is a magnesium-doped GaN sample, while samples b and c are doped with the same magnesium concentration but linearly graded from $x = 0$ to $x = 0.16$ and $x = 0$ to $x = 0.3$, respectively. (b) relative output power intensity with increasing drive current for the graded $Al_xGa_{1-x}N$ p–n junction and the control bulk-doped p–n junction. Schematic energy-band diagrams of (c) a conventional LED device and (d) a polarization-doped device. Reprinted with permission from Ref. [178]. ©2010, American Association for the Advancement of Science.

generation $Al_xGa_{1-x}N$-based DUV optoelectronic devices because $Al_xGa_{1-x}N$ TDDs can be substantially reduced to values between 10^5 cm^{-2} and 10^5 cm^{-2}, but cost-wise, they are not currently available for practical applications[99, 324, 391, 729–739]. Tokuyama Corporation in Japan reported EQEs of 2.2% and 2.4% for DUV LEDs grown on AlN substrates at 20 mA and 250 mA injection currents, respectively[740, 741], whereas Crystal IS, Inc. in the United States reported up to 4.9% and 5.9% EQEs at 300 mA and 50 mA, respectively, demonstrating low thermal roll-off of up to a 300 mA injection current[742]. Vertically-oriented devices with backside n-type contacts, on the other hand, demonstrate better current injection characteristics. Nanowire structures exhibit unique characteristics, such as lateral strain relaxation and the absence of lattice mismatches with the substrate and structural cracking. Hence, we anticipate that future efficient DUV optoelectronic devices will take advantage of the unparalleled features unleashed by combining nanostructured devices and Ga_2O_3 substrates. 2D materials and hybrid systems, such as phosphorene[743, 744], phosphorene-like structures[745, 746], 2D TMD heterojunctions[747–752], and graphene/h-BN heterostructures[753, 754], have also been used to improve the use of contact interfacial layers as tunnel layers[755–758], and are occasionally utilized for light coupling in visible and IR regimes because of their narrow bandgaps and high absorption of the signal[759]. We summarized key performance characteristics of state-of-the-art group III–nitride-based and hybrid UV and DUV PDs, as demonstrated in Table 3. Compared to recently emerging wide bandgap energy materials, most notably Ga_2O_3 and its alloys[760–781], $Al_xGa_{1-x}N$-based PDs remain the mature technology for eventual integration into various applications. Although Ga_2O_3-based PDs have been demonstrated with high responsivity (1.8 A/W at 236 nm),[782] the spectral response is relatively broad and is not easily tunable, compared to that of $Al_xGa_{1-x}N$-based material. Apart from that, slow response speeds of up to few seconds were also observed in Ga_2O_3-based PDs due to surface trap states and slow hole transport[782, 783]. These issues would eventually hinder their applicability in systems requiring high selectivity or fast response speed, particularly for wavelength-selective communication channels[784, 785]. BN-based PDs, on the other hand, may still require extensive fundamental study and device optimization before realizing a reliable device with high responsivity and response speed comparable to what $Al_xGa_{1-x}N$-based PDs can realize. Nevertheless, we envision that future development of $Al_xGa_{1-x}N$-based PDs or APDs will heavily rely and focus on 1) epitaxial growth optimization of high-aluminum-content layers for DUV detection, 2) maximizing transient response for communication applications, 3) increasing photocurrent gain, and 4) lowering operating requirements through device optimization, in order to achieve integration on UV or DUV photonic integrated circuits and applications.

Acknowledgements

We acknowledge the financial support from the King Abdulaziz City for Science and Technology (KACST) under grant no. KACST TIC R2-FP-008. This work was partially supported by the King Abdullah University of Science and Technology (KAUST) baseline funding no. BAS/1/1614-01-01, and MBE equipment funding no. C/M-20000-12-001-77 and KCR/1/4055-01-01.

References

[1] Wang L, Xie R J, Suehiro T, et al. Down-conversion nitride materials for solid state lighting: Recent advances and perspectives. Chem Rev, 2018, 118, 1951

[2] Alhassan A I, Young N G, Farrell R M, et al. Development of high performance green *c*-plane III-nitride light-emitting diodes. Opt Express, 2018, 26, 5591

[3] Pimputkar S, Speck J S, DenBaars S P, et al. Prospects for LED lighting. Nat Photonics, 2009, 3, 180

[4] Kim J S, Jeon P E, Park Y H, et al. White-light generation through ultraviolet-emitting diode and white-emitting phosphor. Appl

Phys Lett, 2004, 85, 3696
[5] Matafonova G, Batoev V. Recent advances in application of UV light-emitting diodes for degrading organic pollutants in water through advanced oxidation processes: A review. Water Res, 2018, 132, 177
[6] Chen J, Loeb S, Kim J H. LED revolution: fundamentals and prospects for UV disinfection applications. Environ Sci: Water Res Technol, 2017, 3, 188
[7] Chen Q, Zhang H, Dai J. Enhanced the optical power of AlGaN-based deep ultraviolet light-emitting diode by optimizing mesa sidewall angle. IEEE Photonics J, 2018, 10, 6100807
[8] Hirayama H, Fujikawa S, Kamata N. Recent progress in AlGaN-based deep-UV LEDs. Electron Commun Jpn, 2015, 98, 1
[9] Aoyagi Y, Takeuchi M, Yoshida K, et al. High-sensitivity ozone sensing using 280 nm deep ultraviolet light-emitting diode for detection of natural hazard ozone. J Environ Prot, 2012, 3, 695
[10] Würtele M, Kolbe T, Lipsz M, et al. Application of GaN-based ultraviolet-C light emitting diodes-UV LEDs-for water disinfection. Water Res, 2011, 45, 1481
[11] Alhamoud A A, Alfaraj N, Priante D, et al. Functional integrity and stable high-temperature operation of planarized ultraviolet-A $Al_xGa_{1-x}N/Al_yGa_{1-y}N$ multiple-quantum-disk nanowire LEDs with charge-trapping inhibition interlayer. Gallium Nitride Materials and Devices XIV. Vol. 10918, 2019, 109181X
[12] Jasuja K, Ayinde K, Wilson C L, et al. Introduction of protonated sites on exfoliated, large-area sheets of hexagonal boron nitride. ACS Nano, 2018, 12, 9931
[13] Pacilé D, Meyer J C, Girit Ç Ö, et al. The two-dimensional phase of boron nitride: Few-atomic-layer sheets and suspended membranes. Appl Phys Lett, 2008, 92, 133107
[14] Srinivasan S, Stevens M, Ponce F A, et al. Carrier dynamics and electrostatic potential variation in InGaN quantum wells grown on $\{11\bar{2}2\}$ GaN pyramidal planes. Appl Phys Lett, 2006, 89, 231908
[15] ElAfandy R T, Majid M A, Ng T K, et al. Exfoliation of threading dislocation-free, singlecrystalline, ultrathin gallium nitride nanomembranes. Adv Funct Mater, 2014, 24, 2305
[16] Hirayama H. Ultraviolet LEDs. In: Nitride Semiconductor Light-Emitting Diodes (LEDs). Elsevier, 2014, 497
[17] Orji N G, Badaroglu M, Barnes B M, et al. Metrology for the next generation of semiconductor devices. Nat Electron, 2018, 1, 532
[18] Ayari T, Sundaram S, Li X, et al. Heterogeneous integration of thin-film InGaN-based solar cells on foreign substrates with enhanced performance. ACS Photonics, 2018, 5, 3003
[19] Liu S, Sheng B, Wang X, et al. Molecular beam epitaxy of single-crystalline aluminum film for low threshold ultraviolet plasmonic nanolasers. Appl Phys Lett, 2018, 112, 231904
[20] Yuan C, Pomeroy J W, Kuball M. Above bandgap thermoreflectance for non-invasive thermal characterization of GaN-based wafers. Appl Phys Lett, 2018, 113, 102101
[21] Jiang J, Guo W, Xu H, et al. Performance enhancement of ultraviolet light emitting diode incorporating Al nanohole arrays. Nanotechnology, 2018, 29, 45LT01
[22] Ishibe T, Kurokawa T, Naruse N, et al. Resistive switching at the high quality metal/insulator interface in $Fe_3O_4/SiO_2/\alpha$-$FeSi_2$/Si stacking structure. Appl Phys Lett, 2018, 113, 141601
[23] Priante D, Janjua B, Prabaswara A, et al. Highly uniform ultraviolet-A quantum-confined AlGaN nanowire LEDs on metal/silicon with a TaN interlayer. Opt Mater Express, 2017, 7, 4214
[24] Sumikura H, Kuramochi E, Notomi M. Nonlinear optical absorption of beryllium isoelectronic centers doped in silicon waveguides. Appl Phys Lett, 2018, 113, 141101
[25] Priante D, Janjua B, Prabaswara A, et al Ti/TaN bilayer for efficient injection and reliable AlGaN nanowires LEDs. Conference on Lasers and ElectroOptics, 2018, JTu2A.91
[26] Zhang R, Zhao B, Huang K, et al. Silicon-on-insulator with hybrid orientations for heterogeneous integration of GaN on Si (100) substrate. AIP Adv, 2018, 8, 055323
[27] Patil S S, Johar M A, Hassan M A, et al. Anchoring MWCNTs to 3D honeycomb ZnO/GaN heterostructures to enhancing photoelectrochemical water oxidation. Appl Catal B, 2018, 237, 791
[28] Ajima Y, Nakamura Y, Murakami K, et al. Room-temperature bonding of GaAs//Si and GaN//GaAs wafers with low electrical resistance. Appl Phys Express, 2018, 11, 106501
[29] Liu X, Sun C, Xiong B, et al. Generation of multiple near-visible comb lines in an AlN microring via $\chi^{(2)}$ and $\chi^{(3)}$ optical nonlinearities. Appl Phys Lett, 2018, 113, 171106
[30] Zhao C, Alfaraj N, Subedi R C, et al. III-nitride nanowires on unconventional substrates: From materials to optoelectronic device applications. Prog Quantum Electron, 2018, 61, 1
[31] Houlton J P, Brubaker M D, Martin D O, et al. An optical Bragg scattering readout for nano-mechanical resonances of GaN nanowire arrays. Appl Phys Lett, 2018, 113, 123102
[32] Maity A, Grenadier S J, Li J, et al. Hexagonal boron nitride neutron detectors with high detection efficiencies. J Appl Phys, 2018, 123, 044501
[33] Maity A, Grenadier S J, Li J, et al. Toward achieving flexible and high sensitivity hexagonal boron nitride neutron detectors. Appl Phys Lett, 2017, 111, 033507
[34] Ahmed K, Dahal R, Weltz A, et al. Solid-state neutron detectors based on thickness scalable hexagonal boron nitride. Appl Phys Lett, 2017, 110, 023503
[35] Alden D, Troha T, Kirste R, et al. Quasi-phase-matched second harmonic generation of UV light using AlN waveguides. Appl Phys Lett, 2019, 114, 103504
[36] Bruch A W, Liu X, Guo X, et al. 17000%/W second-harmonic conversion efficiency in single-crystalline aluminum nitride microresonators. Appl Phys Lett, 2018, 113, 131102
[37] Du C, Hu W, Wang Z L. Recent progress on piezotronic and piezo-phototronic effects in III-group nitride devices and applications. Adv Eng Mater, 2018, 20, 1700760
[38] Kim H J, Jung S I, Segovia-Fernandez J, et al. The impact of electrode materials on $1/f$ noise in piezoelectric AlN contour mode resonators. AIP Adv, 2018, 8, 055009
[39] Cassella C, Chen G, Qian Z, et al. RF passive components based on aluminum nitride crosssectional lamé-mode MEMS resonators. IEEE Trans Electron Devices, 2017, 64, 237
[40] Wang X, Song J, Zhang F, et al. Electricity generation based on one-dimensional group-III nitride nanomaterials. Adv Mater, 2010, 22, 2155
[41] Yu R, Wu W, Ding Y, et al. GaN nanobelt-based strain-gated piezotronic logic devices and computation. ACS Nano, 2013, 7, 6403
[42] Zhang H, Zhang Q, Lin M, et al. A GaN/InGaN/AlGaN MQW RTD for versatile MVL applications with improved logic stability. J Semicond, 2018, 39, 074004
[43] Springbett H, Gao K, Jarman J, et al. Improvement of single photon emission from InGaN QDs embedded in porous micropillars. Appl Phys Lett, 2018, 113, 101107
[44] Bourrellier R, Meuret S, Tararan A, et al. Bright UV single photon emission at point defects in h-BN. Nano Lett, 2016, 16, 4317
[45] Vuong T, Cassabois G, Valvin P, et al. Phonon-photon mapping in a color center in hexagonal boron nitride. Phys Rev Lett, 2016, 117, 097402
[46] Elafandy R T, Ebaid M, Min J W, et al. Flexible InGaN nanowire membranes for enhanced solar water splitting. Opt Express, 2018, 26, A640
[47] Zhang H, Ebaid M, Min J W, et al. Enhanced photoelectrochemical performance of InGaN-based nanowire photoanodes by optimizing the ionized dopant concentration. J Appl Phys, 2018, 124, 083105
[48] Kim Y J, Lee G J, Kim S, et al. Efficient light absorption by GaN truncated nanocones for high performance water splitting applications. ACS Appl Mater Interfaces, 2018, 10, 28672

[49] Ebaid M, Min J W, Zhao C, et al. Water splitting to hydrogen over epitaxially grown InGaN nanowires on a metallic titanium/silicon template: reduced interfacial transfer resistance and improved stability to hydrogen. J Mater Chem A, 2018, 6, 6922

[50] Ebaid M, Priante D, Liu G, et al. Unbiased photocatalytic hydrogen generation from pure water on stable Ir-treated $In_{0.33}Ga_{0.67}$-N nanorods. Nano Energy, 2017, 37, 158

[51] Sekimoto T, Hashiba H, Shinagawa S, et al. Wireless InGaN-Si/Pt device for photo-electrochemical water splitting. Jpn J Appl Phys, 2016, 55, 088004

[52] Lin C H, Fu H C, Cheng B, et al. A flexible solar-blind 2D boron nitride nanopaper-based photodetector with high thermal resistance. NPJ 2D Mater Appl, 2018, 2, 23

[53] Tan X, Lv Y J, Zhou X Y, et al. AlGaN/GaN pressure sensor with a Wheatstone bridge structure. AIP Adv, 2018, 8, 085202

[54] Mehnke F, Guttmann M, Enslin J, et al. Gas sensing of nitrogen oxide utilizing spectrally pure deep UV LEDs. IEEE J Sel Top Quantum Electron, 2017, 23, 29

[55] Pyo J Y, Jeon J H, Koh Y, et al. AlGaN/GaN high-electronmobility transistor pH sensor with extended gate platform. AIP Adv, 2018, 8, 085106

[56] Cao H, Ma Z, Sun B, et al. Composite degradation model and corresponding failure mechanism for mid-power GaN-based white LEDs. AIP Adv, 2018, 8, 065108

[57] Janjua B, Ng T K, Zhao C, et al. True yellow light-emitting diodes as phosphor for tunable color-rendering index laser-based white light. ACS Photonics, 2016, 3, 2089

[58] Guo W, Banerjee A, Bhattacharya P, et al. InGaN/GaN disk-in-nanowire white light emitting diodes on (001) silicon. Appl Phys Lett, 2011, 98, 193102

[59] Lee C, Shen C, Cozzan C, et al. Gigabit-per-second white light-based visible light communication using near-ultraviolet laser diode and red-, green-, and blue-emitting phosphors. Opt Express, 2017, 25, 17480

[60] Yu F, Strempel K, Fatahilah M F, et al. Normally off vertical 3-D GaN nanowire MOSFETs with inverted p-GaN channel. IEEE Trans Electron Devices, 2018, 65, 2439

[61] Yin L, Du G, Liu X. Impact of ambient temperature on the self-heating effects in FinFETs. J Semicond, 2018, 39, 094011

[62] Alfaraj N, Hussain A M, Torres Sevilla G A, et al. Functional integrity of flexible n-channel metal-oxide-semiconductor fieldeffect transistors on a reversibly bistable platform. Appl Phys Lett, 2015, 107, 174101

[63] Zhou X, Tan X, Wang Y, et al. Coeffect of trapping behaviors on the performance of GaN-based devices. J Semicond, 2018, 39, 094007

[64] Zhao J, Xing Y, Fu K, et al. Influence of channel/back-barrier thickness on the breakdown of AlGaN/GaN MISHEMTs. J Semicond, 2018, 39, 094003

[65] Mallick G, Elder R M. Graphene/hexagonal boron nitride heterostructures: Mechanical properties and fracture behavior from nanoindentation simulations. Appl Phys Lett, 2018, 113, 121902

[66] Zhang Z, Chen J. Thermal conductivity of nanowires. Chin Phys B, 2018, 27, 035101

[67] Sztein A, Bowers J E, DenBaars S P, et al. Polarization field engineering of GaN/AlN/AlGaN superlattices for enhanced thermoelectric properties. Appl Phys Lett, 2014, 104, 042106

[68] Sztein A, Bowers J E, DenBaars S P, et al. Thermoelectric properties of lattice matched InAlN on semi-insulating GaN templates. J Appl Phys, 2012, 112, 083716

[69] Sztein A, Ohta H, Sonoda J, et al. GaN-based integrated lateral thermoelectric device for micro-power generation. Appl Phys Express, 2009, 2, 111003

[70] Liu W, Balandin A A. Thermoelectric effects in wurtzite GaN and $Al_xGa_{1-x}N$ alloys. J Appl Phys, 2005, 97, 123705

[71] Mark S. Lundstrom (private communication, 2017)

[72] Wang D, Chen Z Y, Wang T, et al. Repeatable asymmetric resonant tunneling in AlGaN/GaN double barrier structures grown on sapphire. Appl Phys Lett, 2019, 114, 073503

[73] Franckié M, Bosco L, Beck M, et al. Two-well quantum cascade laser optimization by non-equilibrium Green's function modelling. Appl Phys Lett, 2018, 112, 021104

[74] Andrews A M, Zederbauer T, Detz H, et al. THz quantum cascade lasers. In: Molecular Beam Epitaxy. Elsevier, 2018, 597

[75] Wang F, Lee J, Phillips D J, et al. A high-efficiency regime for gas-phase terahertz lasers. Proc Natl Acad Sci USA, 2018, 115, 6614

[76] Encomendero J, Yan R, Verma A, et al. Room temperature microwave oscillations in GaN/AlN resonant tunneling diodes with peak current densities up to 220 kA/cm^2. Appl Phys Lett, 2018, 112, 103101

[77] Encomendero J, Faria F A, Islam S M, et al. New tunneling features in polar III-nitride resonant tunneling diodes. Phys Rev X, 2017, 7, 041017

[78] Alves T E P, Kolodziej C, Burda C, et al. Effect of particle shape and size on the morphology and optical properties of zinc oxide synthesized by the polyol method. Mater Des, 2018, 146, 125

[79] Ghoneim M T, Sadraei A, P de Souza, et al. A protocol to characterize pH sensing materials and systems. Small Methods, 2019, 3, 1800265

[80] Lan W, Yang Z, Zhang Y, et al. Novel transparent high-performance AgNWs/ZnO electrodes prepared on unconventional substrates with 3D structured surfaces. Appl Surf Sci, 2018, 433, 821

[81] Zhang B P, Binh N T, Wakatsuki K, et al. Growth of ZnO/MgZnO quantum wells on sapphire substrates and observation of the two-dimensional confinement effect. Appl Phys Lett, 2005, 86, 032105

[82] Maeda T, Narita T, Kanechika M, et al. Franz-Keldysh effect in GaN p–n junction diode under high reverse bias voltage. Appl Phys Lett, 2018, 112, 252104

[83] Maeda T, Chi X, Horita M, et al. Phonon-assisted optical absorption due to Franz-Keldysh effect in 4H-SiC p-n junction diode under high reverse bias voltage. Appl Phys Express, 2018, 11, 091302

[84] Bridoux G, Villafuerte M, Ferreyra J M, et al. Franz-Keldysh effect in epitaxial ZnO thin films. Appl Phys Lett, 2018, 112, 092101

[85] Tangi M, Min J W, Priante D, et al. Observation of piezotronic and piezophototronic effects in n-InGaN nanowires/Ti grown by molecular beam epitaxy. Nano Energy, 2018, 54, 264

[86] Elahi H, Eugeni M, Gaudenzi P. A review on mechanisms for piezoelectric-based energy harvesters. Energies, 2018, 11, 1850

[87] Dan M, Hu G, Li L, et al. High performance piezotronic logic nanodevices based on GaN/InN/GaN topological insulator. Nano Energy, 2018, 50, 544

[88] Zhu R, Yang R. Introduction to the piezotronic effect and sensing applications. In: Synthesis and Characterization of Piezotronic Materials for Application in Strain/Stress Sensing. Springer, 2018, 1

[89] Zhao C, Ebaid M, Zhang H, et al. Quantified hole concentration in AlGaN nanowires for high-performance ultraviolet emitters. Nanoscale, 2018, 10, 15980

[90] Liang Y H, Towe E. Progress in efficient doping of high aluminum-containing group III-nitrides. Appl Phys Rev, 2018, 5, 011107

[91] Amano H, Kito M Hiramatsu K, et al. P-type conduction in Mg-doped GaN treated with low-energy electron beam irradiation (LEEBI). Jpn J Appl Phys, 1989, 28, L2112

[92] Akasaki I, Amano H, Kito M, et al. Photoluminescence of Mg-doped p-type GaN and electroluminescence of GaN p–n junction LED. J Lumin, 1991, 48, 666

[93] Nakamura S, Senoh M, S Nagahama, et al. InGaN/GaN/AlGaN-based laser diodes with modulation-doped strained-layer superlattices grown on an epitaxially laterally overgrown GaN sub-

strate. Appl Phys Lett, 1998, 72, 211
[94] Nakamura S, Senoh M, Nagahama S, et al. InGaN-based multi-quantum-well-structure laser diodes. Jpn J Appl Phys, 1996, 35, L74
[95] Nakamura S, Mukai T, Senoh M. Candela-class high-brightness InGaN/AlGaN double-heterostructure blue-lightemitting diodes. Appl Phys Lett, 1994, 64, 1687
[96] Amano H, Kitoh M, Hiramatsu K, et al. Growth and luminescence properties of Mg-doped GaN prepared by MOVPE. J Electrochem Soc, 1990, 137, 1639
[97] Bilenko Y, Lunev A, Hu X, et al. 10 milliwatt pulse operation of 265 nm AlGaN light emitting diodes. Jpn J Appl Phys, 2004, 44(L98), L98
[98] Bigio I J, Mourant J R. Ultraviolet and visible spectroscopies for tissue diagnostics: fluorescence spectroscopy and elastic-scattering spectroscopy. Phys Med Biol, 1997, 42, 803
[99] Hirayama H, Maeda N, Fujikawa S, et al. Recent progress and future prospects of AlGaN-based high-efficiency deep-ultraviolet light-emitting diodes. Jpn J Appl Phys, 2014, 53, 100209
[100] Kang B S, Wang H T, Ren F, et al. Electrical detection of biomaterials using AlGaN/GaN high electron mobility transistors. J App Phys, 2008, 104, 8
[101] Cho H K, Külberg A, Ploch N L, et al. Bow reduction of AlInGaN-based deep UV LED wafers using focused laser patterning. IEEE Photonics Technol Lett, 2018, 30, 1792
[102] Janjua B, Priante D, Prabaswara A, et al. Ultraviolet-A LED based on quantum-disks-in-AlGaN-nanowires –Optimization and device reliability. IEEE Photonics J, 2018, 10, 2200711
[103] SaifAddin B, Zollner C J, Almogbel A, et al. Developments in AlGaN and UVC LEDs grown on SiC. In: Light-Emitting Diodes: Materials, Devices, and Applications for Solid State Lighting XXII. Vol. 10554. International Society for Optics and Photonics, 2018, 105541E
[104] Islam S M, Protasenko V, Bharadwaj S, et al Enhancing wall-plug efficiency for deep-UV light-emitting diodes: From crystal growth to devices. In: Light-Emitting Diodes. Springer, 2019, 337.
[105] Wang X, Peng W, Yu R, et al. Simultaneously enhancing light emission and suppressing efficiency droop in GaN microwire-based ultraviolet light-emitting diode by the piezo-phototronic effect. Nano Lett, 2017, 17, 3718
[106] Al Balushi Z Y, Redwing J M. In situ stress measurements during MOCVD growth of thick N-polar InGaN. J Appl Phys, 2017, 122, 085303
[107] Al Balushi Z Y, Redwing J M. The effect of polarity on MOCVD growth of thick InGaN. Appl Phys Lett, 2017, 110, 022101
[108] McLaurin M, Mates T E, Wu F, et al. Growth of p-type and n-type *m*-plane GaN by molecular beam epitaxy. J Appl Phys, 2006, 100, 063707
[109] Sugahara T, Sato H, Hao M, et al. Direct evidence that dislocations are non-radiative recombination centers in GaN. Jpn J Appl Phys, 1998, 37, L398
[110] Boguslawski P , Bernholc J. Doping properties of C, Si, and Ge impurities in GaN and AlN. Phys Rev B, 1997, 56, 9496
[111] Chen Z, Zhang X, Dou Z, et al. High-brightness blue light-emitting diodes enabled by a directly grown graphene buffer layer. Adv Mater, 2018, 30, 1801608
[112] Qi Y, Wang Y, Pang Z, et al. Fast growth of strain-free AlN on graphene-buffered sapphire. J Am Chem Soc, 2018, 140, 11935
[113] Yan P, Tian Q, Yang G, et al. Epitaxial growth and interfacial property of monolayer MoS_2 on gallium nitride. RSC Adv, 2018, 8, 33193
[114] Takano T, Mino T, Sakai J, et al. Deep-ultraviolet light-emitting diodes with external quantum efficiency higher than 20% at 275 nm achieved by improving light-extraction efficiency. Appl Phys Express, 2017, 10, 031002
[115] Nam K B, Nakarmi M L, Li J, et al. Mg acceptor level in AlN probed by deep ultraviolet photoluminescence. Appl Phys Lett, 2003, 83, 878
[116] Van de Walle C G, Stampfl C, Neugebauer J. Theory of doping and defects in III–V nitrides. J Cryst Growth, 1998, 189/190, 505
[117] Kolbe T, Knauer A, Chua C, et al. Optical polarization characteristics of ultraviolet (In)(Al)GaN multiple quantum well light emitting diodes. Appl Phys Lett, 2010, 97, 171105
[118] Cantu P, Keller S, Mishra U K, et al. Metalorganic chemical vapor deposition of highly conductive $Al_{0.65}Ga_{0.35}N$ films. Appl Phys Lett, 2003, 82, 3683
[119] Nam K B, Li J, Nakarmi M L, et al. Achieving highly conductive AlGaN alloys with high Al contents. Appl Phys Lett, 2002, 81, 1038
[120] Nippert F, Tollabi Mazraehno M, Davies M J, et al. Auger recombination in AlGaN quantum wells for UV light-emitting diodes. Appl Phys Lett, 2018, 113, 071107
[121] Kioupakis E, Rinke P, Delaney K T, et al. Indirect Auger recombination as a cause of efficiency droop in nitride light-emitting diodes. Appl Phys Lett, 2011, 98, 161107
[122] Zhang M, Bhattacharya P, Singh J, et al. Direct measurement of auger recombination in $In_{0.1}Ga_{0.9}N$/GaN quantum wells and its impact on the efficiency of $In_{0.1}Ga_{0.9}N$/GaN multiple quantum well light emitting diodes. Appl Phys Lett, 2009, 95, 201108
[123] Shen Y C, Mueller G O, Watanabe S, et al. Auger recombination in InGaN measured by photoluminescence. Appl Phys Lett, 2007, 91, 141101
[124] Yun J, Shim J I, Hirayama H. Analysis of efficiency droop in 280-nm AlGaN multiple-quantum-well light-emitting diodes based on carrier rate equation. Appl Phys Express, 2015, 8, 022104
[125] Dreyer C E, Alkauskas A, Lyons J L, et al. Gallium vacancy complexes as a cause of Shockley-Read-Hall recombination in III-nitride light emitters. Appl Phys Lett, 2016, 108, 141101
[126] Karpov S Y, Makarov Y N. Dislocation effect on light emission efficiency in gallium nitride. Appl Phys Lett, 2002, 81, 4721
[127] Nagasawa Y, Hirano A. A review of AlGaN-based deep-ultraviolet light-emitting diodes on sapphire. Appl Sci, 2018, 8, 1264
[128] Hakamata J, Kawase Y, Dong L, et al. Growth of high-quality AlN and AlGaN films on sputtered AlN/sapphire templates via high-temperature annealing. Phys Status Solidi B, 2018, 255, 1700506
[129] Nakamura S, Mukai T, Senoh M, et al. Thermal annealing effects on p-type Mg-doped GaN films. Jpn J Appl Phys, 1992, 31, L139
[130] Liang F, Yang J, Zhao D G, et al. Resistivity reduction of low temperature grown p-$Al_{0.09}Ga_{0.91}N$ by suppressing the incorporation of carbon impurity. AIP Adv, 2018, 8, 085005
[131] Hömmerich U, Nyein E E, Lee D, et al. Photoluminescence studies of rare earth (Er, Eu, Tm) in situ doped GaN. Mater Sci Eng B, 2003, 105, 91
[132] Chen M T, Lu M P, Wu Y J, et al. Near UV LEDs made with in situ doped p-n homojunction ZnO nanowire arrays. Nano Lett, 2010, 10, 4387
[133] Derluyn J, Boeykens S, Cheng K, et al. Improvement of AlGaN/GaN high electron mobility transistor structures by *in situ* deposition of a Si_3N_4 surface layer. J Appl Phys, 2005, 98, 054501
[134] Fujiwara H, Sasaki K. Amplified spontaneous emission from a surface-modified GaN film fabricated under pulsed intense UV laser irradiation. Appl Phys Lett, 2018, 113, 171606
[135] Ng T K, Yan J. Special section guest editorial: Semiconductor UV photonics. J Nanophotonics, 2018, 12, 043501
[136] Guo Y, Yan J, Zhang Y, et al. Enhancing the light extraction of AlGaN-based ultraviolet light-emitting diodes in the nanoscale. J Nanophotonics, 2018, 12, 043510
[137] Alias M S, Tangi M, Holguin-Lerma J A, et al. Review of nanophotonics approaches using nanostructures and nanofabrication for III-nitrides ultraviolet-photonic devices. J Nanophotonics, 2018, 12, 043508

[138] Min J W, Priante D, Tangi M, et al. Unleashing the potential of molecular beam epitaxy grown AlGaN-based ultraviolet-spectrum nanowires devices. J Nanophotonics, 2018, 12, 043511

[139] Sun J, Lu C, Song Y, et al. Recent progress in the tailored growth of two-dimensional hexagonal boron nitride via chemical vapour deposition. Chem Soc Rev, 2018, 47, 4242

[140] Jiang H X, Lin J Y. Hexagonal boron nitride for deep ultraviolet photonic devices. Semicond Sci Technol, 2014, 29, 084003

[141] Giovannetti G, Khomyakov P A, Brocks G, et al. Substrate-induced band gap in graphene on hexagonal boron nitride: *Ab initio* density functional calculations. Phys Rev B, 2007, 76, 073103

[142] Kang C H, Shen C, Saheed M S M, et al. Carbon nanotube-graphene composite film as transparent conductive electrode for GaN-based light-emitting diodes. Appl Phys Lett, 2016, 109, 081902

[143] Tangi M, Shakfa M K, Mishra P, et al. Anomalous photoluminescence thermal quenching of sandwiched single layer MoS_2. Opt Mater Express, 2017, 7, 3697

[144] Mak K F, He K, Lee C, et al. Tightly bound trions in monolayer MoS_2. Nat Mater, 2013, 12, 207

[145] Tadjer M J, Koehler A D, Freitas J A, et al. High resistivity halide vapor phase homoepitaxial β-Ga_2O_3 films Co-doped by silicon and nitrogen. Appl Phys Lett, 2018, 113, 192102

[146] Li W, Zhao X, Zhi Y, et al. Fabrication of cerium-doped β-Ga_2O_3 epitaxial thin films and deep ultraviolet photodetectors. Appl Opt, 2018, 57, 538

[147] Higashiwaki M, Jessen G H. The dawn of gallium oxide microelectronics. Appl Phys Lett, 2018, 112, 060401

[148] Peelaers H, Varley J B, Speck J S, et al. Structural and electronic properties of Ga_2O_3–Al_2O_3 alloys. Appl Phys Lett, 2018, 112, 242101

[149] Pearton S J, Yang J, Cary I V P H , et al. A review of Ga_2O_3 materials, processing, and devices. Appl Phys Rev, 2018, 5, 011301

[150] Yang T H, Fu H, Chen H, et al. Temperature-dependent electrical properties of β-Ga_2O_3 Schottky barrier diodes on highly doped single-crystal substrates. J Semicond, 2019, 40, 012801

[151] Lu X, Zhou L, Chen L, et al. X-ray detection performance of vertical Schottky photodiodes based on a bulk β-Ga_2O_3 substrate grown by an EFG method. ECS J Solid State Sci Technol, 2019, 8, Q3046

[152] Cheng Z, Hanke M, Galazka Z, et al. Thermal expansion of single-crystalline β-Ga_2O_3 from RT to 1200 K studied by synchrotron-based high resolution x-ray diffraction. Appl Phys Lett, 2018, 113, 182102

[153] Katre A, Carrete J, Wang T, et al. Phonon transport unveils the prevalent point defects in GaN. Phys Rev Mater, 2018, 2, 050602

[154] Imura M, Ota Y, Banal R G, Liao M, et al. Effect of boron incorporation on structural and optical properties of AlN layers grown by metalorganic vapor phase epitaxy. Phys Status Solidi A, 2018, 215(21), 1800282

[155] Kojima K, Takashima S, Edo M, et al. Nitrogen vacancies as a common element of the green luminescence and nonradiative recombination centers in Mg-implanted GaN layers formed on a GaN substrate. Appl Phys Express, 2017, 10, 061002

[156] Kamimura J, Bogdanoff P, Ramsteiner M, et al. p-type doping of GaN nanowires characterized by photoelectrochemical measurements. Nano Lett, 2017, 17, 1529

[157] Pavesi M, Manfredi M, Salviati G, et al. Optical evidence of an electrothermal degradation of InGaN-based light-emitting diodes during electrical stress. Appl Phys Lett, 2004, 84, 3403

[158] Reboredo F A, Pantelides S T. Novel defect complexes and their role in the p-type doping of GaN. Phys Rev Lett, 1999, 82, 1887

[159] Miceli G, Pasquarello A. Self-compensation due to point defects in Mg-doped GaN. Phys Rev B, 2016, 93, 165207

[160] Dai Q, Zhang X, Wu Z, et al. Effects of Mg-doping on characteristics of semi-polar $(11\bar{2}2)$ plane p-AlGaN films. Mater Lett, 2017, 209, 472

[161] Pampili P, Parbrook P J. Doping of III-nitride materials. Mater Sci Semicond Process, 2017, 62, 180

[162] Taniyasu Y, Kasu M, Makimoto T. An aluminium nitride light-emitting diode with a wavelength of 210 nanometres. Nature, 2006, 441, 325

[163] Taniyasu Y, Kasu M, Kobayashi N. Intentional control of n-type conduction for Si-doped AlN and $Al_xGa_{1-x}N$ ($0.42 \leqslant x < 1$). Appl Phys Lett, 2002, 81, 1255

[164] Nakarmi M L, Kim K H, Zhu K, et al. Transport properties of highly conductive n-type Alrich $Al_xGa_{1-x}N$ ($x \geqslant 0.7$). Appl Phys Lett, 2004, 85, 3769

[165] Collazo R, Mita S, Xie J, et al. Progress on n-type doping of AlGaN alloys on AlN single crystal substrates for UV optoelectronic applications. Phys Status Solidi C, 2011, 8, 2031

[166] Mehnke F, Wernicke T, Pingel H, et al. Highly conductive n-$Al_xGa_{1-x}N$ layers with aluminum mole fractions above 80%. Appl Phys Lett, 2013, 103, 212109

[167] Nakarmi M L, Nepal N, Ugolini C, et al. Correlation between optical and electrical properties of Mg-doped AlN epilayers. Appl Phys Lett, 2006, 89, 152120

[168] Mireles F, Ulloa S E. Acceptor binding energies in GaN and AlN. Phys Rev B, 1998, 58, 3879

[169] Li J, Oder T N, Nakarmi M L, et al. Optical and electrical properties of Mg-doped p-type $Al_xGa_{1-x}N$. Appl Phys Lett, 2002, 80, 1210

[170] Sarwar A T M G, May B J, Deitz J I, et al. Tunnel junction enhanced nanowire ultraviolet light emitting diodes. Appl Phys Lett, 2015, 107, 101103

[171] Kaneko M, Ueta S, Horita M, et al. Deep-ultraviolet light emission from 4H-AlN/4H-GaN short-period superlattice grown on 4H-SiC$(11\bar{2}0)$. Appl Phys Lett, 2018, 112, 012106

[172] Liu S, Ye C, Cai X, et al. Performance enhancement of AlGaN deep-ultraviolet light-emitting diodes with varied superlattice barrier electron blocking layer. Appl Phys A, 2016, 122, 527

[173] Kozodoy P, Hansen M, DenBaars S P, et al. Enhanced Mg doping efficiency in $Al_{0.2}Ga_{0.8}N$/GaN superlattices. Appl Phys Lett, 1999, 74, 3681

[174] Sun H, Yin J, Pecora E F, et al. Deep-ultraviolet emitting AlGaN multiple quantum well graded-index separate-confinement heterostructures grown by MBE on SiC substrates. IEEE Photon J, 2017, 9, 2201109

[175] Sun H, Pecora E F, Woodward J, et al. Effect of indium in $Al_{0.65}Ga_{0.35}N/Al_{0.8}Ga_{0.2}N$ MQWs for the development of deep-UV laser structures in the form of graded-index separate confinement heterostructure (GRINSCH). Phys Status Solidi A, 2016, 213, 1165

[176] Sun H, Woodward J, Yin J, et al. Development of AlGaN-based graded-index-separate-confinement-heterostructure deep UV emitters by molecular beam epitaxy. J Vac Sci Technol B, 2013, 31, 03C117

[177] Sun H, Moustakas T D. UV emitters based on an AlGaN p-n junction in the form of graded-index separate confinement heterostructure. Appl Phys Express, 2013, 7, 012104

[178] Simon J, Protasenko V, Lian C, et al. Polarization-induced hole doping in wide-band-gap uniaxial semiconductor heterostructures. Science, 2010, 327, 60

[179] Liu C, Ooi Y K, Islam S M, et al. Physics and polarization characteristics of 298 nm AlN-delta-GaN quantum well ultraviolet light-emitting diodes. Appl Phys Lett, 2017, 110, 071103

[180] Nakarmi M L, Kim K H, Li J, et al. Enhanced p-type conduction in GaN and AlGaN by Mg-δ-doping. Appl Phys Lett, 2003, 82, 3041

[181] Gaddy B E, Bryan Z, Bryan I, et al. The role of the carbon-silicon complex in eliminating deep ultraviolet absorption in AlN. Appl Phys Lett, 2014, 104, 202106

[182] Wu H, Zheng R, Liu W, et al. C and Si codoping method for p-

type AlN. J Appl Phys, 2010, 108, 053715
[183] Tran N H, Le B H, Zhao S, et al. On the mechanism of highly efficient p-type conduction of Mg-doped ultra-widebandgap AlN nanostructures. Appl Phys Lett, 2017, 110, 032102
[184] Connie A T, Zhao S, Sadaf S M, et al. Optical and electrical properties of Mg-doped AlN nanowires grown by molecular beam epitaxy. Appl Phys Lett, 2015, 106, 213105
[185] Sedhain A, Al Tahtamouni T M, Li J, et al. Beryllium acceptor binding energy in AlN. Appl Phys Lett, 2008, 93, 141104
[186] Wu R, Shen L, Yang M, et al. Possible efficient p-type doping of AlN using Be: An ab initio study. Appl Phys Lett, 2007, 91, 152110
[187] Szabó Á, Son N T, Janzén E, et al. Group-II acceptors in wurtzite AlN: A screened hybrid density functional study. Appl Phys Lett, 2010, 96, 192110
[188] Soltamov V A, Rabchinskii M K, Yavkin B V, et al. Properties of AlN single crystals doped with Beryllium via high temperature diffusion. Appl Phys Lett, 2018, 113, 082104
[189] Wang Q, Bowen C R, Lewis R, et al. Hexagonal boron nitride nanosheets doped pyroelectric ceramic composite for high-performance thermal energy harvesting. Nano Energy, 2019, 60, 144
[190] Puchta R. A brighter beryllium. Nat Chem, 2011, 3, 416
[191] Park J H, Kim D Y, Schubert E F, et al. Fundamental limitations of wide-bandgap semiconductors for light-emitting diodes. ACS Energy Lett, 2018, 3, 655
[192] Kamiyama S, Iwaya M, Hayashi N, et al. Low-temperature-deposited AlGaN interlayer for improvement of AlGaN/GaN heterostructure. J Cryst Growth, 2001, 223, 83
[193] Islam S M, Lee K, Verma J, et al. MBE-grown 232–270 nm deep-UV LEDs using monolayer thin binary GaN/AlN quantum heterostructures. Appl Phys Lett, 2017, 110, 041108
[194] Wang L Y, Song W D, Hu W X, et al. Efficiency enhancement of ultraviolet light-emitting diodes with segmentally graded p-type AlGaN layer. Chin Phys B, 2019, 28, 018503
[195] Strak P, Kempisty P, Ptasinska M, et al. Principal physical properties of GaN/AlN multiquantum well systems determined by density functional theory calculations. J Appl Phys, 2013, 113, 193706
[196] Long H, Wang S, Dai J, et al. Internal strain induced significant enhancement of deep ultraviolet light extraction efficiency for AlGaN multiple quantum wells grown by MOCVD. Opt Express, 2018, 26, 680
[197] Reich C, Guttmann M, Feneberg M, et al. Strongly transverse-electric-polarized emission from deep ultraviolet AlGaN quantum well light emitting diodes. Appl Phys Lett, 2015, 107, 142101
[198] Verma J, Islam S M, Protasenko V, et al. Tunnel-injection quantum dot deep-ultraviolet light-emitting diodes with polarization-induced doping in III-nitride heterostructures. Appl Phys Lett, 2014, 104, 021105
[199] Verma J, Kandaswamy P K, Protasenko V, et al. Tunnel-injection GaN quantum dot ultraviolet light-emitting diodes. Appl Phys Lett, 2013, 102, 041103
[200] Taniyasu Y, Kasu M. Polarization property of deepultraviolet light emission from C-plane AlN/GaN short-period superlattices. Appl Phys Lett, 2011, 99, 251112
[201] Zhao S, Mi Z. Al(Ga)N nanowire deep ultraviolet optoelectronics. Semicond Semimet, 2017, 96, 167
[202] Beeler M, Hille P, Schormann J, et al. Intraband absorption in self-assembled Ge-doped GaN/AlN nanowire heterostructures. Nano Lett, 2014, 14, 1665
[203] Tchernycheva M, Nevou L, Doyennette L, et al. Systematic experimental and theoretical investigation of intersubband absorption in GaN/AlN quantum wells. Phys Rev B, 2006, 73, 125347
[204] Cociorva D, Aulbur W G, Wilkins J W. Quasiparticle calculations of band offsets at AlN –GaN interfaces. Solid State Commun, 2002, 124, 63
[205] Binggeli N, Ferrara P, Baldereschi A. Band-offset trends in nitride heterojunctions. Phys Rev B, 2001, 63, 245306
[206] Kamiya K, Ebihara Y, Kasu M, . Efficient structure for deep-ultraviolet light-emitting diodes with high emission efficiency: A first-principles study of AlN/GaN superlattice. Jpn J Appl Phys, 2012, 51, 02BJ11
[207] Bayerl D, Islam S M, Jones C M, et al. Deep ultraviolet emission from ultra-thin GaN/AlN heterostructures. Appl Phys Lett, 2016, 109, 241102
[208] Islam S M, Protasenko V, Rouvimov S, et al. Sub-230 nm deep-UV emission from GaN quantum disks in AlN grown by a modified Stranski-Krastanov mode. Jpn J Appl Phys, 2016, 55, 05FF06
[209] Bayerl D, Kioupakis E. Visible-wavelength polarized-light emission with small-diameter InN nanowires. Nano Lett, 2014, 14, 3709
[210] Efros A L, Delehanty J B, Huston A L, et al. Evaluating the potential of using quantum dots for monitoring electrical signals in neurons. Nat Nanotechnol, 2018, 13, 278
[211] Sharma A S, Dhar S. Dependence of strain distribution on In content in InGaN/GaN quantum wires and spherical quantum dots. J Electron Mater, 2018, 47, 1239
[212] Renard J, Kandaswamy P K, Monroy E, et al. Suppression of nonradiative processes in long-lived polar GaN/AlN quantum dots. Appl Phys Lett, 2009, 95, 131903
[213] Janjua B, Sun H, Zhao C, et al. Self-planarized quantum-disks-in-nanowires ultraviolet-B emitters utilizing pendeo-epitaxy. Nanoscale, 2017, 9, 7805
[214] Zhao C, Ng T K, Wei N, et al. Facile formation of high-quality InGaN/GaN quantum-disks-in-nanowires on bulk-metal substrates for high-power light-emitters. Nano Lett, 2016, 16, 1056
[215] Hestroffer K, Leclere C, Cantelli V, et al. *In situ* study of self-assembled GaN nanowires nucleation on Si(111) by plasma-assisted molecular beam epitaxy. Appl Phys Lett, 2012, 100, 212107
[216] Schumann T, Gotschke T, Limbach F, et al. Selective-area catalyst-free MBE growth of GaN nanowires using a patterned oxide layer. Nanotechnology, 2011, 22, 095603
[217] Ravi L, Boopathi K, Panigrahi P, et al. Growth of gallium nitride nanowires on sapphire and silicon by chemical vapor deposition for water splitting applications. Appl Surf Sci, 2018, 449, 213
[218] Fan S, Zhao S, Chowdhury F A, et al. Molecular beam epitaxial growth of III-nitride nanowire heterostructures and emerging device applications. In: Handbook of GaN Semiconductor Materials and Devices. CRC Press, 2017, 265
[219] Heilmann M, Munshi A M, Sarau G, et al. Vertically oriented growth of GaN nanorods on Si using graphene as an atomically thin buffer layer. Nano Lett, 2016, 16, 3524
[220] Zhong Z, Qian F, Wang D, et al. Synthesis of p-type gallium nitride nanowires for electronic and photonic nanodevices. Nano Lett, 2003, 3, 343
[221] Wang R, Nguyen H P T, Connie A T, et al. Color-tunable, phosphor-free InGaN nanowire light-emitting diode arrays monolithically integrated on silicon. Opt Express, 2014, 22, A1768
[222] Parkinson P, Joyce H J, Gao Q, et al. Carrier lifetime and mobility enhancement in nearly defect-free core- shell nanowires measured using time-resolved terahertz spectroscopy. Nano Lett, 2009, 9, 3349
[223] Tham D, Nam C Y, Fischer J E. Defects in GaN nanowires. Adv Funct Mater, 2006, 16, 1197
[224] Le B H, Zhao S, Liu X, et al. Controlled coalescence of AlGaN nanowire arrays: An architecture for nearly dislocation-free planar ultraviolet photonic device applications. Adv Mater, 2016, 28, 8446
[225] Chang Y L, Wang J, Li F, et al. High efficiency green, yellow, and

amber emission from InGaN/GaN dot-in-a-wire heterostructures on Si(111). Appl Phys Lett, 2010, 96, 013106
[226] Yan R, Gargas D, Yang P. Nanowire photonics. Nat Photonics, 2009, 3, 569
[227] Qian F, Gradecak S, Li Y, et al. Core/multishell nanowire heterostructures as multicolor, high-efficiency light-emitting diodes. Nano Lett, 2005, 5, 2287
[228] Qian F, Li Y, Gradecak S, et al. Gallium nitride-based nanowire radial heterostructures for nanophotonics. Nano Lett, 2004, 4, 1975
[229] Priante D, Tangi M, Min J W, et al. Enhanced electro-optic performance of surface-treated nanowires: origin and mechanism of nanoscale current injection for reliable ultraviolet light-emitting diodes. Opt Mater Express, 2019, 9, 203
[230] Almutlaq J, Yin J, Mohammed O F, et al. The benefit and challenges of zero-dimensional perovskites. J Phys Chem Lett, 2018, 9, 4131
[231] Hung N T, Hasdeo E H, Nugraha A R, et al. Quantum effects in the thermoelectric power factor of low-dimensional semiconductors. Phys Rev Lett, 2016, 117, 036602
[232] Li H, Geelhaar L, Riechert H, et al. Computing equilibrium shapes of wurtzite crystals: The example of GaN. Phys Rev Lett, 2015, 115, 085503
[233] Schuster F, Winnerl A, Weiszer S, et al. Doped GaN nanowires on diamond: Structural properties and charge carrier distribution. J Appl Phys, 2015, 117, 044307
[234] Nguyen H P T, Djavid M, Cui K, et al. Temperature-dependent nonradiative recombination processes in GaN-based nanowire white-light-emitting diodes on silicon. Nanotechnology, 2012, 23, 194012
[235] Moustakas T D. Ultraviolet optoelectronic devices based on AlGaN alloys grown by molecular beam epitaxy. MRS Commun, 2016, 6, 247
[236] Liu K, Sun H, AlQatari F, et al. Wurtzite BAlN and BGaN alloys for heterointerface polarization engineering. Appl Phys Lett, 2017, 111, 222106
[237] Li X, Wang S, Liu H, et al. 100-nm thick single-phase wurtzite BAlN films with boron contents over 10%. Phys Status Solidi B, 2017, 254, 1600699
[238] Orsal G, Maloufi N, Gautier S, et al. Effect of boron incorporation on growth behavior of BGaN/GaN by MOVPE. J Cryst Growth, 2008, 310, 5058
[239] Escalanti L, Hart G L W. Boron alloying in GaN. Appl Phys Lett, 2004, 84, 705
[240] Teles L K, Furthmüller J, Scolfaro L M R, et al. Phase separation and gap bowing in zinc-blende InGaN, InAlN, BGaN, and BAlN alloy layers. Physica E, 2002, 13, 1086
[241] Teles L K, Scolfaro L M R, Leite J R, et al. Spinodal decomposition in $B_xGa_{1-x}N$ and $B_xAl_{1-x}N$ alloys. Appl Phys Lett, 2002, 80, 1177
[242] Edgar J H, Smith D T, Eddy C R Jr, et al. c-Boron-aluminum nitride alloys prepared by ion-beam assisted deposition. Thin Solid Films, 1997, 298, 33
[243] Jiang H X, Lin J Y. Hexagonal boron nitride epilayers: Growth, optical properties and device applications. ECS J Solid State Sci Technol, 2017, 6, Q3012
[244] Das T, Chakrabarty S, Kawazoe Y, et al. Tuning the electronic and magnetic properties of graphene/h-BN hetero nanoribbon: A first-principles investigation. AIP Adv, 2018, 8, 065111
[245] Kubota Y, Watanabe K, Tsuda O, et al. Deep ultraviolet light-emitting hexagonal boron nitride synthesized at atmospheric pressure. Science, 2007, 317, 932
[246] Blase X, Rubio A, Louie S G, et al. Quasiparticle band structure of bulk hexagonal boron nitride and related systems. Phys Rev B, 1995, 51, 6868
[247] Rubio A, Corkill J L, Cohen M L. Theory of graphitic boron nitride nanotubes. Phys Rev B, 1994, 49, 5081
[248] Arnaud B, Lebegue S, Rabiller P, et al. Huge excitonic effects in layered hexagonal boron nitride. Phys Rev Lett, 2006, 96, 026402
[249] Hong X, Wang D, Chung D D L. Boron nitride nanotube mat as a low-*k* dielectric material with relative dielectric constant ranging from 1.0 to 1.1. J Electron Mater, 2016, 45, 453
[250] Yin J, Li J, Hang Y, et al. Boron nitride nanostructures: Fabrication, functionalization and applications. Small, 2016, 12, 2942
[251] Shehzad K, Xu Y, Gao C, et al. Three-dimensional macro-structures of two-dimensional nanomaterials. Chem Soc Rev, 2016, 45, 5541
[252] Terao T, Zhi C, Bando Y, et al. Alignment of boron nitride nanotubes in polymeric composite films for thermal conductivity improvement. J Phys Chem C, 2010, 114, 4340
[253] Zhi C, Bando Y, Tang C, et al. Boron nitride nanotubes. Mater Sci Eng R, 2010, 70, 92
[254] Henck H, Pierucci D, Fugallo G, et al. Direct observation of the band structure in bulk hexagonal boron nitride. Phys Rev B, 2017, 95, 085410
[255] Grenadier S J, Maity A, Li J, et al. Origin and roles of oxygen impurities in hexagonal boron nitride epilayers. Appl Phys Lett, 2018, 112, 162103
[256] Du X Z, Li J, Lin J Y, et al. The origins of near band-edge transitions in hexagonal boron nitride epilayers. Appl Phys Lett, 2016, 108, 052106
[257] Attaccalite C, Bockstedte M, Marini A, et al. Coupling of excitons and defect states in boron-nitride nanostructures. Phys Rev B, 2011, 83, 144115
[258] Schué L, Sponza L, Plaud A, et al. Bright luminescence from indirect and strongly bound excitons in h-BN. Phys Rev Lett, 2019, 122, 067401
[259] Watanabe K, Taniguchi T. Jahn-Teller effect on exciton states in hexagonal boron nitride single crystal. Phys Rev B, 2009, 79, 193104
[260] Watanabe K, Taniguchi T, Kanda H. Direct-bandgap properties and evidence for ultraviolet lasing of hexagonal boron nitride single crystal. Nat Mater, 2004, 3, 404
[261] Solozhenko V L, Lazarenko A G, Petitet J P, et al. Bandgap energy of graphite-like hexagonal boron nitride. J Phys Chem Solids, 2001, 62, 1331
[262] Carlisle J A, Shirley E L, Terminello L J, et al. Band-structure and core-hole effects in resonant inelastic softx-ray scattering: Experiment and theory. Phys Rev B, 1999, 59, 7433
[263] Jia J J, Callcott T A, Shirley E L, et al. Resonant inelastic X-ray scattering in hexagonal boron nitride observed by soft-X-ray fluorescence spectroscopy. Phys Rev Lett, 1996, 76, 4054
[264] Taylor C A, Brown S W, Subramaniam V, et al. Observation of near-band-gap luminescence from boron nitride films. Appl Phys Lett, 1994, 65, 1251
[265] Lopatin V V, Konusov F V. Energetic states in the boron nitride band gap. J Phys Chem Solids, 1992, 53, 847
[266] Tarrio C, Schnatterly S E. Interband transitions, plasmons, and dispersion in hexagonal boron nitride. Phys Rev B, 1989, 40, 7852
[267] Hoffman D M, Doll G L, Eklund P C. Optical properties of pyrolytic boron nitride in the energy range 0.05–10 eV. Phys Rev B, 1984, 30, 6051
[268] Sugino T, Tanioka K, Kawasaki S, et al. Characterization and field emission of sulfur-doped boron nitride synthesized by plasma-assisted chemical vapor deposition. Jpn J Appl Phys, 1997, 36, L463
[269] Carpenter L G, Kirby P J. The electrical resistivity of boron nitride over the temperature range 700 °C to 1400 °C. J Phys D, 1982, 15, 1143
[270] Davies B M, Bassani F, Brown F C, et al. Core excitons at the boron *K* edge in hexagonal BN. Phys Rev B, 1981, 24, 3537
[271] Tegeler E, Kosuch N, Wiech G, et al. On the electronic structure of hexagonal boron nitride. Phys Status Solidi B, 1979, 91, 223

[272] Zunger A, Katzir A, Halperin A. Optical properties of hexagonal boron nitride. Phys Rev B, 1976, 13, 5560
[273] Brown F C, Bachrach R Z, Skibowski M. Effect of X-ray polarization at the boron *K* edge in hexagonal BN. Phys Rev B, 1976, 13, 2633
[274] Zupan J, Kolar D. Optical properties of graphite and boron nitride. J Phys C Solid State Phys, 1972, 5, 3097
[275] Cassabois G, Valvin P, Gil B. Hexagonal boron nitride is an indirect bandgap semiconductor. Nat Photonics, 2016, 10, 262
[276] Laleyan D A, Zhao S, Woo S Y, et al. AlN/h-BN heterostructures for Mg dopant-free deep ultraviolet photonics. Nano Lett, 2017, 17, 3738
[277] Cadiz F, Courtade E, Robert C, et al. Excitonic linewidth approaching the homogeneous limit in MoS_2-based van der Waals heterostructures. Phys Rev X, 2017, 7, 021026
[278] Museur L, Brasse G, Pierret A, et al. Exciton optical transitions in a hexagonal boron nitride single crystal. Phys Status Solidi RRL, 2011, 5, 214
[279] Pierucci D, Zribi J, Henck H, et al. Van der Waals epitaxy of two-dimensional single-layer h-BN on graphite by molecular beam epitaxy: Electronic properties and band structure. Appl Phys Lett, 2018, 112, 253102
[280] Schubert E F. Light-emitting diodes. Cambridge University Press, 2006
[281] Kaneko K, Fujita S, Hitora T. A power device material of corundum-structured α-Ga_2O_3 fabricated by MIST EPITAXY® technique. Jpn J Appl Phys, 2018, 57, 02CB18
[282] Fujita S, Oda M, Kaneko K, et al. Evolution of corundum-structured III-oxide semiconductors: Growth, properties, and devices. Jpn J Appl Phys, 2016, 55, 1202A3
[283] Shinohara D, Fujita S. Heteroepitaxy of corundum-structured α-Ga_2O_3 thin films on α-Al_2O_3 substrates by ultrasonic mist chemical vapor deposition. Jpn J Appl Phys, 2008, 47, 7311
[284] Marezio M, Remeika J P. Bond lengths in the α-Ga_2O_3 structure and the high-pressure phase of $Ga_{2-x}Fe_xO_3$. J Chem Phys, 1967, 46, 1862
[285] Leszczynski M, Teisseyre H, Suski T, et al. Lattice parameters of gallium nitride. Appl Phys Lett, 1996, 69, 73
[286] Zhao J, Zhang X, He J, et al. High internal quantum efficiency of nonpolar a-plane AlGaN-based multiple quantum wells grown on r-plane sapphire substrate. ACS Photonics, 2018, 5, 1903
[287] Tangi M, Mishra P, Janjua B, et al. Role of quantumconfined stark effect on bias dependent photoluminescence of N-polar GaN/InGaN multi-quantum disk amber light emitting diodes. J Appl Phys, 2018, 123, 105702
[288] Moustakas T D, Paiella R. Optoelectronic device physics and technology of nitride semiconductors from the UV to the terahertz. Rep Prog Phys, 2017, 80, 106501
[289] Bartoš I, Romanyuk O, Paskova T, et al. Electron band bending and surface sensitivity: X-ray photoelectron spectroscopy of polar GaN surfaces. Surf Sci, 2017, 664, 241
[290] Jang H W, Lee J H, Lee J L. Characterization of band bendings on Ga-face and N-face GaN films grown by metalorganic chemical-vapor deposition. Appl Phys Lett, 2002, 80, 3955
[291] Bhat I. Physical properties of gallium nitride and related III–V nitrides. In: Wide Bandgap Semiconductor Power Devices. Woodhead Publishing, 2019, 43
[292] Yonenaga I, Ohkubo Y, Deura M, et al. Elastic properties of indium nitrides grown on sapphire substrates determined by nano-indentation: In comparison with other nitrides. AIP Adv, 2015, 5, 077131
[293] Yim W M, Paff R J. Thermal expansion of AlN, sapphire, and silicon. J Appl Phys, 1974, 45, 1456
[294] Maruska H P, Tietjen J J. The preparation and properties of vapor-deposited single-crystal-line GaN. Appl Phys Lett, 1969, 15, 327
[295] Wright A. Elastic properties of zinc-blende and wurtzite AlN, GaN, and InN. J Appl Phys, 1997, 82, 2833
[296] Kim K, Lambrecht W R L, Segall B. Elastic constants and related properties of tetrahedrally bonded BN, AlN, GaN, and InN. Phys Rev B, 1996, 53, 16310
[297] Polian A, Grimsditch M, Grzegory I. Elastic constants of gallium nitride. J Appl Phys, 1996, 79, 3343
[298] Thokala R, Chaudhuri J. Calculated elastic constants of wide band gap semiconductor thin films with a hexagonal crystal structure for stress problems. Thin Solid Films, 1995, 266, 189
[299] McNeil L E, Grimsditch M, French R H. Vibrational spectroscopy of aluminum nitride. J Am Ceram Soc, 1993, 76, 1132
[300] Chetverikova I F, Chukichev M V, Rastorguev L N. X-ray phase analysis and elastic properties of gallium nitride. Inorg Mater, 1986, 22, 53
[301] Rounds R, Sarkar B, Sochacki T, et al. Thermal conductivity of GaN single crystals: Influence of impurities incorporated in different growth processes. J Appl Phys, 2018, 124, 105106
[302] Ziade E, Yang J, Brummer G, et al. Thickness dependent thermal conductivity of gallium nitride. Appl Phys Lett, 2017, 110, 031903
[303] Mion C, Muth J F, Preble E A, et al. Accurate dependence of gallium nitride thermal conductivity on dislocation density. Appl Phys Lett, 2006, 89, 092123
[304] Harafuji K, Tsuchiya T, Kawamura K. Molecular dynamics simulation for evaluating melting point of wurtzite-type GaN crystal. J Appl Phys, 2004, 96, 2501
[305] Levinshtein M E, Rumyantsev S L, Shur M S. Properties of Advanced Semiconductor Materials: GaN, AlN, InN, BN, SiC, SiGe. John Wiley & Sons, 2001
[306] Morkoc H, Strite S, Gao G, et al. Large-band-gap SiC, III-V nitride, and II-VI ZnSe-based semiconductor device technologies. J Appl Phys, 1994, 76, 1363
[307] Berger L I. Semiconductor materials. CRC Press, 1997, 123
[308] Grzegory I, Krukowski S, Jun J, et al. Stability of indium nitride at N_2 pressure up to 20 kbar. AIP Conf Proc, 1994, 309, 565
[309] Slack G A, Tanzilli R A, Pohl R O, et al. The intrinsic thermal conductivity of AlN. J Phys Chem Solids, 1987, 48, 641
[310] Barin I, Knacke O, Kubaschewski O. Thermochemical properties of inorganic substances. Springer-Verlag, 1977
[311] Slack G A, McNelly T F. AlN single crystals. J Cryst Growth, 1977, 42, 560
[312] Slack G A, McNelly T F. Growth of high purity AlN crystals. J Cryst Growth, 1976, 34, 263
[313] Slack G A, Bartram S F. Thermal expansion of some diamondlike crystals. J Appl Phys, 1975, 46, 89
[314] Mezaki R, Tilleux E W, Jambois T F,et al. Specific heat of nonmetallic solids. Plenum Press, 1970
[315] Tyagai V A, Evstigneev A M, Krasiko A N, et al. Optical properties of indium nitride films. Sov Phys Semicond, 1977, 11, 1257
[316] Barker A S Jr, Ilegems M. Infrared lattice vibrations and free-electron dispersion in GaN. Phys Rev B, 1973, 7, 743
[317] Wagner J M, Bechstedt F. Properties of strained wurtzite GaN and AlN: *Ab initio* studies. Phys Rev B, 2002, 66, 115202
[318] Krukowski S, Witek A, Adamczyk J, et al. Thermal properties of indium nitride. J Phys Chem Solids, 1998, 59, 289
[319] Doppalapudi D, Moustakas T D. Epitaxial growth and structure of III–V nitride thin films. In: Handbook of Thin Films. Elsevier, 2002, 57
[320] You S T, Lo I, Shih H J, et al. Strain of *m*-plane GaN epitaxial layer grown on β-$LiGaO_2$(100) by plasma-assisted molecular beam epitaxy. AIP Adv, 2018, 8, 075116
[321] Davies M J, Dawson P, Massabuau F C P, et al. The effects of varying threading dislocation density on the optical properties of InGaN/GaN quantum wells. Phys Status Solidi C, 2014, 11, 750
[322] Zhang J P, Wang H M, Gaevski M E, et al. Crack-free thick AlGaN

grown on sapphire using AlN/AlGaN superlattices for strain management. Appl Phys Lett, 2002, 80, 3542

[323] Dong P, Yan J, Wang J, et al. 282-nm AlGaN-based deep ultraviolet light-emitting diodes with improved performance on nano-patterned sapphire substrates. Appl Phys Lett, 2013, 102, 241113

[324] Bryan Z, Bryan I, Xie J, et al. High internal quantum efficiency in AlGaN multiple quantum wells grown on bulk AlN substrates. Appl Phys Lett, 2015, 106, 142107

[325] Grandusky J R, Smart J A, Mendrick M C, et al. Pseudomorphic growth of thick n-type $Al_xGa_{1-x}N$ layers on low-defect-density bulk AlN substrates for UV LED applications. J Cryst Growth, 2009, 311, 2864

[326] Graham D M, Soltani-Vala A, Dawson P, et al. Optical and microstructural studies of InGaN/GaN single-quantum-well structures. J Appl Phys, 2005, 97, 103508

[327] Nakamura S, Senoh M, Mukai T. High-power InGaN/GaN double-heterostructure violet light emitting diodes. Appl Phys Lett, 1993, 62, 2390

[328] Usami S, Ando Y, Tanaka A, et al. Correlation between dislocations and leakage current of p–n diodes on a free-standing GaN substrate. Appl Phys Lett, 2018, 112, 182106

[329] Ferdous M S, Wang X, Fairchild M N, et al. Effect of threading defects on InGaN/GaN multiple quantum well light emitting diodes. Appl Phys Lett, 2007, 91, 231107

[330] Kamiyama S, Iwaya M, Takanami S, et al. UV light-emitting diode fabricated on hetero-ELO-grown $Al_{0.22}Ga_{0.78}N$ with low dislocation density. Phys Status Solidi A, 2002, 192, 296

[331] Nakamura S. The roles of structural imperfections in InGaN-based blue light-emitting diodes and laser diodes. Science, 1998, 281, 956

[332] Massabuau F C, Rhode S L, Horton M K, et al. Dislocations in AlGaN: Core structure, atom segregation, and optical properties. Nano Lett, 2017, 17, 4846

[333] Holec D, Costa P M F J, Kappers M J, et al. Critical thickness calculations for InGaN/GaN. J Cryst Growth, 2007, 303, 314

[334] Holec D, Zhang Y, Rao D V S, et al. Equilibrium critical thickness for misfit dislocations in III-nitrides. J Appl Phys, 2008, 104, 123514

[335] Yang X, Nitta S, Nagamatsu K, et al. Growth of hexagonal boron nitride on sapphire substrate by pulsed-mode metalorganic vapor phase epitaxy. J Cryst Growth, 2018, 482, 1

[336] Creighton J R, Coltrin M E, Figiel J J. Measurement and thermal modeling of sapphire substrate temperature at III –nitride MOVPE conditions. J Cryst Growth, 2017, 464, 132

[337] Hirayama H, Fujikawa S, Noguchi N, et al. 222–282 nm AlGaN and InAlGaN-based deep-UV LEDs fabricated on high-quality AlN on sapphire. Phys Status Solidi A, 2009, 206, 1176

[338] Weeks T W Jr, Bremser M D, Ailey K S, et al. GaN thin films deposited via organometallic vapor phase epitaxy on α(6H)-SiC(0001) using high-temperature monocrystalline AlN buffer layers. Appl Phys Lett, 1995, 67, 401

[339] Akasaki I, Amano H, Koide Y, et al. Effects of AlN buffer layer on crystallographic structure and on electrical and optical properties of GaN and $Ga_{1-x}Al_xN$ ($0 < x \leqslant 0.4$) films grown on sapphire substrate by MOVPE. J Cryst Growth, 1989, 98, 209

[340] Matta S, Brault J, Ngo T H, et al. Photoluminescence properties of (Al,Ga)N nanostructures grown on $Al_{0.5}Ga_{0.5}N$ (0001). Superlattices Microstruct, 2018, 114, 161

[341] Hirayama H, Fujikawa S, Norimatsu J, et al. Fabrication of a low threading dislocation density ELO-AlN template for application to deep-UV LEDs. Phys Status Solidi C, 2009, 6, S356

[342] Xu Q, Liu B, Zhang S, et al. Structural and optical properties of $Al_xGa_{1-x}N$ ($0.33 \leqslant x \leqslant 0.79$) layers on high-temperature AlN interlayer grown by metal organic chemical vapor deposition. Superlattices Microstruct, 2017, 101, 144

[343] Khan M A, Shatalov M, Maruska H P, et al. III-nitride UV devices. Jpn J Appl Phys, 2005, 44, 7191

[344] Keller S, DenBaars S P. Metalorganic chemical vapor deposition of group III nitrides — a discussion of critical issues. J Cryst Growth, 2003, 248, 479

[345] Wu X H, Fini P, Tarsa E J, et al. Dislocation generation in GaN heteroepitaxy. J Cryst Growth, 1998, 189, 231

[346] Imura M, Nakano K, Fujimoto N, et al. Dislocations in AlN epilayers grown on sapphire substrate by high-temperature metal-organic vapor phase epitaxy. Jpn J Appl Phys, 2007, 46, 1458

[347] Narayanan V, Lorenz K, Kim W, et al. Origins of threading dislocations in GaN epitaxial layers grown on sapphire by metalorganic chemical vapor deposition. Appl Phys Lett, 2001, 78, 1544

[348] Wang H M, Zhang J P, Chen C Q, et al. AlN/AlGaN superlattices as dislocation filter for low-threading-dislocation thick AlGaN layers on sapphire. Appl Phys Lett, 2002, 81, 604

[349] Jiang H, Egawa T, Hao M, et al. Reduction of threading dislocations in AlGaN layers grown on AlN/sapphire templates using high-temperature GaN interlayer. Appl Phys Lett, 2005, 87, 241911

[350] Tersoff J. Dislocations and strain relief in compositionally graded layers. Appl Phys Lett, 1993, 62, 693

[351] Ivanov S V, Nechaev D V, Sitnikova A A, et al. Plasma-assisted molecular beam epitaxy of Al(Ga)N layers and quantum well structures for optically pumped mid-UV lasers on *c*-Al_2O_3. Semicond Sci Technol, 2014, 29, 084008

[352] Cho J, Schubert E F, Kim J K. Efficiency droop in light-emitting diodes: Challenges and countermeasures. Laser Photonics Rev, 2013, 7, 408

[353] Janjua B, Sun H, Zhao C, et al. Droop-free $Al_xGa_{1-x}N/Al_yGa_{1-y}N$ quantum-disks-in-nanowires ultraviolet LED emitting at 337 nm on metal/silicon substrates. Opt Express, 2017, 25, 1381

[354] Kim T, Seong T Y, Kwon O. Investigating the origin of efficiency droop by profiling the voltage across the multi-quantum well of an operating light-emitting diode. Appl Phys Lett, 2016, 108, 231101

[355] Jung E, Hwang G, Chung J, et al. Investigating the origin of efficiency droop by profiling the temperature across the multi-quantum well of an operating light-emitting diode. Appl Phys Lett, 2015, 106, 041114

[356] Verzellesi G, Saguatti D, Meneghini M, et al. Efficiency droop in InGaN/GaN blue light-emitting diodes: Physical mechanisms and remedies. J Appl Phys, 2013, 114, 071101

[357] Kim M H, Schubert M F, Dai Q, et al. Origin of efficiency droop in GaN-based light-emitting diodes. Appl Phys Lett, 2007, 91, 183507

[358] Efremov A A, Bochkareva N, Gorbunov R I, et al. Effect of the joule heating on the quantum efficiency and choice of thermal conditions for high-power blue InGaN/GaN LEDs. Semiconductors, 2006, 40, 605

[359] Yang Y, Cao X A, Yan C. Investigation of the nonthermal mechanism of efficiency rolloff in InGaN light-emitting diodes. IEEE Trans Electron Devices, 2008, 55, 1771

[360] Mukai T, Yamada M, Nakamura S. Characteristics of InGaN-based UV/blue/green/amber/red light-emitting diodes. Jpn J Appl Phys, 1999, 38, 3976

[361] Meng X, Wang L, Hao Z, et al. Study on efficiency droop in InGaN/GaN light-emitting diodes based on differential carrier lifetime analysis. Appl Phys Lett, 2016, 108, 013501

[362] Schubert M F, Xu J, Kim J K, et al. Polarization-matched GaInN/AlGaInN multi-quantum-well light-emitting diodes with reduced efficiency droop. Appl Phys Lett, 2008, 93, 041102

[363] Meyaard D S, Lin G B, Cho J, et al. Identifying the cause of the efficiency droop in GaInN light-emitting diodes by correlating the onset of high injection with the onset of the efficiency droop. Appl Phys Lett, 2013, 102, 251114

[364] Bochkareva N I, Rebane Y T, Shreter Y G. Efficiency droop in GaN LEDs at high current densities: Tunneling leakage currents and incomplete lateral carrier localization in InGaN/GaN quantum wells. Semiconductors, 2014, 48, 1079
[365] Rozhansky I V, Zakheim D A. Analysis of the causes of the decrease in the electroluminescence efficiency of AlGaInN light-emitting-diode heterostructures at high pumping density. Semiconductors, 2006, 40, 839
[366] Piprek J. Efficiency droop in nitride-based light-emitting diodes. Phys Status Solidi A, 2010, 207, 2217
[367] Hai X, Rashid R T, Sadaf S M, et al. Effect of low hole mobility on the efficiency droop of AlGaN nanowire deep ultraviolet light emitting diodes. Appl Phys Lett, 2019, 114, 101104
[368] Frost T, Jahangir S, Stark E, et al. Monolithic electrically injected nanowire array edge-emitting laser on (001) silicon. Nano Lett, 2014, 14, 4535
[369] Iveland J, Martinelli L, Peretti J, et al. Direct measurement of Auger electrons emitted from a semiconductor light-emitting diode under electrical injection: Identification of the dominant mechanism for efficiency droop. Phys Rev Lett, 2013, 110, 177406
[370] Wang L, Jin J, Mi C, et al. A review on experimental measurements for understanding efficiency droop in InGaN-based light-emitting diodes. Materials, 2017, 10, 1233
[371] Yoshida H, Kuwabara M, Yamashita Y, et al. Radiative and nonradiative recombination in an ultraviolet GaN/AlGaN multiple-quantum-well laser diode. Appl Phys Lett, 2010, 96, 211122
[372] Morkoç H. Handbook of nitride semiconductors and devices, materials properties, physics and growth. Vol. 3. John Wiley & Sons, 2009
[373] Hader J, Moloney J V, Pasenow B, et al. On the importance of radiative and Auger losses in GaN-based quantum wells. Appl Phys Lett, 2008, 92, 261103
[374] Delaney K T, Rinke P, Van de Walle C G. Auger recombination rates in nitrides from first principles. Appl Phys Lett, 2009, 94, 191109
[375] Delaney K T, Rinke P, Van de Walle C G. Erratum: "Auger recombination rates in nitrides from first principles" [Appl. Phys. Lett. 94, 191109(2009)]. Appl Phys Lett, 2016, 108, 259901
[376] Guo W, Zhang M, Bhattacharya P, et al. Auger recombination in III-nitride nanowires and its effect on nanowire light-emitting diode characteristics. Nano Lett, 2011, 11, 1434
[377] Liu L, Wang L, Liu N, et al. Investigation of the light emission properties and carrier dynamics in dual-wavelength InGaN/GaN multiple-quantum well light emitting diodes. J Appl Phys, 2012, 112, 083101
[378] Berdahl P. Radiant refrigeration by semiconductor diodes. J Appl Phys, 1985, 58, 1369
[379] David A, Hurni C A, Young N G, et al. Electrical properties of III-Nitride LEDs: Recombination-based injection model and theoretical limits to electrical efficiency and electroluminescent cooling. Appl Phys Lett, 2016, 109, 083501
[380] Kibria M G, Qiao R, Yang W, et al. Atomic-scale origin of long-term stability and high performance of p-GaN nanowire arrays for photocatalytic overall pure water splitting. Adv Mater, 2016, 28, 8388
[381] Yong Y, Jiang H, Li X, et al. The cluster-assembled nanowires based on $M_{12}N_{12}$(M = Al and Ga) clusters as potential gas sensors for CO, NO, and NO_2 detection. Phys Chem Chem Phys, 2016, 18, 21431
[382] Alfaraj N, Muhammed M M, Li K H, et al. Thermodynamic photoinduced disorder in AlGaN nanowires. AIP Adv, 2017, 7, 125113
[383] Alfaraj N, Mitra S, Wu F, et al. Photoinduced entropy of InGaN/GaN p–i–n double-heterostructure nanowires. Appl Phys Lett, 2017, 110, 161110
[384] Wang J B, Johnson S, Ding D, et al. Influence of photon recycling on semiconductor luminescence refrigeration. J Appl Phys, 2006, 100, 043502
[385] Dawson P, Schulz S, Oliver R A, et al. The nature of carrier localisation in polar and nonpolar InGaN/GaN quantum wells. J Appl Phys, 2016, 119, 181505
[386] Badcock T J, Dawson P, Davies M J, et al. Low temperature carrier redistribution dynamics in InGaN/GaN quantum wells. J Appl Phys, 2014, 115, 113505
[387] Li C K, Piccardo M, Lu L S, et al. Localization landscape theory of disorder in semiconductors. III. Application to carrier transport and recombination in light emitting diodes. Phys Rev B, 2017, 95, 144206
[388] Belloeil M, Gayral B, Daudin B. Quantum dot-like behavior of compositional fluctuations in AlGaN nanowires. Nano Lett, 2016, 16, 960
[389] Zhao S, Woo S Y, Bugnet M, Liu X., et al Three-dimensional quantum confinement of charge carriers in self-organized AlGaN nanowires: A viable route to electrically injected deep ultraviolet lasers. Nano Lett, 2015, 15, 7801
[390] Mahajan S. Phase separation and atomic ordering in mixed III nitride layers. Scr Mater, 2014, 75, 1
[391] Li D, Jiang K, Sun X, et al. AlGaN photonics: recent advances in materials and ultraviolet devices. Adv Opt Photonics, 2018, 10, 43
[392] He J, Wang S, Chen J, et al. Localized surface plasmon enhanced deep UV-emitting of AlGaN based multi-quantum wells by Al nanoparticles on SiO_2 dielectric interlayer. Nanotechnology, 2018, 29, 195203
[393] Yoshikawa A, Nagatomi T, Morishita T, et al. High-quality AlN film grown on a nanosized concave-convex surface sapphire substrate by metalorganic vapor phase epitaxy. Appl Phys Lett, 2017, 111, 162102
[394] Jiang K, Sun X, Ben J, et al. The defect evolution in homoepitaxial AlN layers grown by high-temperature metal-organic chemical vapor deposition. Cryst Eng Comm, 2018, 20, 2720
[395] Miyoshi M, Ohta M, Mori T, et al. A comparative study of InGaN/GaN multiple-quantum-well solar sells grown on sapphire and AlN template by metalorganic chemical vapor deposition. Phys Status Solidi A, 2018, 215, 1700323
[396] Yoshida S, Misawa S, Gonda S. Improvements on the electrical and luminescent properties of reactive molecular beam epitaxially grown GaN films by using AlN-coated sapphire substrates. Appl Phys Lett, 1983, 42, 427
[397] Amano H, Sawaki N, Akasaki I, et al. Metalorganic vapor phase epitaxial growth of a high quality GaN film using an AlN buffer layer. Appl Phys Lett, 1986, 48, 353
[398] Nakamura S, Senoh M, Mukai T. P-GaN/N-InGaN/NGaN double-heterostructure blue-light-emitting diodes. Jpn J Appl Phys, 1993, 32, L8
[399] Asif Khan M, Kuznia J N, Olson D T, et al. Microwave performance of a 0.25 μm gate AlGaN/GaN heterostructure field effect transistor. Appl Phys Lett, 1994, 65, 1121
[400] Zhao S, Woo S Y, Sadaf S M, et al. Molecular beam epitaxy growth of Al-rich AlGaN nanowires for deep ultraviolet optoelectronics. APL Mater, 2016, 4, 086115
[401] Himwas C, Den Hertog M, Dang L S, et al. Alloy inhomogeneity and carrier localization in AlGaN sections and AlGaN/AlN nanodisks in nanowires with 240–350 nm emission. Appl Phys Lett, 2014, 105, 241908
[402] Khan A, Balakrishnan K, Katona T. Ultraviolet light-emitting diodes based on group three nitrides. Nat Photonics, 2008, 2, 77
[403] Ristić J, Sánchez-García M, Calleja E, et al. AlGaN nanocolumns grown by molecular beam epitaxy: Optical and structural characterization. Phys Status Solidi A, 2002, 192, 60
[404] Vuong T Q P, Cassabois G, Valvin P, et al. Deep ultraviolet emission in hexagonal boron nitride grown by high-temperature mo-

lecular beam epitaxy. 2D Mater, 2017, 4, 021023
[405] Liu X, Zhao S, Le B H, et al. Molecular beam epitaxial growth and characterization of AlN nanowall deep UV light emitting diodes. Appl Phys Lett, 2017, 111, 101103
[406] SaifAddin B K, Almogbel A, Zollner C, et al. Fabrication technology for high light-extraction ultraviolet thin-film flip-chip (UV TFFC) LEDs grown on SiC. Semicond Sci Technol, 2019, 43, 035007
[407] Alias M S, Janjua B, Zhao C, et al. Enhancing the light-extraction efficiency of AlGaN nanowires ultraviolet light-emitting diode by using nitride/air distributed Bragg reflector nanogratings. IEEE Photonics J, 2017, 9, 4900508
[408] Park J S, Kim J K, Cho J, et al. Review- Group III-nitride-based ultraviolet light-emitting diodes: Ways of increasing external quantum efficiency. ECS J Solid State Sci Technol, 2017, 6, Q42
[409] Kneissl M, Rass J. III-nitride ultraviolet emitters. In: Springer Series in Materials Science. Vol. 227. Springer, 2016
[410] Yamada K, Furusawa Y, Nagai S, et al. Development of underfilling and encapsulation for deep-ultraviolet LEDs. Appl Phys Express, 2015, 8, 012101
[411] Maeda N, Hirayama H. Realization of high-efficiency deep-UV LEDs using transparent p-AlGaN contact layer. Phys Status Solidi C, 2013, 10, 1521
[412] Kim B J, Jung H, Shin J, et al. Enhancement of light extraction efficiency of ultraviolet light emitting diodes by patterning of SiO_2 nanosphere arrays. Thin Solid Films, 2009, 517, 2742
[413] Jo M, Maeda N, Hirayama H. Enhanced light extraction in 260 nm light-emitting diode with a highly transparent pAlGaN layer. Appl Phys Express, 2016, 9, 012102
[414] Kinoshita T, Obata T, Yanagi H, et al. High p-type conduction in high-Al content Mg-doped AlGaN. Appl Phys Lett, 2013, 102, 012105
[415] Kozodoy P, Xing H, DenBaars S P, et al. Heavy doping effects in Mg-doped GaN. J Appl Phys, 2000, 87, 1832
[416] Chen Y, Wu H, Han E, et al. High hole concentration in p-type AlGaN by indium-surfactant-assisted Mg-delta doping. Appl Phys Lett, 2015, 106, 162102
[417] Aoyagi Y, Takeuchi M, Iwai S, et al. High hole carrier concentration realized by alternative co-doping technique in metal organic chemical vapor deposition. Appl Phys Lett, 2011, 99, 112110
[418] Kauser M Z, Osinsky A, Dabiran A M, et al. Enhanced vertical transport in p-type AlGaN/GaN superlattices. Appl Phys Lett, 2004, 85, 5275
[419] Luo W, Liu B, Li Z, et al. Enhanced p-type conduction in AlGaN grown by metal-source flow-rate modulation epitaxy. Appl Phys Lett, 2018, 113, 072107
[420] Detchprohm T, Liu Y S, Mehta K, et al. Sub 250 nm deep-UV AlGaN/AlN distributed Bragg reflectors. Appl Phys Lett, 2017, 110, 011105
[421] Alias M S, Alatawi A A, Chong W K, et al. High reflectivity YDH/SiO_2 distributed Bragg reflector for UV-C wavelength regime. IEEE Photonics J, 2018, 10, 2200508
[422] Majety S, Li J, Cao X K, et al. Epitaxial growth and demonstration of hexagonal BN/AlGaN p–n junctions for deep ultraviolet photonics. Appl Phys Lett, 2012, 100, 061121
[423] Dahal R, Li J, Majety S, et al. Epitaxially grown semiconducting hexagonal boron nitride as a deep ultraviolet photonic material. Appl Phys Lett, 2011, 98, 211110
[424] He B, Zhang W J, Yao Z Q, et al. p-type conduction in beryllium-implanted hexagonal boron nitride films. Appl Phys Lett, 2009, 95, 252106
[425] Nose K, Oba H, Yoshida T. Electric conductivity of boron nitride thin films enhanced by *in situ* doping of zinc. Appl Phys Lett, 2006, 89, 112124
[426] Lu M, Bousetta A, Bensaoula A, et al. Electrical properties of boron nitride thin films grown by neutralized nitrogen ion assisted vapor deposition. Appl Phys Lett, 1996, 68, 622
[427] Nakarmi M L, Kim K H, Khizar M, et al. Electrical and optical properties of Mg-doped $Al_{0.7}Ga_{0.3}N$ alloys. Appl Phys Lett, 2005, 86, 092108
[428] Yan Q, Janotti A, Scheffler M, et al. Origins of optical absorption and emission lines in AlN. Appl Phys Lett, 2014, 105, 111104
[429] Takeuchi M, Ooishi S, Ohtsuka T, et al. Improvement of Al-polar AlN layer quality by three-stage flow-modulation metalorganic chemical vapor deposition. Appl Phys Express, 2008, 1, 021102
[430] Takeuchi M, Shimizu H, Kajitani R, et al. Al- and N-polar AlN layers grown on *c*-plane sapphire substrates by modified flow-modulation MOCVD. J Cryst Growth, 2007, 305, 360
[431] Kikkawa J, Nakamura Y, Fujinoki N, et al. Investigating the origin of intense photoluminescence in Si capping layer on $Ge_{1-x}Sn_x$ nanodots by transmission electron microscopy. J Appl Phys, 2013, 113, 074302
[432] Huang C Y, Wu P Y, Chang K S, et al. High-quality and highly-transparent AlN template on annealed sputter-deposited AlN buffer layer for deep ultraviolet light-emitting diodes. AIP Adv, 2017, 7, 055110
[433] Miyake H, Nishio G, Suzuki S, et al. Annealing of an AlN buffer layer in N_2–CO for growth of a high-quality AlN film on sapphire. Appl Phys Express, 2016, 9, 025501
[434] Miyake H, Lin C H, Tokoro K, et al. Preparation of high-quality AlN on sapphire by high-temperature face-to-face annealing. J Cryst Growth, 2016, 456, 155
[435] Iriarte G F. Influence of the magnetron on the growth of aluminum nitride thin films deposited by reactive sputtering. J Vac Sci Technol, 2010, 28, 193
[436] Ide K, Matsubara Y, Iwaya M, et al. Microstructure analysis of AlGaN on AlN underlying layers with different threading dislocation densities. Jpn J Appl Phys, 2013, 52, 08JE22
[437] Nonaka K, Asai T, Ban K, et al. Microstructural analysis of thick AlGaN epilayers using Mg-doped AlN underlying layer. Phys Status Solidi C, 2011, 8, 1467
[438] Asai T, Nonaka K, Ban K, et al. Growth of low-dislocation-density AlGaN using Mg-doped AlN underlying layer. Phys Status Solidi C, 2010, 7, 2101
[439] Sun H, Wu F, Al Tahtamouni T M, et al. Structural properties, crystal quality and growth modes of MOCVD-grown AlN with TMAl pretreatment of sapphire substrate. J Phys D, 2017, 50, 395101
[440] Hussey L, White R M, Kirste R, et al. Sapphire decomposition and inversion domains in N-polar aluminum nitride. Appl Phys Lett, 2014, 104, 032104
[441] Wong M H, Wu F, Speck J S, et al. Polarity inversion of N-face GaN using an aluminum oxide interlayer. J Appl Phys, 2010, 108, 123710
[442] Lim D H, Xu K, Arima S, et al. Polarity inversion of GaN films by trimethyl-aluminum preflow in low-pressure metalorganic vapor phase epitaxy growth. J Appl Phys, 2002, 91, 6461
[443] Eom D, Kim J, Lee K, et al. Fabrication of AlN nano-structures using polarity control by high temperature metalorganic chemical vapor deposition. J Nanosci Nanotechnol, 2015, 15, 5144
[444] Liu X, Sun C, Xiong B, et al. Aluminum nitride-on-sapphire platform for integrated high-*Q* microresonators. Opt Express, 2017, 25, 587
[445] Lee D, Lee J W, Jang J, et al. Improved performance of AlGaN-based deep ultraviolet light-emitting diodes with nanopatterned AlN/sapphire substrates. Appl Phys Lett, 2017, 110, 191103
[446] Zhou S, Hu H, Liu X, et al. Comparative study of GaN-based ultraviolet LEDs grown on different-sized patterned sapphire substrates with sputtered AlN nucleation layer. Jpn J Appl Phys, 2017, 56, 111001
[447] Wang S, Dai J, Hu J, et al. Ultrahigh degree of optical polarization above 80% in AlGaN-based deep-ultraviolet LED with

moth-eye microstructure. ACS Photonics, 2018, 5, 3534
[448] Shen X Q, Takahashi T, Ide T, et al. High quality thin AlN epilayers grown on Si(110) substrates by metalorganic chemical vapor deposition. CrystEngComm, 2017, 19, 1204
[449] Tran B T, Maeda N, Jo M, et al. Performance improvement of AlN crystal quality grown on patterned Si(111) substrate for deep UV-LED applications. Sci Rep, 2016, 6, 35681
[450] Ooi Y K, Zhang J. Light extraction efficiency analysis of flip-chip ultraviolet light-emitting diodes with patterned sapphire substrate. IEEE Photonics J, 2018, 10, 8200913
[451] Bhattacharyya A, Moustakas T D, Zhou L, et al. Deep ultraviolet emitting AlGaN quantum wells with high internal quantum efficiency. Appl Phys Lett, 2009, 94, 181907
[452] Susilo N, Enslin J, Sulmoni L, et al. Effect of the GaN:Mg contact layer on the light-output and current-voltage characteristic of UVB LEDs. Phys Status Solidi A, 2018, 215, 1700643
[453] Akaike R, Ichikawa S, Funato M, et al. $Al_xGa_{1-x}N$-based semipolar deep ultraviolet light-emitting diodes. Appl Phys Express, 2018, 11, 061001
[454] Liu X, Mashooq K, Szkopek T, et al. Improving the efficiency of transverse magnetic polarized emission from AlGaN based LEDs by using nanowire photonic crystal. IEEE Photonics J, 2018, 10, 4501211
[455] Liu D, Cho S J, Park J, et al. 229 nm UV LEDs on aluminum nitride single crystal substrates using p-type silicon for increased hole injection. Appl Phys Lett, 2018, 112, 081101
[456] Liu C, Ooi Y K, Islam S M, et al. 234 nm and 246 nm AlN-delta-GaN quantum well deep ultraviolet light-emitting diodes. Appl Phys Lett, 2018, 112, 011101
[457] Inoue S i, Tamari N, Taniguchi M. 150 mW deep-ultraviolet light-emitting diodes with large-area AlN nanophotonic light-extraction structure emitting at 265 nm. Appl Phys Lett, 2017, 110, 141106
[458] Sarwar A T M G, May B J, et al. Effect of quantum well shape and width on deep ultraviolet emission in AlGaN nanowire LEDs. Phys Status Solidi A, 2016, 213, 947
[459] Kent T F, Carnevale S D, Sarwar A, et al. Deep ultraviolet emitting polarization induced nanowire light emitting diodes with $Al_xGa_{1-x}N$ active regions. Nanotechnology, 2014, 25, 455201
[460] Moustakas T D, Liao Y, Kao C K, et al. Deep UV-LEDs with high IQE based on AlGaN alloys with strong band structure potential fluctuations. In: Light-Emitting Diodes: Materials, Devices, and Applications for Solid State Lighting XVI. Vol. 8278. 2012, 82780L
[461] Liao Y, Thomidis C, Kao C K. et al AlGaN based deep ultraviolet light emitting diodes with high internal quantum efficiency grown by molecular beam epitaxy. Appl Phys Lett, 2011, 98, 081110
[462] Cabalu J S, Bhattacharyya A, Thomidis C, et al. High power ultraviolet light emitting diodes based on GaN/AlGaN quantum wells produced by molecular beam epitaxy. J Appl Phys, 2006, 100, 104506
[463] Molnar R J, Lei T, Moustakas T D. Electron transport mechanism in gallium nitride. Appl Phys Lett, 1993, 62, 72
[464] Muñoz E, Monroy E, Calle F, et al. AlGaN photodiodes for monitoring solar UV radiation. J Geophys Res Atmos, 2000, 105, 4865
[465] Monroy E, Calle F, Pau J, et al. AlGaN-based UV photodetectors. J Cryst Growth, 2001, 230, 537
[466] Chowdhury U, Wong M M, Collins C J, et al . High-performance solar-blind photodetector using an $Al_{0.6}Ga_{0.4}N$ n-type window layer. J Cryst Growth, 2003, 248, 552
[467] Asgari A, Ahmadi E, Kalafi M. $Al_xGa_{1-x}N$/GaN multi-quantum-well ultraviolet detector based on p-i-n heterostructures. Microelectron J, 2009, 40, 104
[468] Larason T, Ohno Y. Calibration and characterization of UV sensors for water disinfection. Metrologia, 2006, 43, S151
[469] Oubei H M, Shen C, Kammoun A, et al. Light based underwater wireless communications. Jpn J Appl Phys, 2018, 57, 08PA06
[470] Werner M R, Fahrner W R. Review on materials, microsensors, systems and devices for high-temperature and harsh-environment applications. IEEE Trans Ind Electron, 2001, 48, 249
[471] Neuberger R, Müller G, Ambacher O, et al. High-electron-mobility AlGaN/GaN Transistors (HEMTs) for fluid monitoring applications. Phys Status Solidi A, 2001, 185, 85
[472] Miller R A, So H, Chiamori H C, et al. A microfabricated sun sensor using GaN-on-sapphire ultraviolet photodetector arrays. Rev Sci Instrum, 2016, 87, 095003
[473] Alheadary W G, Park K H, Alfaraj N, et al. Free-space optical channel characterization and experimental validation in a coastal environment. Opt Express, 2018, 26, 6614
[474] de Graaf G, Wolffenbuttel R F. Illumination source identification using a CMOS optical microsystem. IEEE Trans Instrum Meas, 2004, 53, 238
[475] Ji M H, Kim J, Detchprohm T, et al. p–i–p–i–n separate absorption and multiplication ultraviolet avalanche photodiodes. IEEE Photonics Technol Lett, 2018, 30, 181
[476] Zheng J, Wang L, Wu X, et al. A PMT-like high gain avalanche photodiode based on GaN/AlN periodically stacked structure. Appl Phys Lett, 2016, 109, 241105
[477] Li J, Fan Z Y, Dahal R, et al. 200 nm deep ultraviolet photodetectors based on AlN. Appl Phys Lett, 2006, 89, 213510
[478] Khan M A, Kuznia J N, Olson D T, et al. High-responsivity photoconductive ultraviolet sensors based on insulating single-crystal GaN epilayers. Appl Phys Lett, 1992, 60, 2917
[479] Tut T, Biyikli N, Kimukin I, et al. High bandwidth-efficiency solar-blind AlGaN Schottky photodiodes with low dark current. Solid-State Electron, 2005, 49, 117
[480] Biyikli N, Kimukin I, Kartaloglu T, et al. High-speed solar-blind AlGaN-based metal-semiconductor- metal photodetectors. Phys Status Solidi C, 2003, 0, 2314
[481] Biyikli N, Aytur O, Kimukin I, et al. Solar-blind AlGaN-based Schottky photodiodes with low noise and high detectivity. Appl Phys Lett, 2002, 81, 3272
[482] Pandit B, Cho J. Metal-semiconductor-metal ultraviolet photodiodes based on reduced graphene oxide/GaN Schottky contacts. Thin Solid Films, 2018, 660, 824
[483] Brendel M, Brunner F, Weyers M. On the EQE-bias characteristics of bottom-illuminated AlGaN-based metal–semiconductor–metal photodetectors with asymmetric electrode geometry. J Appl Phys, 2017, 122, 174501
[484] Brendel M, Helbling M, Knauer A, et al. Top- and bottom-illumination of solar-blind AlGaN metal-semiconductor-metal photodetectors. Phys Status Solidi A, 2015, 212, 1021
[485] Brendel M, Helbling M, Knigge A, et al. Measurement and simulation of top- and bottom-illuminated solar-blind AlGaN metal–semiconductor–metal photodetectors with high external quantum efficiencies. J Appl Phys, 2015, 118, 244504
[486] Butun S, Tut T, Butun B, et al. Deep-ultraviolet $Al_{0.75}Ga_{0.25}N$ photodiodes with low cutoff wavelength. Appl Phys Lett, 2006, 88, 123503
[487] Narita T, Wakejima A, Egawa T. Ultraviolet photodetectors using transparent gate AlGaN/GaN high electron mobility transistor on silicon substrate. Jpn J Appl Phys, 2013, 52, 01AG06
[488] Tut T, Yelboga T, Ulker E, et al. Solar-blind AlGaN-based p–i–n photodetectors with high breakdown voltage and detectivity. Appl Phys Lett, 2008, 92, 103502
[489] Teke A, Dogan S, He L, et al. p-GaN-i-GaN/AlGaN multiple-quantum well n-AlGaN back-illuminated ultraviolet detectors. J Electron Mater, 2003, 32, 307
[490] Collins C J, Chowdhury U, Wong M M, et al. Improved solar-blind detectivity using an $Al_xGa_{1-x}N$ heterojunction p–i–n photodiode. Appl Phys Lett, 2002, 80, 3754
[491] Wong M M, Chowdhury U, Collins C J, et al. High quantum effi-

ciency AlGaN/GaN solar-blind photodetectors grown by metalorganic chemical vapor deposition. Phys Status Solidi A, 2001, 188, 333

[492] Biyikli N, Kimukin I, Kartaloglu T, et al. High-speed solar-blind photodetectors with indium-tin-oxide Schottky contacts. Appl Phys Lett, 2003, 82, 2344

[493] Averin S V, Kuznetzov P I, Zhitov V A, et al. Solar-blind MSM-photodetectors based on $Al_xGa_{1-x}N$ heterostructures. Opt Quant Electron, 2007, 39, 181

[494] Wang G, Xie F, Lu H, et al. Performance comparison of front-and back-illuminated AlGaN-based metal–semiconductor–metal solar-blind ultraviolet photodetectors. J Vac Sci Technol B, 2013, 31, 011202

[495] Høiaas I M, Liudi Mulyo A, Vullum P E, et al. GaN/AlGaN nanocolumn ultraviolet LED using double-layer graphene as substrate and transparent electrode. Nano Lett, 2019, 19, 1649

[496] Fernández-Garrido S, Ramsteiner M, Gao G, et al. Molecular beam epitaxy of GaN nanowires on epitaxial graphene. Nano Lett, 2017, 17, 5213

[497] Tonkikh A A, Tsebro V I, Obraztsova E A, et al. Films of filled single-wall carbon nanotubes as a new material for high-performance air-sustainable transparent conductive electrodes operating in a wide spectral range. Nanoscale, 2019, 11, 6755

[498] Boulanger N, Barbero D R. Nanostructured networks of single wall carbon nanotubes for highly transparent, conductive, and anti-reflective flexible electrodes. Appl Phys Lett, 2013, 103, 021116

[499] Borges B G A L, Holakoei S, das Neves M F F, et al. Molecular orientation and femtosecond charge transfer dynamics in transparent and conductive electrodes based on graphene oxide and PEDOT:PSS composites. Phys Chem Chem Phys, 2019, 21, 736

[500] Yan X, Ma J, Xu H, et al. Fabrication of silver nanowires and metal oxide composite transparent electrodes and their application in UV light-emitting diodes. J Phys D, 2016, 49, 325103

[501] Brendel M, Knigge A, Brunner F, et al. Anisotropic responsivity of AlGaN metal-semiconductor-metal photodetectors on epitaxial laterally overgrown AlN/sapphire templates. J Electron Mater, 2014, 43, 833

[502] Schlegel J, Brendel M, Martens M, et al. Influence of carrier lifetime, transit time, and operation voltages on the photoresponse of visible-blind AlGaN metal–semiconductor–metal photodetectors. Jpn J Appl Phys, 2013, 52, 08JF01

[503] Rathkanthiwar S, Kalra A, Muralidharan R, et al. Analysis of screw dislocation mediated dark current in $Al_{0.50}Ga_{0.50}N$ solar-blind metal-semiconductor-metal photodetectors. J Cryst Growth, 2018, 498, 35

[504] Liu H Y, Wang Y H, Hsu W C. Suppression of dark current on AlGaN/GaN metal-semiconductor-metal photodetectors. IEEE Sens J, 2015, 15, 5202

[505] Li D, Sun X, Song H, et al. Influence of threading dislocations on GaN-based metal –semiconductor –metal ultraviolet photodetectors. Appl Phys Lett, 2011, 98, 011108

[506] Walde S, Brendel M, Zeimer U, et al. Impact of open-core threading dislocations on the performance of AlGaN metal-semiconductor-metal photodetectors. J Appl Phys, 2018, 123, 161551

[507] Yoshikawa A, Ushida S, Nagase K, et al. High-performance solar-blind $Al_{0.6}Ga_{0.4}N/Al_{0.5}Ga_{0.5}N$ MSM type photodetector. Appl Phys Lett, 2017, 111, 191103

[508] Kang S, Nandi R, Kim H, et al. Synthesis of n-AlGaN nanoflowers by MOCVD for high-performance ultraviolet-C photodetectors. J Mater Chem C, 2018, 6, 1176

[509] Cicek E, McClintock R, Vashaei Z, et al. Crack-free AlGaN for solar-blind focal plane arrays through reduced area epitaxy. Appl Phys Lett, 2013, 102, 051102

[510] Cicek E, Vashaei Z, Huang E Kw, et al. $Al_xGa_{1-x}N$-based deep-ultraviolet 320×256 focal plane array. Opt Lett, 2012, 37, 896

[511] Cicek E, McClintock R, Cho C Y, et al. $Al_xGa_{1-x}N$-based back-illuminated solar-blind photodetectors with external quantum efficiency of 89%. Appl Phys Lett, 2013, 103, 191108

[512] Adivarahan V, Simin G, Tamulaitis G, et al. Indium-silicon co-doping of high-aluminum-content AlGaN for solar blind photodetectors. Appl Phys Lett, 2001, 79, 1903

[513] Han W Y, Zhang Z W, Li Z M, et al. High performance back-illuminated MIS structure AlGaN solar-blind ultraviolet photodiodes. J Mater Sci Mater Electron, 2018, 29, 9077

[514] Chen Y, Zhang Z, Jiang H, et al. The optimized growth of AlN templates for back-illuminated AlGaN-based solar-blind ultraviolet photodetectors by MOCVD. J Mater Chem C, 2018, 6, 4936

[515] Albrecht B, Kopta S, John O, et al. Improved AlGaN p–i–n photodetectors for monitoring of ultraviolet radiation. IEEE J Sel Top Quantum Electron, 2014, 20, 3802507

[516] Ozbay E, Biyikli N, Kimukin I, et al. High-performance solar-blind photodetectors based on $Al_xGa_{1-x}N$ heterostructures. IEEE J Sel Top Quantum Electron, 2004, 10, 742

[517] Muhtadi S, Hwang S M, Coleman A L, et al. High-speed solar-blind UV photodetectors using high-Al content $Al_{0.64}Ga_{0.36}N/Al_{0.34}Ga_{0.66}N$ multiple quantum wells. Appl Phys Express, 2017, 10, 011004

[518] Babichev A V, Zhang H, Lavenus P, et al. GaN nanowire ultraviolet photodetector with a graphene transparent contact. Appl Phys Lett, 2013, 103, 201103

[519] Kang S, Chatterjee U, Um D Y, et al. Ultraviolet-C photodetector fabricated using Si-doped n-AlGaN nanorods grown by MOCVD. ACS Photonics, 2017, 4, 2595

[520] Zou Y, Zhang Y, Hu Y, et al. Ultraviolet detectors based on wide bandgap semiconductor nanowire: A review. Sensors, 2018, 18, 2072

[521] Cai Q, Luo W K, Li Q, et al. AlGaN ultraviolet avalanche photodiodes based on a triple-mesa structure. Appl Phys Lett, 2018, 113, 123503

[522] Shao Z G, Chen D J, Lu H, et al. High-gain AlGaN solar-blind avalanche photodiodes. IEEE Electron Device Lett, 2014, 35, 372

[523] Bellotti E, Bertazzi F, Shishehchi S, et al. Theory of carriers transport in III-nitride materials: State of the art and future outlook. IEEE Trans Electron Devices, 2013, 60, 3204

[524] Huang Z, Li J, Zhang W, et al. AlGaN solar-blind avalanche photodiodes with enhanced multiplication gain using back-illuminated structure. Appl Phys Express, 2013, 6, 054101

[525] Huang Y, Chen D J, Lu H, et al. Back-illuminated separate absorption and multiplication AlGaN solar-blind avalanche photodiodes. Appl Phys Lett, 2012, 101, 253516

[526] Sun L, Chen J, Li J, et al. AlGaN solar-blind avalanche photodiodes with high multiplication gain. Appl Phys Lett, 2010, 97, 191103

[527] Dahal R, Al Tahtamouni T M, Lin J Y,et al. AlN avalanche photodetectors. Appl Phys Lett, 2007, 91, 243503

[528] Dahal R, Al Tahtamouni T M, Fan Z Y, et al. Hybrid AlN-SiC deep ultraviolet Schottky barrier photodetectors. Appl Phys Lett, 2007, 90, 263505

[529] McClintock R, Yasan A, Minder K, et al. Avalanche multiplication in AlGaN based solar-blind photodetectors. Appl Phys Lett, 2005, 87, 241123

[530] Nikzad S, Hoenk M, Jewell A, et al. Single photon counting UV solar-blind detectors using silicon and III –nitride materials. Sensors, 2016, 16, 927

[531] Pau J L, McClintock R, Minder K, et al. Geiger-mode operation of back-illuminated GaN avalanche photodiodes. Appl Phys Lett, 2007, 91, 041104

[532] Kim J, Ji M H, Detchprohm T, et al. Comparison of AlGaN p–i–n ultraviolet avalanche photodiodes grown on free-standing GaN and sapphire substrates. Appl Phys Express, 2015, 8, 122202

[533] Wu H, Wu W, Zhang H, et al. All AlGaN epitaxial structure solar-

blind avalanche photodiodes with high efficiency and high gain. Appl Phys Express, 2016, 9, 052103
[534] Hahn L, Fuchs F, Kirste L, et al. Avalanche multiplication in AlGaN-based heterostructures for the ultraviolet spectral range. Appl Phys Lett, 2018, 112, 151102
[535] Shao Z, Chen D, Liu Y, et al. Significant performance improvement in AlGaN solar-blind avalanche photodiodes by exploiting the built-in polarization electric field. IEEE J Sel Top Quantum Electron, 2014, 20, 3803306
[536] Walker D, Kumar V, Mi K, et al. Solar-blind AlGaN photodiodes with very low cutoff wavelength. Appl Phys Lett, 2000, 76, 403
[537] Gökkavas M, Butun S, Tut T, et al. AlGaN-based high-performance metal-semiconductor-metal photodetectors. Photonics Nanostruct: Fundam Appl, 2007, 5, 53
[538] Izyumskaya N, Demchenko D O, Das S, et al. Recent development of boron nitride towards electronic applications. Adv Electron Mater, 2017, 3, 1600485
[539] Monroy E, Omnès F, Calle F. Wide-bandgap semiconductor ultraviolet photodetectors. Semicond Sci Technol, 2003, 18, R33
[540] Munoz E, Monroy E, Pau J, et al. III nitrides and UV detection. J Phys Condens Matter, 2001, 13, 7115
[541] Rodak L, Sampath A, Gallinat C, et al. Solar-blind $Al_xGa_{1-x}N$/AlN/SiC photodiodes with a polarization-induced electron filter. Appl Phys Lett, 2013, 103, 071110
[542] Spies M, Den Hertog M I, Hille P, et al. Bias-controlled spectral response in GaN/AlN single-nanowire ultraviolet photodetectors. Nano Lett, 2017, 17, 4231
[543] Nikishin S, Borisov B, Pandikunta M, et al. High quality AlN for deep UV photodetectors. Appl Phys Lett, 2009, 95, 054101
[544] Barkad H A, Soltani A, Mattalah M, et al. Design, fabrication and physical analysis of TiN/AlN deep UV photodiodes. J Phys D, 2010, 43, 465104
[545] Laksana C P, Chen M R, Liang Y, et al. Deep-UV sensors based on SAW oscillators using low-temperature-grown AlN films on sapphires. IEEE Trans Ultrason Ferroelectr Freq Control, 2011, 58, 1688
[546] Soltani A, Barkad H, Mattalah M, et al. 193 nm deep-ultraviolet solar-blind cubic boron nitride based photodetectors. Appl Phys Lett, 2008, 92, 053501
[547] Li J, Majety S, Dahal R, et al. Dielectric strength, optical absorption, and deep ultraviolet detectors of hexagonal boron nitride epilayers. Appl Phys Lett, 2012, 101, 171112
[548] Yang N, Zeng X, Lu J, et al. Effect of chemical functionalization on the thermal conductivity of 2D hexagonal boron nitride. Appl Phys Lett, 2018, 113, 171904
[549] Sajjad M, Jadwisienczak W M, Feng P. Nanoscale structure study of boron nitride nanosheets and development of a deep-UV photo-detector. Nanoscale, 2014, 6, 4577
[550] Liu H, Meng J, Zhang X, et al. High-performance deep ultraviolet photodetectors based on few-layer hexagonal boron nitride. Nanoscale, 2018, 10, 5559
[551] Alfaraj N, Li K H, Kang C H, et al. Electrical characterization of solar-blind deep-ultraviolet $(Al_{0.28}Ga_{0.72})_2O_3$ Schottky photodetectors grown on silicon by pulsed laser deposition. Conference on Lasers and Electro–Optics, 2019
[552] Tian H, Liu Q, Hu A, et al. Hybrid graphene/GaN ultraviolet photo-transistors with high responsivity and speed. Opt Express, 2018, 26, 5408
[553] Tian H, Liu Q, Zhou C, et al. Hybrid graphene/unintentionally doped GaN ultraviolet photodetector with high responsivity and speed. Appl Phys Lett, 2018, 113, 121109
[554] Seo T H, Lee K J, Park A H, et al. Enhanced light output power of near UV light emitting diodes with graphene/indium tin oxide nanodot nodes for transparent and current spreading electrode. Opt Express, 2011, 19, 23111
[555] Li K H, Alfaraj N, Kang C H, et al. Deep-ultraviolet β-Ga_2O_3 photodetectors grown on MgO substrates with a TiN template. 2019 IEEE Photonics Conference (IPC), San Antonio, TX, United States, 2019
[556] Qian L X, Liu H Y, Zhang H F, et al. Simultaneously improved sensitivity and response speed of β-Ga_2O_3 solar-blind photodetector via localized tuning of oxygen deficiency. Appl Phys Lett, 2019, 114, 113506
[557] Xu Y, An Z, Zhang L, et al. Solar blind deep ultraviolet β-Ga_2O_3 photodetectors grown on sapphire by the Mist-CVD method. Opt Mater Express, 2018, 8, 2941
[558] Rathkanthiwar S, Kalra A, Solanke S V, et al. Gain mechanism and carrier transport in high responsivity AlGaN-based solar blind metal semiconductor metal photodetectors. J Appl Phys, 2017, 121, 164502
[559] Zhuo R, Zeng L, Yuan H, et al. *In-situ* fabrication of $PtSe_2$/GaN heterojunction for self-powered deep ultraviolet photodetector with ultrahigh current on/off ratio and detectivity. Nano Res, 2019, 12, 183
[560] Zhuo R, Wang Y, Wu D, et al. High-performance self-powered deep ultraviolet photodetector based on MoS_2/GaN p-n heterojunction. J Mater Chem C, 2018, 6, 299
[561] He T, Zhao Y, Zhang X, et al. Solar-blind ultraviolet photodetector based on graphene/vertical Ga_2O_3 nanowire array heterojunction. Nanophotonics, 2018, 7, 1557
[562] Lin R, Zheng W, Zhang D, et al. High-performance graphene/β-Ga_2O_3 heterojunction deep-ultraviolet photodetector with hot-electron excited carrier multiplication. ACS Appl Mater Interfaces, 2018, 10, 22419
[563] Lu Y, Wu Z, Xu W, et al. ZnO quantum dot-doped graphene/h-BN/GaN-heterostructure ultraviolet photodetector with extremely high responsivity. Nanotechnology, 2016, 27, 48LT03
[564] Ai M, Guo D, Qu Y, et al. Fast-response solar-blind ultraviolet photodetector with a graphene/β-Ga_2O_3/graphene hybrid structure. J Alloys Compd, 2017, 692, 634
[565] Kumar M, Jeong H, Polat K, et al. Fabrication and characterization of graphene/AlGaN/GaN ultraviolet Schottky photodetector. J Phys D , 2016, 49, 275105
[566] Martens M, Mehnke F, Kuhn C, et al. Performance characteristics of UV-C AlGaN-based lasers grown on sapphire and bulk AlN substrates. IEEE Photonics Technol Lett, 2014, 26, 342
[567] Xie J, Mita S, Bryan Z, et al. Lasing and longitudinal cavity modes in photo-pumped deep ultraviolet AlGaN heterostructures. Appl Phys Lett, 2013, 102, 171102
[568] Wunderer T, Chua C, Northrup J, et al. Optically pumped UV lasers grown on bulk AlN substrates. Phys Status Solidi C, 2012, 9, 822
[569] Jmerik V N, Mizerov A M, Shubina T V, et al. Optically pumped lasing at 300.4 nm in AlGaN MQW structures grown by plasmaassisted molecular beam epitaxy on c-Al_2O_3. Phys Status Solidi A, 2010, 207, 1313
[570] Takano T, Narita Y, Horiuchi A, et al. Room-temperature deep-ultraviolet lasing at 241.5 nm of AlGaN multiple-quantum-well laser. Appl Phys Lett, 2004, 84, 3567
[571] Martens M, Kuhn C, Simoneit T, et al. The effects of magnesium doping on the modal loss in AlGaN-based deep UV lasers. Appl Phys Lett, 2017, 110, 081103
[572] Pecora E F, Sun H, Dal Negro L, et al. Deep-UV optical gain in AlGaN-based graded-index separate confinement heterostructure. Opt Mater Express, 2015, 5, 809
[573] Zhu H, Shan C X, Li B H, et al. Low-threshold electrically pumped ultraviolet laser diode. J Mater Chem, 2011, 21, 2848
[574] Yoshida H, Yamashita Y, Kuwabara M, et al. A 342-nm ultraviolet AlGaN multiple-quantum-well laser diode. Nat Photonics, 2008, 2, 551
[575] Sellés J, Brimont C, Cassabois G, et al. Deep-UV nitride-on-silicon microdisk lasers. Sci Rep, 2016, 6, 21650

[576] Zhao S, Mi Z. AlGaN nanowires: Path to electrically injected semiconductor deep ultraviolet lasers. IEEE J Quantum Electron, 2018, 54, 2001009
[577] Zhao S, Liu X, Wu Y, et al. An electrically pumped 239 nm AlGaN nanowire laser operating at room temperature. Appl Phys Lett, 2016, 109, 191106
[578] Zhao S, Liu X, Woo S, et al. An electrically injected AlGaN nanowire laser operating in the ultraviolet-C band. Appl Phys Lett, 2015, 107, 043101
[579] Pan R, Retzer U, Werblinski T, et al. Generation of high-energy, kilohertz-rate narrowband tunable ultraviolet pulses using a burst-mode dye laser system. Opt Lett, 2018, 43, 1191
[580] Higase Y, Morita S, Fujii T, et al. High-gain and wide-band optical amplifications induced by a coupled excited state of organic dye molecules co-doped in polymer waveguide. Opt Lett, 2018, 43, 1714
[581] Yamamoto H, Oyamada T, Sasabe H, et al. Amplified spontaneous emission under optical pumping from an organic semiconductor laser structure equipped with transparent carrier injection electrodes. Appl Phys Lett, 2004, 84, 1401
[582] Tsutsumi N, Kawahira T, Sakai W. Amplified spontaneous emission and distributed feedback lasing from a conjugated compound in various polymer matrices. Appl Phys Lett, 2003, 83, 2533
[583] Kogelnik H, Shank C V. Stimulated emission in a periodic structure. Appl Phys Lett, 1971, 18, 152
[584] Lochner Z, Kao T T, Liu Y S, et al. Deep-ultraviolet lasing at 243 nm from photo-pumped AlGaN/AlN heterostructure on AlN substrate. Appl Phys Lett, 2013, 102, 101110
[585] Kao T T, Liu Y S, Satter M M, et al. Sub-250 nm low-threshold deep-ultraviolet AlGaN-based heterostructure laser employing HfO_2/SiO_2 dielectric mirrors. Appl Phys Lett, 2013, 103, 211103
[586] Shatalov M, Gaevski M, Adivarahan V, et al. Room-temperature stimulated emission from AlN at 214 nm. J Appl Phys, 2006, 45, L1286
[587] Klein T, Klembt S, Kozlovsky V, et al. High-power green and blue electron-beam pumped surface-emitting lasers using dielectric and epitaxial distributed Bragg reflectors. J Appl Phys, 2015, 117, 113106
[588] Oto T, Banal R G, Kataoka K, et al. 100 mW deep-ultraviolet emission from aluminium-nitride-based quantum wells pumped by an electron beam. Nat Photonics, 2010, 4, 767
[589] Demir I, Li H, Robin Y, et al. Sandwich method to grow high quality AlN by MOCVD. J Phys D, 2018, 51, 085104
[590] Tran B T, Hirayama H, Jo M, et al. High-quality AlN template grown on a patterned Si(111) substrate. J Cryst Growth, 2017, 468, 225
[591] Kataoka K, Funato M, Kawakami Y. Development of polychromatic ultraviolet light-emitting diodes based on three-dimensional AlGaN quantum wells. Appl Phys Express, 2017, 10, 121001
[592] Kataoka K, Funato M, Kawakami Y. Deep-ultraviolet polychromatic emission from three-dimensionally structured AlGaN quantum wells. Appl Phys Express, 2017, 10, 031001
[593] Funato M, Hayashi K, Ueda M, et al. Emission color tunable light-emitting diodes composed of InGaN multifacet quantum wells. Appl Phys Lett, 2008, 93, 021126
[594] Kaneda M, Pernot C, Nagasawa Y, et al. Uneven AlGaN multiple quantum well for deep-ultraviolet LEDs grown on macrosteps and impact on electroluminescence spectral output. Jpn J Appl Phys, 2017, 56, 061002
[595] Pernot C, Fukahori S, Inazu T, et al. Development of high efficiency 255–355 nm AlGaN-based light-emitting diodes. Phys Status Solidi A, 2011, 208, 1594
[596] Pernot C, Kim M, Fukahori S, et al. Improved efficiency of 255–280 nm AlGaN-based light-emitting diodes. Appl Phys Express, 2010, 3, 061004
[597] Nagamatsu K, Okada N, Sugimura H, et al. High-efficiency AlGaN-based UV light-emitting diode on laterally overgrown AlN. J Cryst Growth, 2008, 310, 2326
[598] Harada T, Oda Y, Motohisa J, et al. Novel nanofaceting structures grown on patterned vicinal (110) GaAs substrates by metal-organic vapor phase epitaxy (MOVPE). Jpn J Appl Phys, 2000, 39, 7090
[599] Oda Y, Fukui T. Natural formation of multiatomic steps on patterned vicinal substrates by MOVPE and application to GaAs QWR structures. J Cryst Growth, 1998, 195, 6
[600] Susilo N, Hagedorn S, Jaeger D, et al. AlGaN-based deep UV LEDs grown on sputtered and high temperature annealed AlN/sapphire. Appl Phys Lett, 2018, 112, 041110
[601] He C, Zhao W, Wu H, et al. High-quality AlN film grown on sputtered AlN/sapphire via growth-mode modification. Cryst Growth Des, 2018, 18, 6816
[602] Xiao S, Suzuki R, Miyake H, et al. Improvement mechanism of sputtered AlN films by high-temperature annealing. J Cryst Growth, 2018, 502, 41
[603] Zhao L, Yang K, Ai Y, et al. Crystal quality improvement of sputtered AlN film on sapphire substrate by high-temperature annealing. J Mater Sci Mater Electron, 2018, 29, 13766
[604] Ben J, Sun X, Jia Y, et al. Defect evolution in AlN templates on PVD-AlN/sapphire substrates by thermal annealing. Cryst Eng Comm, 2018, 20, 4623
[605] Zhao L, Zhang S, Zhang Y, et al. AlGaN-based ultraviolet light-emitting diodes on sputter-deposited AlN templates with epitaxial AlN/AlGaN superlattices. Superlattices Microstruct, 2018, 113, 713
[606] Oh J T, Moon Y T, Kang D S, et al. High efficiency ultraviolet GaN-based vertical light emitting diodes on 6-inch sapphire substrate using *ex-situ* sputtered AlN nucleation layer. Opt Express, 2018, 26, 5111
[607] He C, Zhao W, Zhang K, et al. High-quality GaN epilayers achieved by facet-controlled epitaxial lateral overgrowth on sputtered AlN/PSS templates. ACS Appl Mater Interfaces, 2017, 9, 43386
[608] Chen Z, Zhang J, Xu S, et al. Influence of stacking faults on the quality of GaN films grown on sapphire substrate using a sputtered AlN nucleation layer. Mater Res Bull, 2017, 89, 193
[609] Chen Z, Zhang J, Xu S, et al. Effect of AlN interlayer on the impurity incorporation of GaN film grown on sputtered AlN. J Alloys Compd, 2017, 710, 756
[610] Zhang L, Xu F, Wang M, et al. High-quality AlN epitaxy on sapphire substrates with sputtered buffer layers. Superlattices Microstruct, 2017, 105, 34
[611] Yoshizawa R, Miyake H, Hiramatsu K. Effect of thermal annealing on AlN films grown on sputtered AlN templates by metalorganic vapor phase epitaxy. Jpn J Appl Phys, 2017, 57, 01AD05
[612] Funato M, Shibaoka M, Kawakami Y. Heteroepitaxy mechanisms of AlN on nitridated *c*-and *a*-plane sapphire substrates. J Appl Phys, 2017, 121, 085304
[613] Okada N, Kato N, Sato S, et al. Growth of high-quality and crack free AlN layers on sapphire substrate by multi-growth mode modification. J Cryst Growth, 2007, 298, 349
[614] Chang H, Chen Z, Li W, et al. Graphene-assisted quasi-van der Waals epitaxy of AlN film for ultraviolet light emitting diodes on nano-patterned sapphire substrate. Appl Phys Lett, 2019, 114, 091107
[615] Zhang L, Li X, Shao Y, Yu J, et al. Improving the quality of GaN crystals by using graphene or hexagonal boron nitride nanosheets substrate. ACS Appl Mater Interfaces, 2015, 7, 4504
[616] Kim J, Bayram C, Park H, et al. Principle of direct van der Waals epitaxy of single-crystalline films on epitaxial graphene. Nat Commun, 2014, 5, 4836
[617] Han N, Cuong T V, Han M, et al. Improved heat dissipation in galli-

um nitride light-emitting diodes with embedded graphene oxide pattern. Nat Commun, 2013, 4, 1452
[618] Roy R, Hill V G, Osborn E F. Polymorphism of Ga_2O_3 and the system Ga_2O_3–H_2O. J Am Chem Soc, 1952, 74, 719
[619] Han S H, Mauze A, Ahmadi E, et al. n-type dopants in (001) β-Ga_2O_3 grown on (001) β-Ga_2O_3 substrates by plasma-assisted molecular beam epitaxy. Semicond Sci Technol, 2018, 33, 045001
[620] Sasaki K, Kuramata A, Masui T, et al. Device-quality β-Ga_2O_3 epitaxial films fabricated by ozone molecular beam epitaxy. Appl Phys Express, 2012, 5, 035502
[621] Shimamura K, Víllora E G, Domen K, et al. Epitaxial growth of GaN on (100) β-Ga_2O_3 substrates by metalorganic vapor phase epitaxy. Jpn J Appl Phys, 2005, 44, L7
[622] Víllora E G, Shimamura K, Aoki K, et al. Molecular beam epitaxy of *c*-plane wurtzite GaN on nitridized *a*-plane β-Ga_2O_3. Thin Solid Films, 2006, 500, 209
[623] Ohira S, Suzuki N, Minami H, et al. Growth of hexagonal GaN films on the nitridated β-Ga_2O_3 substrates using RF-MBE. Phys Status Solidi C, 2007, 4, 2306
[624] Kachel K, Korytov M, Gogova D, et al. A new approach to free-standing GaN using β-Ga_2O_3 as a substrate. Cryst Eng Comm, 2012, 14, 8536
[625] Ito S, Takeda K, Nagata K, et al. Growth of GaN and AlGaN on (100) β-Ga_2O_3 substrates. Phys Status Solidi C, 2012, 9, 519
[626] Ajia I A, Yamashita Y, Lorenz K, et al. GaN/AlGaN multiple quantum wells grown on transparent and conductive (-201)-oriented β-Ga_2O_3 substrate for UV vertical light emitting devices. Appl Phys Lett, 2018, 113, 082102
[627] Yamada K, Nagasawa Y, Nagai S, et al. Study on the main-chain structure of amorphous fluorine resins for encapsulating AlGaN-based DUV-LEDs. Phys Status Solidi A, 2018, 215, 1700525
[628] Nagai S, Yamada K, Hirano A, et al. Development of highly durable deep-ultraviolet AlGaN-based LED multichip array with hemispherical encapsulated structures using a selected resin through a detailed feasibility study. Jpn J Appl Phys, 2016, 55, 082101
[629] Liang R, Dai J, Xu L, et al. Interface anchored effect on improving working stability of deep ultraviolet light-emitting diode using graphene oxide-based fluoropolymer encapsulant. ACS Appl Mater Interfaces, 2018, 10, 8238
[630] Shen K C, Ku C T, Hsieh C, et al. Deep-ultraviolet hyperbolic metacavity laser. Adv Mater, 2018, 30, 1706918
[631] Shen K C, Hsieh C, Cheng Y J, et al. Giant enhancement of emission efficiency and light directivity by using hyperbolic metacavity on deep-ultraviolet AlGaN emitter. Nano Energy, 2018, 45, 353
[632] Tangi M, Mishra P, Tseng C C, et al. Band alignment at GaN/single-layer WSe_2 interface. ACS Appl Mater Interfaces, 2017, 9, 9110
[633] Mishra P, Tangi M, Ng T K, et al. Impact of N-plasma and Ga-irradiation on MoS_2 layer in molecular beam epitaxy. Appl Phys Lett, 2017, 110, 012101
[634] Zhao C, Ng T K, Tseng C C, et al. InGaN/GaN nanowires epitaxy on large-area MoS_2 for high-performance light-emitters. RSC Adv, 2017, 7, 26665
[635] Tangi M, Mishra P, Li M Y, et al. Type-I band alignment at MoS_2/$In_{0.15}Al_{0.85}N$ lattice matched heterojunction and realization of MoS_2 quantum well. Appl Phys Lett, 2017, 111, 092104
[636] Tangi M, Mishra P, Ng T K, et al. Determination of band offsets at GaN/single-layer MoS_2 heterojunction. Appl Phys Lett, 2016, 109, 032104
[637] Gupta P, Rahman A, Subramanian S, et al. Layered transition metal dichalcogenides: Promising near-lattice-matched substrates for GaN growth. Sci Rep, 2016, 6, 23708
[638] Lopez-Sanchez O, Lembke D, Kayci M, et al. Ultrasensitive photodetectors based on monolayer MoS_2. Nat Nanotech, 2013, 8, 497
[639] Yin Z, Li H, Li H, Jiang L, et al. Single-layer MoS_2 phototransistors. ACS Nano, 2011, 6, 74
[640] Saigal N, Wielert I, Čapeta D, et al. Effect of lithium doping on the optical properties of monolayer MoS_2. Appl Phys Lett, 2018, 112, 121902
[641] Splendiani A, Sun L, Zhang Y, et al. Emerging photoluminescence in monolayer MoS_2. Nano Lett, 2010, 10, 1271
[642] Mak K F, Lee C, Hone J, et al. Atomically thin MoS_2: A new direct-gap semiconductor. Phys Rev Lett, 2010, 105, 136805
[643] Bharathi N D, Sivasankaran K. Research progress and challenges of two dimensional MoS_2 field effect transistors. J Semicond, 2018, 39, 104002
[644] Pak Y, Kim Y, Lim N, et al. Scalable integration of periodically aligned 2D-MoS_2 nanoribbon array. APL Mater, 2018, 6, 076102
[645] Huang C Y, Chang C, Lu G Z, et al. Hybrid 2D/3D MoS_2/GaN heterostructures for dual functional photoresponse. Appl Phys Lett, 2018, 112, 233106
[646] Grisafe B, Zhao R, Ghosh R K, et al. Electrically triggered insulator-to-metal phase transition in two-dimensional (2D) heterostructures. Appl Phys Lett, 2018, 113, 142101
[647] Ahmad M, Varandani D, Mehta B R. Large surface charge accumulation in 2D MoS_2/Sb_2Te_3 junction and its effect on junction properties: KPFM based study. Appl Phys Lett, 2018, 113, 141603
[648] Roy K, Padmanabhan M, Goswami S, et al. Graphene-MoS_2 hybrid structures for multifunctional photoresponsive memory devices. Nat Nanotech, 2013, 8, 826
[649] Wang Q H, Kalantar-Zadeh K, Kis A, et al. Electronics and optoelectronics of two-dimensional transition metal dichalcogenides. Nat Nanotech, 2012, 7, 699
[650] Wang L, Jie J, Shao Z, et al. MoS_2/Si heterojunction with vertically standing layered structure for ultrafast, high-detectivity, self-driven visible-near infrared photodetectors. Adv Funct Mater, 2015, 25, 2910
[651] Zhao C, Ng T K, ElAfandy R T, et al. Droop-free, reliable, and high-power InGaN/GaN nanowire light-emitting diodes for monolithic metal-optoelectronics. Nano Lett, 2016, 16, 4616
[652] Li L, Zhang Y, Xu S, et al. On the hole injection for III-nitride based deep ultraviolet light-emitting diodes. Materials, 2017, 10, 1221
[653] Tangi M, Kuyyalil J, Shivaprasad S M. Optical bandgap and near surface band bending in degenerate InN films grown by molecular beam epitaxy. J Appl Phys, 2013, 114, 153501
[654] Kuyyalil J, Tangi M, Shivaprasad S. Effect of interfacial lattice mismatch on bulk carrier concentration and band gap of InN. J Appl Phys, 2012, 112, 083521
[655] Roul B, Kumar M, Rajpalke M K, et al. Binary group III-nitride based heterostructures: band offsets and transport properties. J Phys D, 2015, 48, 423001
[656] Zubair A, Nourbakhsh A, Hong J Y, et al. Hot electron transistor with van der Waals base-collector heterojunction and high-performance GaN emitter. Nano Lett, 2017, 17, 3089
[657] Liu J, Kobayashi A, Toyoda S, et al. Band offsets of polar and nonpolar GaN/ZnO heterostructures determined by synchrotron radiation photoemission spectroscopy. Phys Status Solidi B, 2011, 248, 956
[658] King P D C, Veal T D, Kendrick C E, et al. InN/GaN valence band offset: High-resolution X-ray photoemission spectroscopy measurements. Phys Rev B, 2008, 78, 033308
[659] King P D C, Veal T D, Jefferson P H, et al. Valence band offset of InN/AlN heterojunctions measured by X-ray photoelectron spectroscopy. Appl Phys Lett, 2007, 90, 132105
[660] Martin G, Botchkarev A, Rockett A, et al. Valence-band discontinuities of wurtzite GaN, AlN, and InN heterojunctions measured by X-ray photoemission spectroscopy. Appl Phys Lett, 1996, 68, 2541

[661] Mietze C, Landmann M, Rauls E, et al. Band offsets in cubic GaN/AlN superlattices. Phys Rev B, 2011, 83, 195301
[662] Sang L, Zhu Q S, Yang S Y, et al. Band offsets of non-polar A-plane GaN/AlN and AlN/GaN heterostructures measured by X-ray photoemission spectroscopy. Nanoscale Res Lett, 2014, 9, 470
[663] Zhao G, Li H, Wang L, et al. Measurement of semi-polar (11-22) plane AlN/GaN heterojunction band offsets by X-ray photoelectron spectroscopy. Appl Phys A, 2018, 124, 130
[664] Mahmood Z H, Shah A P, Kadir A, et al. Determination of InN-GaN heterostructure band offsets from internal photoemission measurements. Appl Phys Lett, 2007, 91, 152108
[665] Wu C L, Lee H M, Kuo C T, et al. Polarization-induced valence-band alignments at cation- and anion-polar InN/GaN heterojunctions. Appl Phys Lett, 2007, 91, 042112
[666] Shih C F, Chen N C, Chang P H, et al. Band offsets of InN/GaN interface. Jpn J Appl Phys, 2005, 44, 7892
[667] Wang K, Lian C, Su N, et al. Conduction band offset at the InN/GaN heterojunction. Appl Phys Lett, 2007, 91, 232117
[668] Shibin K T C, Gupta G. Band alignment and Schottky behaviour of InN/GaN heterostructure grown by low-temperature low-energy nitrogen ion bombardment. RSC Adv, 2014, 4, 27308
[669] Akazawa M, Gao B, Hashizume T, et al. Measurement of valence-band offsets of InAlN/GaN heterostructures grown by metal-organic vapor phase epitaxy. J Appl Phys, 2011, 109, 013703
[670] Jiao W, Kong W, Li J, et al. Characterization of MBE-grown InAlN/GaN heterostructure valence band offsets with varying In composition. AIP Adv, 2016, 6, 035211
[671] Ekpunobi A J, Animalu A O E. Band offsets and properties of AlGaAs/GaAs and AlGaN/GaN material systems. Superlattices Microstruct, 2002, 31, 247
[672] Sun H, Park Y J, Li K H, et al. Nearly-zero valence band and large conduction band offset at BAlN/GaN heterointerface for optical and power device application. Appl Surf Sci, 2018, 458, 949
[673] Sun H, Park Y J, Li K H, et al. Band alignment of $B_{0.14}Al_{0.86}N$/$Al_{0.7}Ga_{0.3}N$ heterojunction. Appl Phys Lett, 2017, 111, 122106
[674] Fares C, Tadjer M J, Woodward J, et al. Valence and conduction band offsets for InN and III-nitride ternary alloys on (−201) bulk β-Ga_2O_3. ECS J Solid State Sci Technol, 2019, 8, Q3154
[675] Carey IV P H, Ren F, Hays D C, et al. Band offsets in ITO/Ga_2O_3 heterostructures. Appl Surf Sci, 2017, 422, 179
[676] Fares C, Ren F, Lambers E, et al. Valence and conduction band offsets for sputtered AZO and ITO on (010) $(Al_{0.14}Ga_{0.86})_2O_3$. Semicond Sci Technol, 2019, 34, 025006
[677] Fares C, Ren F, Lambers E, et al. Valence- and conduction-band offsets for atomiclayer-deposited Al_2O_3 on (010) $(Al_{0.14}Ga_{0.86})_2$-O_3. J Electron Mater, 2019, 48, 1568
[678] Liu J M, Liu X L, Xu X Q, et al. Measurement of w-InN/h-BN heterojunction band offsets by X-ray photoemission spectroscopy. Nanoscale Res Lett, 2010, 5, 1340
[679] Zhang Z H, Zhang Y, Bi W, et al. On the internal quantum efficiency for InGaN/GaN light-emitting diodes grown on insulating substrates. Phys Status Solidi A, 2016, 213, 3078
[680] Karpov S. ABC-model for interpretation of internal quantum efficiency and its droop in III-nitride LEDs: a review. Opt Quantum Electron, 2015, 47, 1293
[681] Bayerl M W, Brandt M S, Graf T, et al. *g* values of effective mass donors in $Al_xGa_{1-x}N$ alloys. Phys Rev B, 2001, 63, 165204
[682] McGill S A, Cao K, Fowler W B, et al. Bound-polaron model of effective-mass binding energies in GaN. Phys Rev B, 1998, 57, 8951
[683] Im J S, Moritz A, Steuber F, et al. Radiative carrier lifetime, momentum matrix element, and hole effective mass in GaN. Appl Phys Lett, 1997, 70, 631
[684] Hirayama H, Tsukada Y, Maeda T, et al. Marked enhancement in the efficiency of deep-ultraviolet AlGaN light-emitting diodes by using a multiquantum-barrier electron blocking layer. Appl Phys Express, 2010, 3, 031002
[685] Hirayama H. Quaternary InAlGaN-based high-efficiency ultraviolet light-emitting diodes. J Appl Phys, 2005, 97, 091101
[686] Müßener, Teubert J, Hille P, et al. Probing the internal electric field in GaN/AlGaN nanowire heterostructures. Nano Lett, 2014, 14, 5118
[687] Miller D A B, Chemla D S, Damen T C, et al. Band-edge electroabsorption in quantum well structures: The quantum-confined Stark effect. Phys Rev Lett, 1984, 53, 2173
[688] Carnevale S D, Kent T F, Phillips P J, et al. Polarization-induced pn diodes in wide-bandgap nanowires with ultraviolet electroluminescence. Nano Lett, 2012, 12, 915
[689] Jena D, Heikman S, Green D, et al. Realization of wide electron slabs by polarization bulk doping in graded III–V nitride semiconductor alloys. Appl Phys Lett, 2002, 81, 4395
[690] Green D S, Haus E, Wu F, et al. Polarity control during molecular beam epitaxy growth of Mg-doped GaN. J Vac Sci Technol B, 2003, 21, 1804
[691] Kuo Y K, Shih Y H, Tsai M C, et al. Improvement in electron overflow of near-ultraviolet InGaN LEDs by specific design on last barrier. IEEE Photonics Technol Lett, 2011, 23, 1630
[692] Tangi M, Mishra P, Janjua B, et al. Bandgap measurements and the peculiar splitting of E_2H phonon modes of $In_xAl_{1-x}N$ nanowires grown by plasma assisted molecular beam epitaxy. J Appl Phys, 2016, 120, 045701
[693] Choi S, Wu F, Shivaraman R, et al. Observation of columnar microstructure in lattice-matched InAlN/GaN grown by plasma assisted molecular beam epitaxy. Appl Phys Lett, 2012, 100, 232102
[694] Zhang Z H, Tan S T, Ju Z, et al. On the effect of step-doped quantum barriers in InGaN/GaN light emitting diodes. J Disp Technol, 2013, 9, 226
[695] Kneissl M, Kolbe T, Chua C, et al. Advances in group III-nitride-based deep UV light-emitting diode technology. Semicond Sci Technol, 2010, 26, 014036
[696] Shatalov M, Sun W, Jain R, et al. High power AlGaN ultraviolet light emitters. Semicond Sci Technol, 2014, 29, 084007
[697] Katsuragawa M, Sota S, Komori M, et al. Thermal ionization energy of Si and Mg in AlGaN. J Cryst Growth, 1998, 189, 528
[698] Li L, Miyachi Y, Miyoshi M, et al. Enhanced emission efficiency of deep ultraviolet light-emitting AlGaN multiple quantum wells grown on an n-AlGaN underlying layer. IEEE Photonics J, 2016, 8, 1601710
[699] Zhang Z H, Zhang Y, Bi W, et al. A charge inverter for III-nitride light-emitting diodes. Appl Phys Lett, 2016, 108, 133502
[700] Ho J K, Jong C S, Chiu C C, et al. Low-resistance ohmic contacts to p-type GaN. Appl Phys Lett, 1999, 74, 1275
[701] Chae S W, Kim K C, Kim D H, et al. Highly transparent and low-resistant ZnNi/indium tin oxide Ohmic contact on p-type GaN. Appl Phys Lett, 2007, 90, 181101
[702] Jang H W, Lee J L. Transparent Ohmic contacts of oxidized Ru and Ir on p-type GaN. J Appl Phys, 2003, 93, 5416
[703] Schubert E F, Grieshaber W, Goepfert I D. Enhancement of deep acceptor activation in semiconductors by superlattice doping. Appl Phys Lett, 1996, 69, 3737
[704] Neugebauer S, Hoffmann M, Witte H, et al. All metalorganic chemical vapor phase epitaxy of p/n-GaN tunnel junction for blue light emitting diode applications. Appl Phys Lett, 2017, 110, 102104
[705] Zhang Y, Krishnamoorthy S, Akyol F, et al. Reflective metal/semiconductor tunnel junctions for hole injection in AlGaN UV LEDs. Appl Phys Lett, 2017, 111, 051104
[706] Krishnamoorthy S, Akyol F, Rajan S. InGaN/GaN tunnel junctions for hole injection in GaN light emitting diodes. Appl Phys Lett, 2014, 105, 141104

[707] Kuo Y K, Chang J Y, Chen F M, et al. Numerical investigation on the carrier transport characteristics of AlGaN deep-UV light-emitting diodes. IEEE J Quantum Electron, 2016, 52, 3300105
[708] Cheng B, Choi S, Northrup J E, et al. Enhanced vertical and lateral hole transport in high aluminum-containing AlGaN for deep ultraviolet light emitters. Appl Phys Lett, 2013, 102, 231106
[709] Kim J K, Waldron E L, Li Y L, et al. P-type conductivity in bulk $Al_xGa_{1-x}N$ and $Al_xGa_{1-x}N/Al_yGa_{1-y}N$ superlattices with average Al mole fraction > 20%. Appl Phys Lett, 2004, 84, 3310
[710] Zhu T G, Denyszyn J C, Chowdhury U, et al. AlGaN-GaN UV light-emitting diodes grown on SiC by metal-organic chemical vapor deposition. IEEE J Sel Top Quantum Electron, 2002, 8, 298
[711] Zhang L, Ding K, Yan J C, et al. Three-dimensional hole gas induced by polarization in (0001)-oriented metal-face III-nitride structure. Appl Phys Lett, 2010, 97, 062103
[712] Zhang Z H, Li L, Zhang Y, et al. On the electric-field reservoir for III-nitride based deep ultraviolet light-emitting diodes. Opt Express, 2017, 25, 16550
[713] Jeon S R, Song Y H, Jang H J, et al. Lateral current spreading in GaN-based light-emitting diodes utilizing tunnel contact junctions. Appl Phys Lett, 2001, 78, 3265
[714] Mehnke F, Kuhn C, Guttmann M, et al. Efficient charge carrier injection into sub-250 nm AlGaN multiple quantum well light emitting diodes. Appl Phys Lett, 2014, 105, 051113
[715] Tsai C L, Liu H H, Chen J W, et al. Improving the light output power of DUV-LED by introducing an intrinsic last quantum barrier interlayer on the high-quality AlN template. Solid-State Electron, 2017, 138, 84
[716] Zhang Z H, Huang Chen S W, Zhang Y, et al. Hole transport manipulation to improve the hole injection for deep ultraviolet light-emitting diodes. ACS Photonics, 2017, 4, 1846
[717] Tsai M C, Yen S H, Kuo Y K. Deep-ultraviolet light-emitting diodes with gradually increased barrier thicknesses from n-layers to p-layers. Appl Phys Lett, 2011, 98, 111114
[718] Kolbe T, Sembdner T, Knauer A, et al. (In)AlGaN deep ultraviolet light emitting diodes with optimized quantum well width. Phys Status Solidi A, 2010, 207, 2198
[719] Norimichi N, Hirayama H, Yatabe T, et al. 222 nm single-peaked deep-UV LED with thin AlGaN quantum well layers. Phys Status Solidi C, 2009, 6, S459
[720] Hirayama H, Noguchi N, Yatabe T, et al. 227 nm AlGaN light-emitting diode with 0.15 mW output power realized using a thin quantum well and AlN buffer with reduced threading dislocation density. Appl Phys Express, 2008, 1, 051101
[721] Hirayama H, Yatabe T, Noguchi N, et al. 231 –261 nm AlGaN deep-ultraviolet light-emitting diodes fabricated on AlN multilayer buffers grown by ammonia pulse-flow method on sapphire. Appl Phys Lett, 2007, 91, 071901
[722] Xiu X, Zhang L, Li Y, Xiong Z, et al. Application of halide vapor phase epitaxy for the growth of ultra-wide band gap Ga_2O_3. J Semicond, 2019, 40, 011805
[723] Pratiyush A S, Krishnamoorthy S, Muralidharan R, et al. Advances in Ga_2O_3 solar-blind UV photodetectors. In: Gallium Oxide. Elsevier, 2019, 369
[724] Sedhain A, Lin J Y, Jiang H X. Nature of optical transitions involving cation vacancies and complexes in AlN and AlGaN. Appl Phys Lett, 2012, 100, 221107
[725] Bickermann M, Epelbaum B M, Filip O, et al. Deep-UV transparent bulk single-crystalline AlN substrates. Phys Status Solidi C, 2010, 7, 1743
[726] Bondokov R T, Mueller S G, Morgan K E, et al. Large-area AlN substrates for electronic applications: An industrial perspective. J Cryst Growth, 2008, 310, 4020
[727] Bickermann M, Epelbaum B M, Winnacker A. PVT growth of bulk AlN crystals with low oxygen contamination. Phys Status Solidi C, 1993, 1993
[728] Slack G A, Schowalter L J, Morelli D, et al. Some effects of oxygen impurities on AlN and GaN. J Cryst Growth, 2002, 246, 287
[729] Haughn C R, Rupper G, Wunderer T, et al. Highly radiative nature of ultra-thin c-plane Al-rich AlGaN/AlN quantum wells for deep ultraviolet emitters. Appl Phys Lett, 2019, 114, 102101
[730] Chu C, Tian K, Zhang Y, et al. Progress in external quantum efficiency for III-nitride based deep ultraviolet light-emitting diodes. Phys Status Solidi A, 2019, 216, 1800815
[731] Bryan I, Bryan Z, Washiyama S, et al. Doping and compensation in Al-rich AlGaN grown on single crystal AlN and sapphire by MOCVD. Appl Phys Lett, 2018, 112, 062102
[732] Kirste R, Mita S, Guo Q, et al. Recent breakthroughs in AlGaN-based UV light emitters. IEEE Research and Applications of Photonics In Defense Conference (RAPID), 2018, 18196129
[733] Bryan I, Bryan Z, Mita S, et al. Surface kinetics in AlN growth: A universal model for the control of surface morphology in III-nitrides. J Cryst Growth, 2016, 438, 81
[734] Hartmann C, Wollweber J, Dittmar A, et al. Preparation of bulk AlN seeds by spontaneous nucleation of freestanding crystals. Jpn J Appl Phys, 2013, 52, 08JA06
[735] Sumathi R R. Bulk AlN single crystal growth on foreign substrate and preparation of free-standing native seeds. Cryst Eng Comm, 2013, 15, 2232
[736] Mokhov E, Izmaylova I, Kazarova O, et al. Specific features of sublimation growth of bulk AlN crystals on SiC wafers. Phys Status Solidi C, 2013, 10, 445
[737] Park S H, Shim J I. Carrier density dependence of polarization switching characteristics of light emission in deep-ultraviolet AlGaN/AlN quantum well structures. Appl Phys Lett, 2013, 102, 221109
[738] Dalmau R, Moody B, Xie J, et al. Characterization of dislocation arrays in AlN single crystals grown by PVT. Phys Status Solidi A, 2011, 208, 1545
[739] Herro Z, Zhuang D, Schlesser R, et al. Growth of AlN single crystalline boules. J Cryst Growth, 2010, 312, 2519
[740] Kinoshita T, Obata T, Nagashima T, et al. Performance and reliability of deep-ultraviolet light-emitting diodes fabricated on AlN substrates prepared by hydride vapor phase epitaxy. Appl Phys Express, 2013, 6, 092103
[741] Kinoshita T, Hironaka K, Obata T, et al. Deep-ultraviolet light-emitting diodes fabricated on AlN substrates prepared by hydride vapor phase epitaxy. Appl Phys Express, 2012, 5, 122101
[742] Grandusky J R, Chen J, Gibb S R, et al. 270 nm pseudomorphic ultraviolet light-emitting diodes with over 60 mW continuous wave output power. Appl Phys Express, 2013, 6, 032101
[743] An Y, Sun Y, Zhang M, et al. Tuning the electronic structures and transport properties of zigzag blue phosphorene nanoribbons. IEEE Trans Electron Devices, 2018, 65, 4646
[744] Liu H, Neal A T, Zhu Z, Luo Z, et al. Phosphorene: An unexplored 2D semiconductor with a high hole mobility. ACS Nano, 2014, 8, 4033
[745] Zhang M, An Y, Sun Y, et al. The electronic transport properties of zigzag phosphorene-like MX (M = Ge/Sn, X = S/Se) nanostructures. Phys Chem Chem Phys, 2017, 19, 17210
[746] Li F, Liu X, Wang Y, et al. Germanium monosulfide monolayer: a novel two-dimensional semiconductor with a high carrier mobility. J Mater Chem C, 2016, 4, 2155
[747] Dagan R, Vaknin Y, Henning A, et al. Two-dimensional charge carrier distribution in MoS_2 monolayer and multilayers. Appl Phys Lett, 2019, 114, 101602
[748] Zhou X, Hu X, Yu J, et al. 2D layered material-based van der Waals heterostructures for optoelectronics. Adv Funct Mater, 2018, 28, 1706587
[749] Nayeri M, Fathipour M. A numerical analysis of electronic and optical properties of the zigzag MoS_2 nanoribbon under uniaxial strain. IEEE Trans Electron Devices, 2018, 65, 1988

[750] Fan Z Q, Jiang X W, Luo J W, et al. In-plane Schottky-barrier field-effect transistors based on 1T/2H heterojunctions of transition-metal dichalcogenides. Phys Rev B, 2017, 96, 165402

[751] An Y, Zhang M, Wu D, et al. The electronic transport properties of transition-metal dichalcogenide lateral heterojunctions. J Mater Chem C, 2016, 4, 10962

[752] Cheng R, Li D, Zhou H, et al. Electroluminescence and photocurrent generation from atomically sharp WSe_2/MoS_2 heterojunction p-n diodes. Nano Lett, 2014, 14, 5590

[753] Zhao J, Cheng K, Han N, et al. Growth control, interface behavior, band alignment, and potential device applications of 2D lateral heterostructures. Wiley Interdiscip Rev Comput Mol Sci, 2018, 8, e1353

[754] Koppens F H L, Mueller T, Avouris P, et al . Photodetectors based on graphene, other two-dimensional materials and hybrid systems. Nat Nanotechnol, 2014, 9, 780

[755] Zhu X, Lei S, Tsai S H, et al. A study of vertical transport through graphene toward control of quantum tunneling. Nano Lett, 2018, 18, 682

[756] Asres G A, Järvinen T, Lorite G S,et al. High photoresponse of individual WS_2 nanowire-nanoflake hybrid materials. Appl Phys Lett, 2018, 112, 233103

[757] Chu D, Lee Y H, Kim E K. Selective control of electron and hole tunneling in 2D assembly. Sci Adv, 2017, 3, e1602726

[758] Yamaguchi T, Moriya R, Inoue Y, et al. Tunneling transport in a few monolayer-thick WS_2/graphene heterojunction. Appl Phys Lett, 2014, 105, 223109

[759] Xia F, Wang H, Xiao D, et al. Two-dimensional material nanophotonics. Nat Photonics, 2014, 8, 899

[760] Kim S, Oh S, Kim J. Ultrahigh deep-UV sensitivity in graphene-gated β-Ga_2O_3 phototransistors. ACS Photonics, 2019, 6, 1026

[761] Schubert M, Mock A, Korlacki R, et al. Longitudinal phonon plasmon mode coupling in β-Ga_2O_3. Appl Phys Lett, 2019, 114, 102102

[762] Polyakov A Y, Smirnov N B, Shchemerov I V, et al. Electrical properties of bulk semi-insulating β-Ga_2O_3(Fe). Appl Phys Lett, 2018, 113, 142102

[763] Hu Z, Nomoto K, Li W, et al. Breakdown mechanism in 1 kA/cm^2 and 960 V E-mode β-Ga_2O_3 vertical transistors. Appl Phys Lett, 2018, 113, 122103

[764] Joishi C, Xia Z, McGlone J, et al. Effect of buffer iron doping on delta-doped β-Ga_2O_3 metal semiconductor field effect transistors. Appl Phys Lett, 2018, 113, 123501

[765] Neal A T, Mou S, Rafique S, et al. Donors and deep acceptors in β-Ga_2O_3. Appl Phys Lett, 2018, 113, 062101

[766] Wong M H, Lin C H, Kuramata A, et al. Acceptor doping of β-Ga_2O_3 by Mg and N ion implantations. Appl Phys Lett, 2018, 113, 102103

[767] Yang J, Ren F, Tadjer M, et al. Ga_2O_3 Schottky rectifiers with 1 ampere forward current, 650 V reverse breakdown and 26.5 MW·cm^{-2} figure-of-merit. AIP Adv, 2018, 8, 055026

[768] Lee S U, Jeong J. Short time helium annealing for solution-processed amorphous indium-gallium-zinc-oxide thin film transistors. AIP Adv, 2018, 8, 085206

[769] Polyakov A Y, Smirnov N B, Shchemerov I V, et al. Defects responsible for charge carrier removal and correlation with deep level introduction in irradiated β-Ga_2O_3. Appl Phys Lett, 2018, 113, 092102

[770] Gibbon J T, Jones L, Roberts J W, et al. Band alignments at Ga_2O_3 heterojunction interfaces with Si and Ge. AIP Adv, 2018, 8, 065011

[771] Zhang S, Lian X, Ma Y, et al. Growth and characterization of 2-inch high quality β-Ga_2O_3 single crystals grown by EFG method. J Semicond, 2018, 39, 083003

[772] Polyakov A Y, Smirnov N B, Shchemerov I V, et al. Compensation and persistent photocapacitance in homoepitaxial Sn-doped β-Ga_2O_3. J Appl Phys, 2018, 123, 115702

[773] Zhang K, Feng Q, Huang L, et al. $(In_xGa_{1-x})_2O_3$ photodetectors fabricated on sapphire at different temperatures by PLD. IEEE Photon J, 2018, 10, 6802508

[774] Feng Q, Hu Z, Feng Z, et al. Research on the growth of β-$(AlGa)_2O_3$ film and the analysis of electrical characteristics of Ni/Au Schottky contact using Tung's model. Superlattices Microstruct, 2018, 120, 441-447

[775] Feng Q, Feng Z, Hu Z, et al. Temperature dependent electrical properties of pulse laser deposited Au/Ni/β-$(AlGa)_2O_3$ Schottky diode. Appl Phys Lett, 2018, 112, 072103

[776] Zhang Y, Joishi C, Xia Z, et al. Demonstration of β-$(Al_xGa_{1-x})_2O_3$/Ga_2O_3 double heterostructure field effect transistors. Appl Phys Lett, 2018, 112, 233503

[777] Zhang Y, Neal A, Xia Z, et al. Demonstration of high mobility and quantum transport in modulationdoped β-$(Al_xGa_{1-x})_2O_3$/Ga_2O_3 heterostructures. Appl Phys Lett, 2018, 112, 173502

[778] Chen X, Xu Y, Zhou D, et al. Solar-blind photodetector with high avalanche gains and bias-tunable detecting functionality based on metastable phase α-Ga_2O_3/ZnO isotype heterostructures. ACS Appl Mater Interfaces, 2017, 9, 36997-37005

[779] Oshima T, Okuno T, Fujita S. Ga_2O_3 thin film growth on c-plane sapphire substrates by molecular beam epitaxy for deep-ultraviolet photodetectors. Jpn J Appl Phys, 2007, 46, 7217

[780] Qian L X, Wu Z H, Zhang Y Y, et al. Ultrahigh-responsivity, rapid-recovery, solar-blind photodetector based on highly nonstoichiometric amorphous gallium oxide. ACS Photonics, 2017, 4, 2203

[781] Orita M, Ohta H, Hirano M, et al. Deep-ultraviolet transparent conductive β-Ga_2O_3 thin films. Appl Phys Lett, 2000, 77, 4166

[782] Pratiyush A S, Krishnamoorthy S, Solanke S V, et al. High responsivity in molecular beam epitaxy grown β-Ga_2O_3 metal semiconductor metal solar blind deep-UV photodetector. Appl Phys Lett, 2017, 110, 221107

[783] Guo D, Wu Z, Li P, et al. Fabrication of β-Ga_2O_3 thin films and solar-blind photodetectors by laser MBE technology. Opt Mater Express, 2014, 4, 1067

[784] Moudgil A, Dhyani V, Das S. High speed efficient ultraviolet photodetector based on 500 nm width multiple WO_3 nanowires. Appl Phys Lett, 2018, 113, 101101

[785] Khan F, Khan W, Kim J H, et al. Oxygen desorption kinetics of ZnO nanorod-gated AlGaN/GaN HEMT-based UV photodetectors. AIP Adv, 2018, 8, 075225